Studies of Intrinsic Properties of Gamma Ray Bursts Detected by the *HETE-II* Satellite

by

Peter Csatorday

Submitted to the Department of Physics
in partial fulfillment of the requirements for the degree of

Doctor of Philosophy

at the

MASSACHUSETTS INSTITUTE OF TECHNOLOGY

September 2006

Author .....
Department of Physics
September 29, 2006

Certified by .....
George R. Ricker
Senior Research Scientist
Thesis Supervisor

Certified by .....
Saul Rappaport
Professor
Thesis Supervisor

Accepted by .....
Thomas J. Greytak
Associate Department Head for Education

Studies of Intrinsic Properties of Gamma Ray Bursts Detected by the *HETE-II* Satellite

by

Peter Csatorday

Submitted to the Department of Physics
on September 29, 2006, in partial fulfillment of the
requirements for the degree of
Doctor of Philosophy

Abstract

Analysis of *HETE-II* data is discussed with the aim of understanding the intrinsic properties of gamma-ray bursts (GRBs). A technique is developed that allows the simultaneous estimation of source and background counts during a burst with coded aperture instruments such as the Wide-field X-ray Monitor (WXM) on *HETE-II*. A closely related photon-by-photon statistical bootstrap analysis is then described that can be used to compute the non-Gaussian error distribution of GRB temporal statistics. This is applied to the T_{90} and $T_{0.45}$ duration measures. The distribution of T_{90} has been extensively studied since the availability of the *BATSE* gamma-ray burst catalogs and is widely believed to be log-normally distributed. It is shown that intrinsically, GRBs may in fact have a much narrower distribution, and the wide log-normal may primarily be due to measurement artifacts.

Computation of the $T_{0.45}$ parameter enables the inference of redshifts through the recently discovered $L_{\rm iso}$–$E_{\rm pk}$–$T_{0.45}$ relation. This in turn allows the compilation of a flux-limited sample of bursts with redshifts that is free of the observational selection effects inherent in spectroscopic catalogs. This analysis is performed for 31 WXM bursts and redshift-corrected distributions of T_{90} and $T_{0.45}$ are computed. It is shown for the first time that the distribution of $T_{0.45}$ can be modeled by an exponential distribution.

The redshifts calculated through the $L_{\rm iso}$–$E_{\rm pk}$–$T_{0.45}$ relation are also used to calculate the implied isotropic luminosities. The normalized luminosity function and redshift distribution of gamma-ray bursts are derived using the non-parametric methods of Lynden-Bell and Efron & Petrosian. The results imply strong evidence for luminosity evolution with redshift and are consistent with prior studies based on *BATSE* bursts. Concordance cosmology ($\Omega_\Lambda = 0.7$, $\Omega_M = 0.3$, H_0=70 km s^{-1} Mpc^{-1}) is assumed throughout the analysis. Effects of log-normal errors in the redshifts are estimated using Monte-Carlo methods. Results indicate that a fraction close to 10% of GRBs are to be expected at high redshifts (> 5) in consonance with theoretical predictions of high-redshift *Swift* detections.

Thesis Supervisor: George R. Ricker
Title: Senior Research Scientist

Thesis Supervisor: Saul Rappaport
Title: Professor

Acknowledgments

I am very grateful for the assistance that Garrett Jernigan has provided me over the past three years. He has been incredibly generous with his time, advice, and ideas. Garrett has also been a great motivator and collaborator, and never doubted the value and positive outcome of our projects and this thesis.

I am thankful to my advisor, George Ricker, for providing me with a great opportunity to work on an exciting project. I also thank the members of my thesis committee, Saul Rappaport, Claude Canizares and Walter Lewin, for their guidance and insightful questions. Al Levine has also been kind enough to devote considerable time to my questions. Thanks also to Nat Butler who worked closely with me when I joined the group.

Of course, none of this would have been possible without the *HETE-II* team of Geoff Crew, John Doty, Gregory Prigozhin, Roland Vanderspek, and Joel Villasenor. I also appreciate the efforts of the greater *HETE-II* collaboration; in particular I had a many helpful discussions with Carlo Graziani, Tim Donaghy, and Takanori Sakamoto. I thank Kevin Hurley, Jay Selvidge, Roger Williams and Zachary Geary, who indirectly contributed to my work through their efforts on the spectral fits.

Contents

List of Figures

List of Tables

Chapter 1

Introduction

Gamma-ray bursts (GRBs) were detected first in 1969 by military satellites developed by the United States of America in a mission to enforce the Nuclear Test Ban Treaty prohibiting above-ground tests of nuclear weapons. It was soon realized that the source of γ-radiation was extra-terrestrial and the results were reported in 1973 (Klebesadel et al. 1973).

Following their discovery, GRBs were detected by a number of space instruments, in both X-ray and γ-ray bands. Hundreds of theories were advanced regarding their origin, but without knowledge of the distance scale to these events, progress was limited. The Burst and Transient Source Experiment (*BATSE*) (Fishman et al. 1989) on the Compton Gamma-Ray Observatory (CGRO) mission represents a milestone in the understanding of GRBs. Over its nine year mission (1991-2000), *BATSE* cataloged 2704 bursts, and established their distribution to be isotropic on the sky. Together with the peak flux distribution, which pointed toward a non-Euclidean or non-homogeneous source distribution, cosmological rather than galactic distances were strongly favored (Paczyński 1995; Lamb 1995). *BATSE* was also able to provide spectral information and high time resolution, but had large (degree scale) localization uncertainty. The initial High Energy Transient Explorer (*HETE*) was designed with the capability of providing more accurate and timely locations, but was lost on launch in November 1996. On 28 February 1997, the Dutch-Italian satellite, *Beppo*SAX (1996-2002), was the first to accurately localize and image a fading X-ray transient

at the position of a GRB (Costa et al. 1997). The detection of this "afterglow" was a watershed event and eventually led to the detection of fast fading optical afterglows and GRB redshift determinations through optical spectroscopy. We now know GRBs to be cosmologically distant events, and the *HETE-II* mission, launched in October 2000 and still operating as of this writing, has been a key mission in exploring their mysteries. *HETE-II* was the only mission dedicated to GRB science until the launch of *Swift* in 2004.

In this thesis we present analysis of *HETE-II* data. We begin with an overview of gamma-ray burst observational properties and the *HETE-II* satellite. In chapter 2 we present a new method of subtracting background rates from GRB observations that can be applied to coded mask instruments like the WXM. Chapter 3 discusses the estimation of temporal characteristics of gamma-ray bursts by means of a photon-by-photon statistical bootstrap method. In chapter 4 we investigate what the *HETE-II* data imply about the luminosity distribution function and redshift distribution of GRBs using a very recent result to estimate redshifts and a novel technique for calculating the statistical errors of the analysis. Partial results of chapters 3 and 4 are combined in the analysis of the duration distributions of GRBs in chapter 5 and our conclusions are summarized in chapter 6. Tables in Appendix A list characteristics of the bursts of our sample the we used for the analysis in chapter 4. The Appendix also shows lightcurves and the results of the methods of chapter 3 for these bursts.

1.1 Observational Properties of GRBs

1.1.1 Temporal Properties

The observed instrument count rates as a function of time are referred to as time histories, or lightcurves. GRB lightcurves are often discussed in "morphological" terms, but in general are quite diverse, even unique. Some have single peaks with a fast rise and exponential decay (FRED) while others have multiple peaks. Early papers discuss some of these morphologies in conjunction with the duration of the bursts and

point out that "short" bursts may form a separate class (Mazets & Golenetskii 1981). The different morphologies have led to various incompatible definitions of burst durations (for instance, how to include decay times of "tails", etc). In the *BATSE* era, the T_{90} (and T_{50}) duration measures were introduced as the time it takes the cumulative background subtracted burst counts to advance from 5% to 95% (25% to 75%) of the time-integrated burst flux (often called "fluence"). Bimodality of the GRB duration distribution was suspected based on the first twenty years of observations (Hurley 1992), and then firmly established with the observed *BATSE* distributions of T_{90} and T_{50} (Kouveliotou et al. 1993). Figure 1-1 shows the bimodality of the T_{50} parameter in the fourth *BATSE* catalog (Paciesas et al. 1999), and figure 5-2 shows the same for T_{90}.

Two distinct classes of bursts, "short" and "long", were identified, with $T_{90} < 2$s for the former and $T_{90} > 2$s for the latter. The bimodality of the duration distribution is important since it points to different progenitor classes of bursts. The short bursts are believed to be coalescing compact object binaries (neutron star–neutron star or neutron star–black hole binaries) (Eichler et al. 1989; Paczyński 1991), and the long bursts are thought to be associated with the end stages of massive rotating stars in the "collapsar" model (Woosley 1993). This classification is still an open question, and the existence of an intermediate class has been indicated principally based on duration statistics (Horváth 1998, 2002) and on multivariate and clustering methods on duration and other parameters such as spectral hardness and fluence (e.g. Mukherjee et al. 1998; Horváth et al. 2006).

Another measure of duration is the "emission time", or "high-signal time" of the burst. This quantity is the length of time that a specified fraction of the burst fluence lasts when considering only the brightest parts of the burst. This parameter was introduced by Mitrofanov et al. (1999) and Reichart et al. (2001) and is discussed further in sections 3.1 and 3.5.

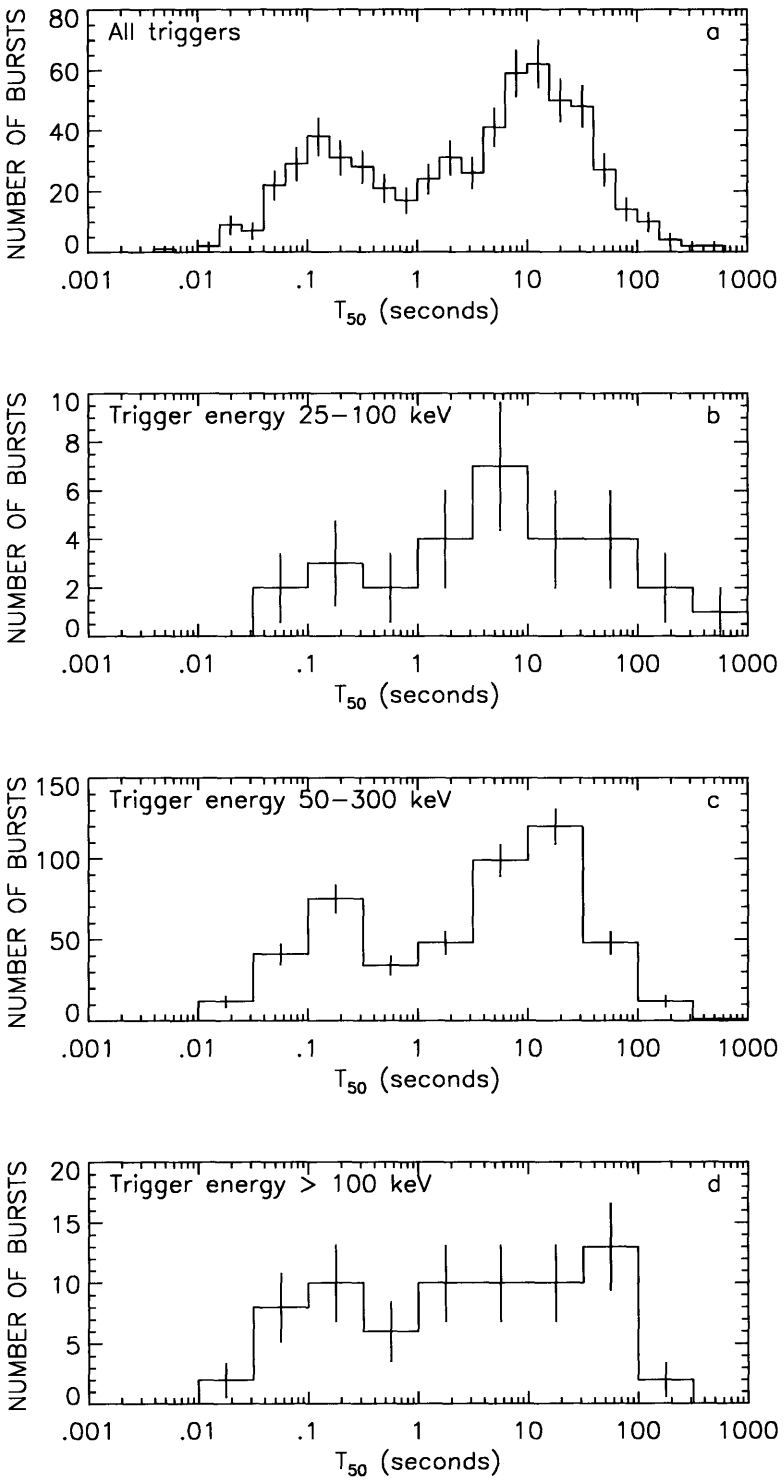

Figure 1-1: Distribution of the T_{50} duration measure of the fourth revised *BATSE* catalog. The bimodality is easily seen when all triggers are considered (top panel). From Paciesas et al. 1999.

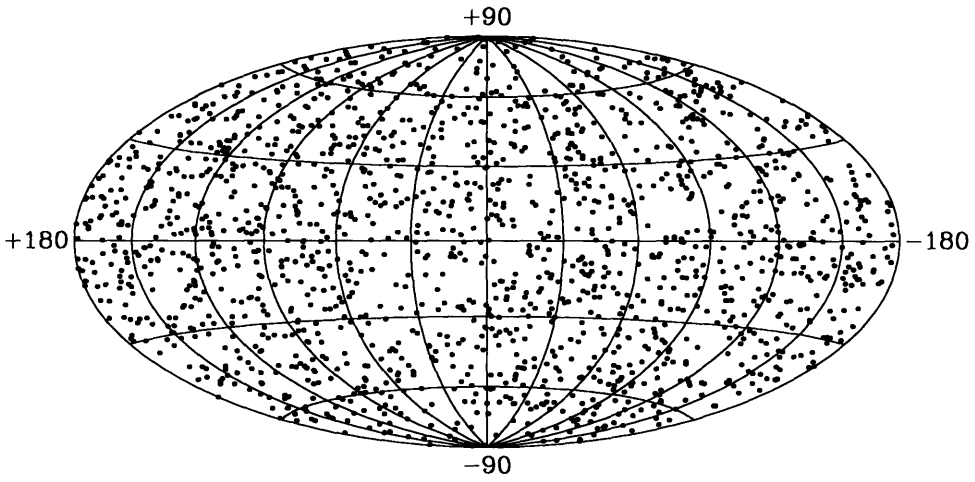

Figure 1-2: Plot of the (isotropic) distribution of 1637 bursts from the fourth revised *BATSE* catalog. (Paciesas et al. 1999). The plot is an Aitoff-Hammer projection in galactic coordinates, and no correction was made for sky coverage.

1.1.2 Spatial Distribution

There are two key aspects of the spatial distribution of gamma-ray bursts: their isotropy (uniformity with respect to rotation, i.e., direction on the sky) and homogeneity (uniformity with respect to translation, i.e., radial distance from us). Both of these aspects were addressed by the *BATSE* observations. With 1005 bursts, Briggs et al. (1996) demonstrate that the distribution is consistent with isotropy. Figure 1-2 shows the sky distribution of a larger sample of 1637 bursts the fourth revised *BATSE* catalog, not accounting for the sky exposure. *BATSE* data was also used to establish that the distribution of bursts is inhomogeneous. This is deduced from the paucity of sources of low brightness in the catalog: if we consider a uniform distribution of sources in a Euclidean space, $N(> P)$, the number of sources detected with peak flux greater than P, is expected to scale as $P^{-3/2}$. Since the *BATSE* burst counts fall below this power law for low values of P (faint bursts), this implies a non-uniformly distributed, or inhomogeneous, source population (Paciesas et al. 1999). From the afterglow redshift measurements we know bursts to be cosmologically distant, so this result is understandable both because space is non-Euclidean and because the burst distribution is bounded. (Note that constraining cosmological parameters using the $N(> P)$ vs. P relation is not possible since the spectral energy distribution of each

source would have to be known, given that different source wavelengths are redshifted into the detector bandpass for each burst depending on its distance.)

1.1.3 Spectral Properties

Spectral Models

Gamma-ray burst spectra were extensively studied with *BATSE*. The time-averaged spectra were found by Band et al. (1993) to be well described with a four parameter model of two smoothly joined power laws. The form of this GRB model, often called the "Band" function after the article's first author, is:

$$N_{E,GRB}(E) = \begin{cases} A\left(\frac{E}{100\text{ keV}}\right)^{\alpha}\exp\left(-\frac{E}{E_0}\right) & \text{if } E \leq E_{break} \\ A\left[\frac{(\alpha-\beta)E_0}{100\text{ keV}}\right]^{\alpha-\beta}\exp(\beta-\alpha)\left(\frac{E}{100\text{ keV}}\right)^{\beta} & \text{if } E > E_{break} \end{cases} \tag{1.1}$$

where

$$E_{break} \equiv (\alpha-\beta)E_0, \tag{1.2}$$

A is the normalization (in photons $\text{s}^{-1}\ \text{cm}^{-2}\ \text{keV}^{-1}$), α is the low energy spectral index, β is the high energy spectral index. In the $E^2N(E)$-energy spectrum, this functional from has a peak at $E_{\text{pk}} = (2+\alpha)E_0$. Figure 1-3 shows an example analytical Band model that was used to fit GRB911127.

When E_{pk} falls out of, or near the edge of the sensitive range of the instruments, the Band model fit cannot successfully determine all four parameters from the data. In such instances one typically fits simpler models, such as a power-law, $N(E) = A(E/100\text{keV})^{\alpha}$, or a cutoff power-law:

$$N(E) = A\left(\frac{E}{100\text{ keV}}\right)^{\alpha}\exp\left(-\frac{E(2+\alpha)}{E_{\text{pk}}}\right) \tag{1.3}$$

The relationship in equation 1.3 is identical to the low energy part of the Band spectrum. Often the energy normalization in the power law is specified as something other than 100 keV (for example 15 keV in Sakamoto et al. 2005).

Preece et al. (2000) fit the Band model to segments of 156 of the brightest *BATSE*

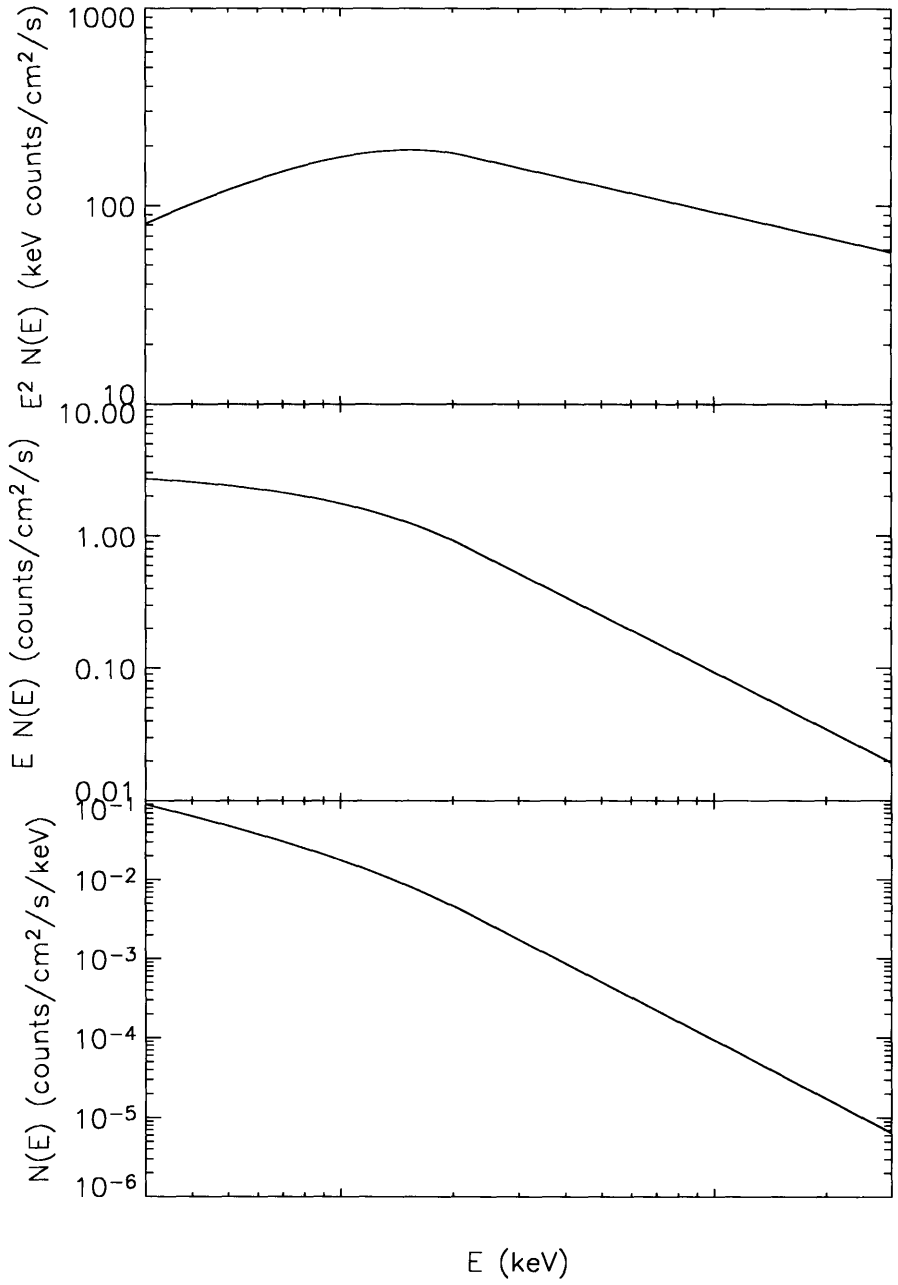

Figure 1-3: An example Band spectral model (used to fit GRB911127 by Band et al. (1993)). For this particular model, the parameters were $\alpha = 0.968$, $\beta = -2.427$ and $E_0 = 149.5keV$. The upper panel shows the count spectrum multiplied by E^2, which shows the peak at $E_{\rm pk}$=154.3 keV.

bursts (selected as ones with minimum fluence in the 30-1000 keV band of 4×10^{-5} ergs cm^{-2} and a minimum peak flux in the 50-300 keV band of 10 ph cm^{-2} s^{-1}) and examined the distribution of the model parameters. $E_{\rm pk}$, α, and β all tend to cluster with singly peaked distributions about typical values of 250 keV, -0.8 and -2.2, respectively.

1.1.4 X-ray Flashes and X-ray Rich Bursts

The low energy threshold of *BATSE* of 30 keV prevented it from detecting softer X-ray transients. X-ray flashes, or XRFs are a class of GRBs that fall into this category, with $E_{\rm pk}$ as low as a few keV and with high X-ray to γ-ray fluence ratios. X-ray rich bursts, or XRRs, are similar, but with more moderate fluence ratios. The exact definitions of these events vary by instrument and research group. For *HETE-II* and *Beppo*SAX the classification is that if $\log(S_X/S_\gamma) > 0$, it is considered an XRF, if $-0.5 < \log(S_x/S_\gamma) \leq 0$ then it is an XRR, and a "hard" GRB otherwise, where S is the fluence in the band indicated by the subscript (Sakamoto 2004; Sakamoto et al. 2005). XRFs and XRRs were initially identified and observed with *GINGA* (Strohmayer et al. 1998) and *Beppo*SAX (Heise et al. 2001), and then in greater numbers with *HETE-II* (26 XRFs and 36 XRRs to date).

1.1.5 Energetics

Having measured the flux, the integrated flux (fluence) and the redshift, one can calculate the γ-ray luminosity and the total energy released in the GRB, assuming a geometry for the emitting region and a cosmology. Under the assumption that the source emits in a spherically symmetrical pattern, the calculated quantities are called the "isotropic-equivalent" energy and luminosity, denoted by E_{iso} and L_{iso}. However, current observations and theory indicate the isotropic emission model is improbable and instead, highly relativistic jets are present. The reasons for this are that the highly relativistic ($\Gamma \sim$ 100–300) emission is more easily accommodated by a jet model, as are the extremely high energies that would otherwise be implied by

the flux measurements and the assumption of isotropy ($E_{iso} \sim 10^{54}$ erg). As the jets expand into the cold material of the medium surrounding the central engine of the GRB, they create an "external" shock, accelerating electrons which then become a source of synchrotron emission. This synchrotron emission is observable in most wave bands (X-ray, optical, radio) as the afterglow emission, which then decays as a power-law in time (e.g. Sari et al. 1998). As the jets expand and slow down, their high bulk Lorentz factor decreases until eventually $1/\Gamma$ is about the size of the jet opening angle, θ_j. Up to this point relativistic beaming effects prevent the observer from seeing the entire jet surface, but once $1/\Gamma \sim \theta_j$, the entire jet is visible and the decay in observed flux continues faster. In other words, there is an achromatic *break* in the lightcurve of the afterglow, which can be observed in X-ray and the optical. The time after the onset of the burst prompt emission that this happens is the break time, t_{break}. Conversely, observing a break time in the afterglow, coupled with assumptions about the ambient density and the efficiency of gamma-ray production by the shock, allows one to infer the jet opening angle (Sari et al. 1999) and a beaming factor. This beaming, or collimation, factor can be applied as a correction to the isotropic equivalent energy and the observed rate of GRBs. Frail et al. 2001 performed this analysis on 17 GRBs and found that after correcting for a conical jet, the energy released in gamma-rays is $E_\gamma \sim 5 \times 10^{50}$ ergs, and distributed much more narrowly than the uncorrected, inferred $E_{\rm iso}$. Bloom et al. 2003 analyzed a larger sample of 29 bursts and found $E_\gamma \sim 1.33 \times 10^{51}$ ergs, with a burst-to-burst variance of 2.2 (0.35 dex).

1.1.6 Empirical Relations

Energy and Pulse Width

Realizing that GRBs are cosmologically distant events, it is important to be able to distinguish between cosmological time dilation and intrinsic GRB effects that influence the observations. To this end, Fenimore et al. (1995) investigated the timescale of pulses in GRB lightcurves measured in different energy bands. They calculated the

average autocorrelation function of 45 bright *BATSE* bursts and found they were well fit by two exponentials. The width of the autocorrelation peaks depend on the energy bands, and to a good approximation, the relationship is a power-law: $t \propto E^{-0.4}$. This scaling was confirmed by Norris et al. 1996 using different methods.

'Amati Relation'

With the availability of spectroscopic redshifts it became possible to investigate correlations between intrinsic (cosmological rest-frame) properties of GRBs, which would be a clue to the underlying physics. Amati et al. (2002) showed using 12 *Beppo*SAX bursts that there is a statistically significant correlation with low chance probability between the intrinsic peak energy, $E_{\rm pk}$, and the isotropic equivalent energy, $E_{\rm iso}$, of approximately $E_{\rm pk} \propto {E_{\rm iso}}^{0.5}$. This result was then confirmed with *HETE-II* bursts of all classes (GRB, XRR, XRF), with low and high redshifts. In an updated analysis Amati (2006) shows that the relation holds over $\sim$5 orders of magnitude in $E_{\rm iso}$ and $\sim$3 orders of magnitude in $E_{\rm pk}$, with a scatter standard deviation of about 0.2 dex, but that bursts of the short class and sub-luminous bursts are inconsistent with it. This relation is often called the 'Amati' relation, or the $E_{\rm pk}$–$E_{\rm iso}$ relation.

'Ghirlanda Relation'

Another relation, found by Ghirlanda et al. (2004a), is a significant correlation between the intrinsic peak energy and the collimation-corrected energy, $E_{\rm pk} \propto E_\gamma^{0.7}$. This empirical relation, called the 'Ghirlanda' or $E_{\rm iso}$–$E_{\rm pk}$–$t_{\rm break}$ relation, has smaller scatter (a standard deviation of 0.1 dex) than the 'Amati' relation. Note, however, that observation of t_{break} is necessary for each burst that is tested against this relation.

'Firmani Relation'

Most recently Firmani et al. (2006c) have shown that a multivariate correlation exists with even tighter scatter (0.06 dex) than the Amati or Ghirlanda relations. They found that $L_{\rm iso} \propto {E_{\rm pk}}^{1.62} {T_{0.45}}^{-0.49}$, where $T_{0.45}$ is a high-signal timescale (mentioned above in section 1.1.1 and discussed more in section 3.5). The analysis was done with

19 bursts with redshift ranging up to 4.3. The importance of this relation is that it does not depend on the break time of the afterglow, which means it can be used as a luminosity (and distance) estimator based only on the prompt burst emission. See further discussion in section 4.3

Luminosity, Variability and Spectral Lag

Two other relations are worthy of note since they feature in many related works. They allow the estimation of luminosity based on observables of the prompt γ-ray burst emission, and so are useful as empirical redshift estimators (Section 4.2).

Norris et al. (2000) investigated the spectral and time evolution of GRB pulses in *BATSE* bursts by calculating cross-correlation functions between lightcurves of different energy bands (25-50 keV and 100-300 keV). The time lag of the cross-correlation function is termed the 'spectral lag', and the higher energy channel is found to lead the lower energy one. Applying the method to the bursts with measured spectroscopic redshifts (detected simultaneously with *BATSE* and *Beppo*SAX), they find that the maximum (peak) isotropic equivalent luminosity, $L_{\rm iso}$, and the spectral lag, τ, are related by:

$$L_{iso} \approx 1.3 \times 10^{53}\mathrm{erg} \times (\tau/0.01\mathrm{s})^{-1.15} \tag{1.4}$$

A key point to note about this relationship is that it is established only for long-duration bursts.

Two related works (Fenimore & Ramirez-Ruiz 2000; Reichart et al. 2001) discuss a "Cepheid-like" relationship between the variability of long duration burst lightcurves and the isotropic-equivalent luminosity. The variability, V, is slightly different in the two works, but is essentially the RMS scatter of the lightcurve once a smoothed version has been subtracted and the Poisson noise accounted for (the smoothing timescale turns out to be the $T_{0.45}$ high-signal timescale used in the Firmani relation). Reichart et al. (2001) find that $L \sim V^{3.3}$ and Fenimore & Ramirez-Ruiz (2000) find

$$L/d\Omega = 3.1 \times 10^{56} V^{3.35}\mathrm{ergs}^{-1} \tag{1.5}$$

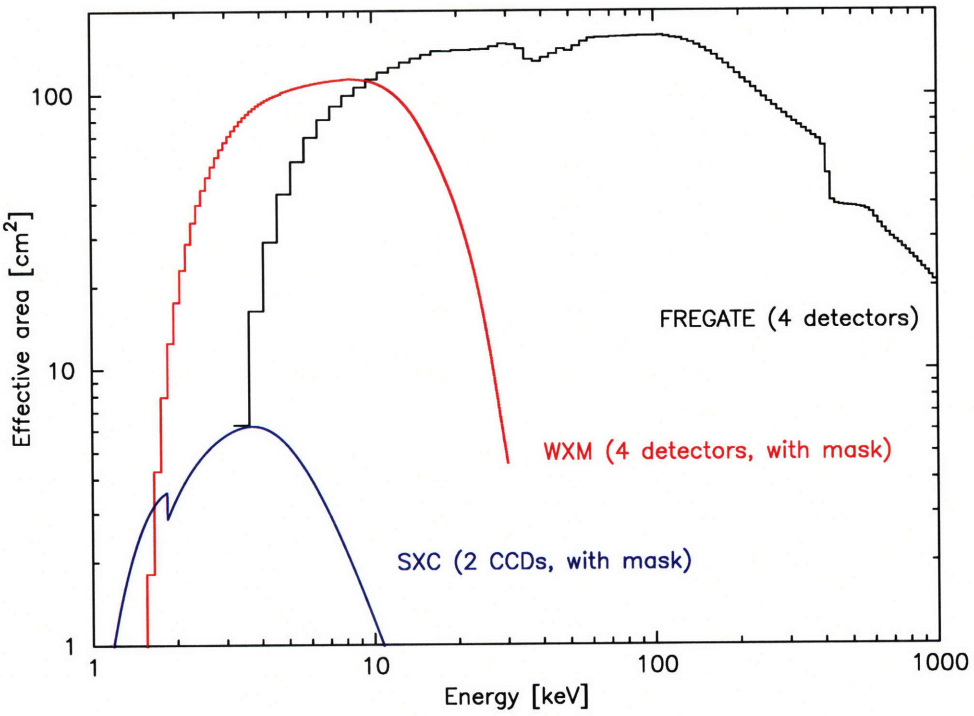

Figure 1-4: Effective area of FREGATE, WXM and SXC (Sakamoto 2004).

1.2 The *HETE-II* Satellite

The High Energy Transient Explorer 2 (*HETE-II*; Ricker et al. 2003) was launched into a low altitude equatorial orbit on October 9, 2000 aboard a Pegasus rocket. A NASA project with international collaborators contributing two of the three science instruments, its mission is to detect and localize gamma-ray bursts (GRBs), to disseminate the information quickly to enable follow-up observations by the astronomical community, and to study GRB prompt X- and γ-ray emission properties. To accomplish this, the spacecraft carries a complement of three science instruments, the Soft X-ray Camera (SXC), the Wide Field X-ray Monitor (WXM), and the French Gamma-Ray Telescope (FREGATE). The WXM and SXC instruments allow sky localizations of GRBs to about 10 arc-minute and 20 arc-second accuracy, respectively, but FREGATE is unable to localize GRBs with any reasonable precision. The instruments are complementary in their energy response as well (see figure 1-4). On-board triggering is possible with FREGATE and WXM. More details of these instruments are provided in the following subsections.

Communication with the satellite is achieved through three primary ground stations in Singapore, the Kwajalein Atoll (Marshall Islands), and Cayenne (French Guiana), as well as with a larger number of secondary, "burst alert", ground stations. These stations in turn communicate with the operations center at MIT via the Internet. Information about bursts is disseminated through the Gamma-Ray Burst Coordinates Network (GCN) via near real-time notices and circulars.

In normal operations, *HETE-II* is oriented to point the science instruments away from the sun. The usual anti-solar pointing is modulated by "nodding" away from the galactic plane in the summer months (when known sources such as Sco X-1 and the so-called GX sources could dominate the instrument telemetry) and away from the moon near full moon. Orbits are about 96 minutes long, with about 40 minutes of nighttime operations. During orbit day, the science instruments do not operate and the batteries are charged. Daytime aspect is maintained using sun sensors and magnetometers. At the dusk terminator the instruments are turned on and during night the aspect is maintained with optical star tracker cameras.

1.2.1 WXM

The WXM instrument on *HETE-II* was provided by Japan, with major contributions from RIKEN, Tokyo Institute of Technology, and Aoyama Gakuin University (Shirasaki et al. 2003). Los Alamos National Laboratory and the University of Chicago were also major participants in the development and operation of the WXM. The instrument is sensitive to medium energy X-ray photons, from 2 to 25 keV. It consists of two "cameras", each providing localization in one primary direction, with the axes of the two cameras orthogonally oriented to provide two-dimensional locations (X and Y). Each camera consists of a coded mask mounted 187 mm above two position sensitive proportional counters (PSPCs) labeled XA, XB and YA, YB. The PSPCs are gas filled detectors with resistive carbon fiber wire anodes and associated pulse height analyzers and electronics. The gas is 97% Xe and 3% CO_2, at a room temperature pressure of 1.4 atm. There are also ^{55}Fe calibration sources in the support structure of the coded mask, located 40 mm from the center of the counter. A summary of the

WXM characteristics is in table 1.1.

Wide-Field X-ray Monitor	
Built by	RIKEN (Japan) and LANL
Instrument type	Coded Mask with PSPC
Energy Range	2 to 25 keV
Timing Resolution	1 ms
Spectral Resolution	~25% @ 20 keV
Detector QE	90% @5 keV
Geometric Area	~175 cm^2 (each of two units)
Sensitivity (10 σ)	~8×10^{-9} $erg/cm^2/s$ (2-10 keV)
Field of View	1.6 steradians (FWZM)
Localization resolution	$19'(5\sigma$ burst) $2.7'(22\sigma$ burst)

Table 1.1: Wide Field X-ray monitor characteristics. (Kawai et al. 2003)

The data products of the WXM instrument include house keeping (temperatures, voltage settings, etc.) and raw, unprocessed photon data with 1 μs resolution in addition to four data products that are used for scientific purposes: TH, POS, TAG and PHA. TH are time histories (i.e., count rates) with 1.2 s resolution in four energy bands for the four detectors; POS data are 6.6 s time resolution, 128 bin position histograms in two energy bands for each of the four detectors; TAG data are 256 μs resolution time-tagged photon data that is generated and telemetered during burst observation mode; and PHA are 4.9 s resolution energy spectra for four energy bands. Most of the analysis in this thesis uses POS or TAG data.

1.2.2 SXC

Like the WXM, the Soft X-ray camera (Villasenor et al. 2003) is a subsystem of two orthogonally oriented detectors each of which is sensitive to the incident angle of incoming X-ray photons along one dimension. The SXC also has a coded aperture mask, although with much finer elements than that of the WXM (see table 1.2). The detectors in the SXC are front-side illuminated, 2048 $\times$ 4096 pixel CCDs, read out along one dimension at 1.2 s intervals. They operate at -50° C, which is achieved

by passive radiative cooling. The CCDs are sensitive to both optical light and X-rays, with appreciable effective area for X-rays in the 1.5-10 keV range. Due to the sensitivity to polluting optical light, e.g. moonlight, two optical blocking filters were installed: an outer filter above the gold mask made of aluminized polyimide film, and an inner one made of Be foil that covers half the CCD area. The polyimide film was eroded by unexpectedly high levels of atomic oxygen in 2001 and therefore only the chips covered by the inner blocking filter are currently useful. During a five day interval centered on full moon, even these are contaminated by optical light and standard operating procedure is to turn off the SXC during these periods. Absorption of low energy X-rays by the beryllium filter is responsible for raising the low energy cutoff from about 0.5 keV to 1.5 keV.

Soft X-ray Camera	
Camera Size	$100 \times 100 \times 100$ mm
Instrument type	Coded Mask with CCID-20
Field of View	0.9 sr (FWHM)
Angular Resolution	33″per CCD pixel
Detector-Mask Distance	95 mm
Mask Open fraction	0.2
Mask element size	45 μm
Timing Resolution	1.2s

Table 1.2: SXC characteristics (Villasenor et al. 2003).

The SXC mask pattern is oversampled by the CCD by a factor of three, and the device can routinely localize sources to high accuracy (about 20″ RMS radius). However, the correlation patterns used in the localization analysis can produce coding noise correlation peaks for faint sources that are of comparable amplitude to that due to the source, so it is necessary to restrict the location search to a $\pm 1°$ range in X and Y *a priori*. This is done by "seeding" the position search with the result of the WXM correlation.

The SXC also carries ^{55}Fe calibration sources to monitor gain changes.

1.2.3 FREGATE

The French Gamma-Ray Telescope (FREGATE) (Atteia et al. 2003) is the instrument aboard *HETE-II* with the largest field of view (about 4 steradians) and the widest energy range (6-400 keV). Table 1.3 summarizes its properties.

The French Gamma-Ray Telescope	
Energy range	6 - 400 keV
Effective area (4 detectors, on axis)	160 cm^2
Field of view (FWZM)	70°
Sensitivity (50 - 300 keV)	10^{-7} erg cm^{-2} s^{-1}
Dead time	10μs
Time resolution	6.4μs
Maximum acceptable photon flux	10^3 ph cm^{-2} s^{-1}
Spectral resolution at 662 keV	~8%
Spectral resolution at 122 keV	~12%
Spectral resolution at 6 keV	~42%

Table 1.3: FREGATE characteristics (Atteia et al. 2003).

FREGATE is a set of four cleaved NaI crystal scintillators each with associated shielding, photomultiplier tubes (PMT), discriminators, pulse height analyzers, and digital electronics. The shield is mostly opaque to photons of low energies but transparent at higher energies. For example at 150 keV the transparency is 5.5%, but at 300 keV it is 55% (Atteia et al. 2003). The shield extends beyond the PMT and scintillator, forming a collimator which restricts the field of view of the instrument at low photon energies. This field of view is larger than that of the WXM, with significant exposed detector area (at least 60 cm^2) for any WXM burst. The collimator reduces the sensitivity of FREGATE to detection of galactic X-ray sources (XRBs, SGRs, SCO X-1) during the summer whose signal would dominate *HETE-II*'s data telemetry, thereby inhibiting the detection of transients. The 6 keV low end of the energy range is set by the beryllium housing of the crystals and the upper 400 keV end is set by the electronics. Two ^{133}Ba sources outside the detectors allow in-flight calibration.

The data provided by FREGATE include housekeeping, time histories (light curves), spectra and burst data. The continuous light curves are generated every

0.16 s and 0.32 s in four adjustable energy bands (nominally 6-40 keV, 6-80 keV, 32-400 keV and >400 keV, or bands A, B, C, D, respectively) for each of the four detectors. Spectra are generated in 128 channels every 5 or 10 seconds. Burst data are photon events tagged by energy and time with a resolution of 6.4 μs and 256 channels in the 0-400 keV range. There is a circular buffer of 64k photons per detector. The buffer contents are saved and telemetered to the ground when a burst triggers. FREGATE is also a triggering instrument, meaning that count rate excesses are detected by the on-board DSP and can activate burst mode.

1.3 Real Time Triggering and Analysis

The *HETE-II* satellite has a complex and time variable methodology for determining a triggered event. Each such event is assigned a BID number (burst identification) that references any analysis of that trigger. If a trigger is determined to be a GRB then the BID is also assigned a GRB name which is reported to the GCN (Gamma-Ray Burst Coordinates Network) via the internet. Figure 1-5 shows a plot of a trigger event, BID3666, alternatively referred to as H3666. This particular BID is also GRB050123A, the first GRB (A) detected on 23 January 2005 (050123). As figure 1-5 indicates this particular burst was triggered in the B spectral band of the FREGATE instrument. This display is automatically posted to the MIT burst web site after the full telemetry stream is delivered over the internet usually within 1-2 hours of the time of the trigger. In a number of cases, such GRBs are reported to the GCN within 10 seconds after the trigger directly from the *HETE-II* satellite via a special low bandwidth telemetry channel. The ground system also computes fluxes in the A, B and C FREGATE bands so that the color ratios C/A and B/A can be used to mark the location in a color-color diagram (see Figure 1-6). This diagram also has all prior GRBs plotted so that a quick preliminary assessment of the type of GRB (XRF, XRR, GRB) can be determined. If the event lies along the correlation line in the color-color plot, then it is also more likely to be a real GRB. Most triggers are not real GRBs and therefore have color ratios that are not consistent with GRBs.

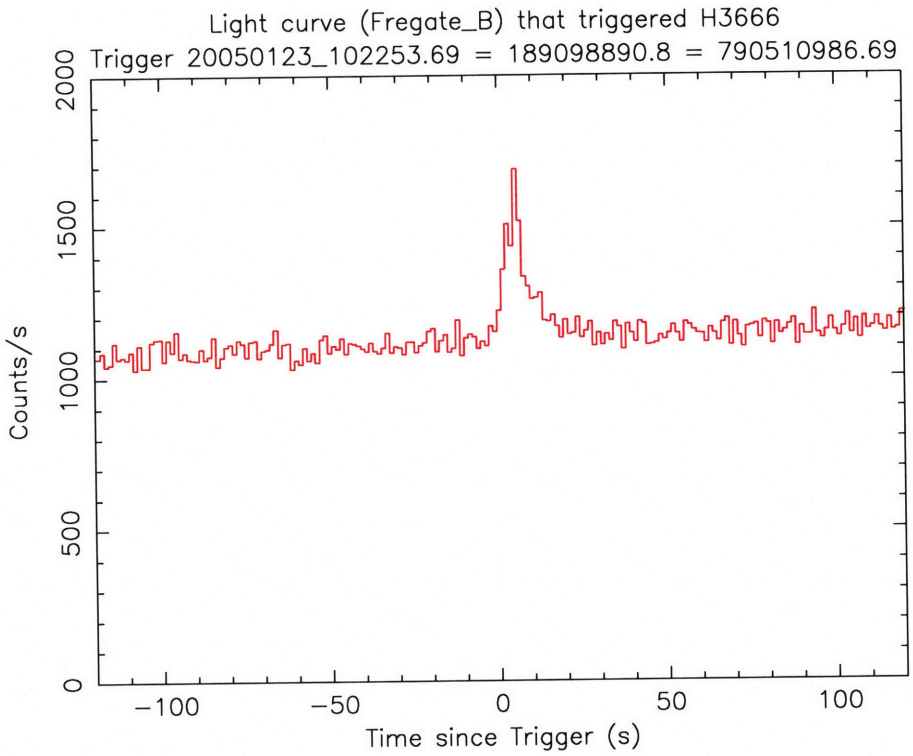

Figure 1-5: The lightcurve for BID3666 (GRB050123A) which shows that this GRB triggered onboard the HETE satellite based on the excess counts in the FREGATE band B.

The pattern in the color-color diagram also indicates that there is some regularity of the spectral properties of GRBs that ultimately is the basis for the new approach for measuring the redshift of GRBs reported in the later sections of this thesis. Figure 1-7 shows an automatic spectral analysis of BID3666 that uses the XSPEC program. The spectrum is plotted weighed by energy (continuous line) and is a fit to the measured data points shown. The peak of the model marks an E_{peak} at about 78 keV. (The value of 71 keV that is also reported for BID3666 in table A.2 is not from the automated fit, but a separate effort by Jernigan (2006)). From the spectral fit and the lightcurve (figure 1-5) the peak flux can be estimated.

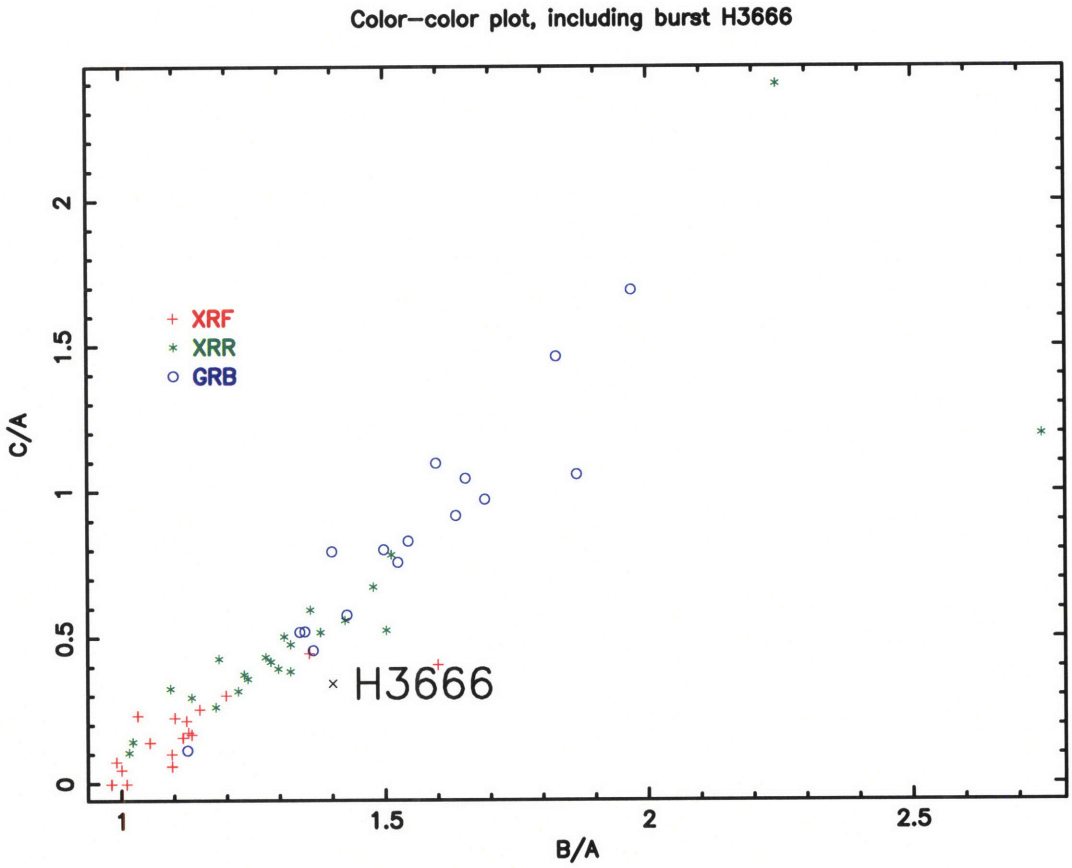

Figure 1-6: The count rates for BID3666 are computed for the A, B and C bands of FREGATE so that this GRB can be located in the color-color plane C/A versus B/A. Prior GRBs are also located in this plane for comparison. The bursts are color coded by type XRF, XRR or GRB.

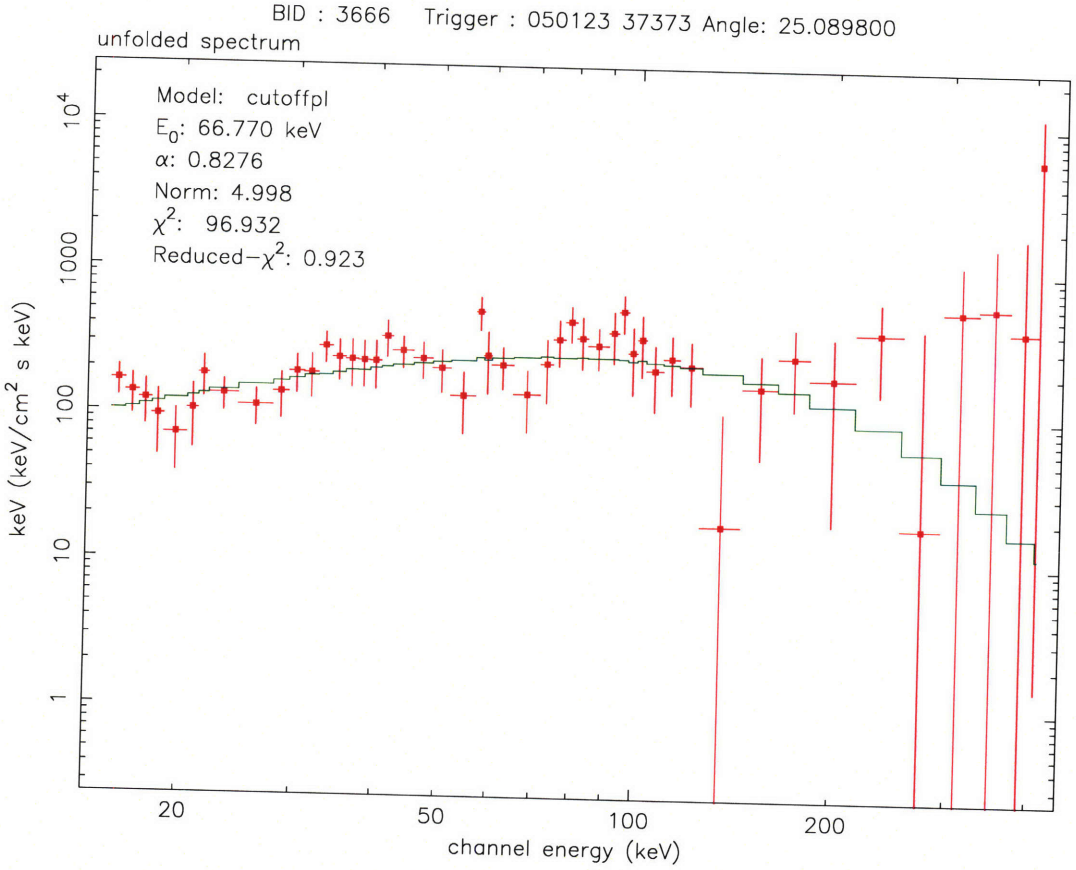

Figure 1-7: The spectral fit for BID3666 based on a cutoff power law model (eq. 1.3), generated by the automated analysis. The model is plotted as the continuous (green) line with parameters of the model in the inset. The XSPEC analysis program was used to calculate the spectral fit. The plot is weighted by a factor of energy so that the peak of the model (curve) is clearly seen at the value of $E_{peak} = 78$ keV.

Chapter 2

Background Subtraction

2.1 Introduction

To determine the duration of a gamma-ray burst, one must first estimate the background count rate during the burst and then subtract it. Typically, this background rate subtraction is performed by inspecting the light curve of the burst and determining a period of time before and after the burst for which one assumes there are no burst counts (often referred to as "bracket regions", especially in the context of "bracket" triggering). To these before and after regions one fits a polynomial model to allow the interpolation of the background rate during the actual burst. (The time during the burst is called the "foreground" region, equivalent to an "on-source" measurement.) This analytic interpolation model of the background is then subtracted from the counts in the foreground region, resulting in an estimate of the burst profile alone.

We have developed a new and alternative method for background subtraction that is based entirely on the spatial distribution of photon counts as modulated in a coded-mask detector. An important advantage of this new method is that it provides simultaneous foreground and background estimates. These estimates are formed without need for data before or after the time of the burst. The coded aperture instrument can thereby measure the time dependence of both the burst signal and the background signal without any model dependent assumptions about the background

and only minimal data.

One drawback of the traditional burst isolation method is its reliance on a qualitative inspection to determine the before and after burst regions (Koshut et al. 1996). Under ideal conditions our new method avoids this by comparing the foreground and background estimates to determine the approximate onset and end of the burst.

The work described in this chapter is an application of the algorithm using data from the WXM. However, the algorithm could be easily adapted for analyzing data from any coded-aperture instrument.

2.2 Source Models

The WXM detector response can be modeled with ray-tracing Monte-Carlo simulations which generate point-source models (so-called 'templates', see example in figure 2-1, Graziani & Lamb (2003); Fenimore (2004)). For each localized burst, the ground analysis pipeline calculates a template for that specific sky position based on a set of very high-resolution pre-computed models. We use these burst-specific models to exploit the spatial information encoded by the mask.

2.3 Using the Coded Mask

One may think of the detection using the mask as a spatial chopping or modulating measurement: by covering parts of the aperture, the mask divides the detector into a "foreground" and a "background" detector. (Note that this is now a slightly different meaning of these terms, since above, foreground and background referred to time intervals, and now they refer to parts of the detector. Nevertheless, the usage is still analogous to the traditional on-source and off-source measurements.) Which exact anode wire positions contribute to the "foreground" and which to the "background" will clearly depend on the location of the X-ray source on the sky relative to the detector axis. The spatial modulation property can be exploited in a number of ways, some of which are specific to the instrument. In the case of the WXM on *HETE-II*, if

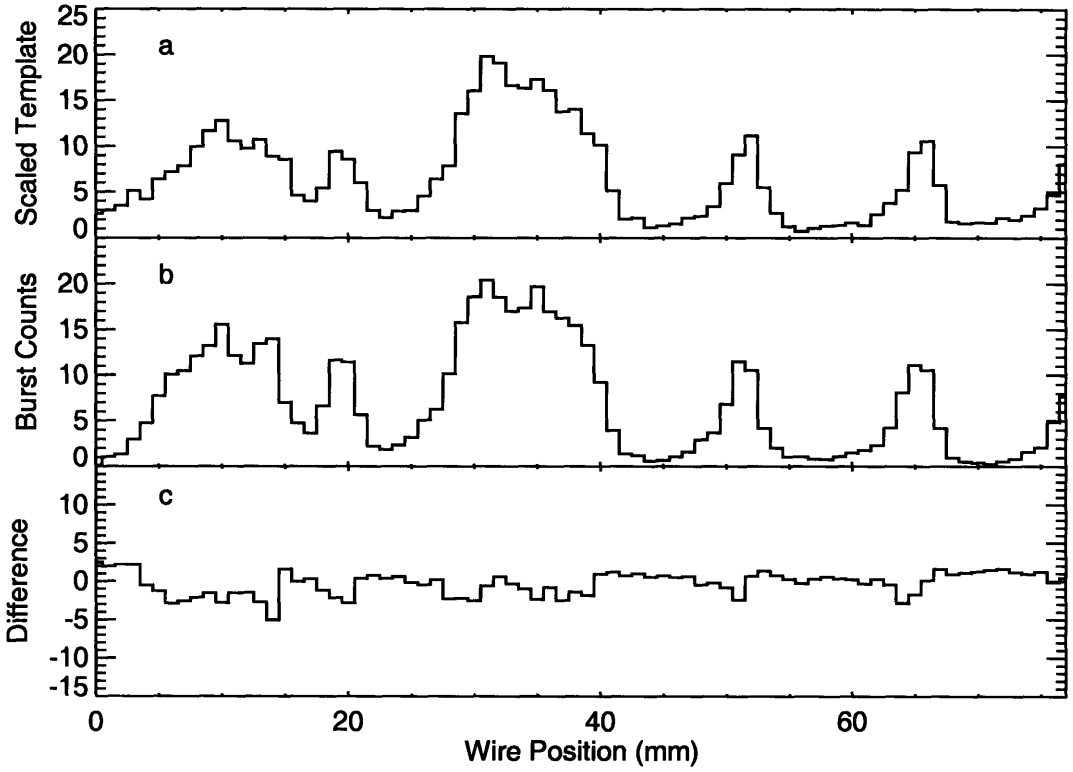

Figure 2-1: Example source model, or template. Panel a is the template for burst GRB030329 in the WXM X camera. The abscissa is the location along the proportional counter wire. The template is not a perfect pattern of ones and zeros due to the physical effects of the detector. Panel b is the actual data for GRB030329 normalized to match the template in 1a. Panel c is the difference in a and b and shows a match within the limits of Poisson noise.

the burst is far enough off-axis, one can use the wires that are not exposed (i.e., those outside the "partially coded" field of view) to estimate the background rate. Even when all wires are exposed to the source, some parts of each wire will be covered by the edges of the detector enclosure and counts recorded in these positions could be used for background estimates.

Our present method relies on the templates described in section 2.2. We sum the counts from those positions along the wires that have a low probability of recording source counts ($s \approx 0$) to estimate the background rate (b_2). We also sum counts from all other wire positions to estimate the sum of the foreground (s) and the (scaled)

background rate (b_1). Our simple model is therefore:

$$\begin{aligned} C_F(t) &= s(t) + b_1(t) \quad \text{“foreground”} \\ C_B(t) &= b_2(t) \qquad\quad\ \ \text{“background”} \end{aligned} \tag{2.1}$$

and

$$b_1(t) = \beta b_2(t) \tag{2.2}$$

where $C_F(t)$ and $C_B(t)$ are the lightcurves of the two detector regions, foreground and background, respectively, $s(t)$ is the signal, or source, $b_1(t)$ and $b_2(t)$ are the background rate in the two detector regions, and β is the scaling between $b_1(t)$ and $b_2(t)$.

In principle the scaling factor, β, could be calculated *ab initio* from the detector geometry and energy response. However, we find that it is best to determine this factor empirically from the data outside the burst, where $s = 0$. To find the position elements to include in the background b_2, we take all locations in the template where the model indicates a foreground level below some arbitrary fixed relative value.

Figure 2-1 illustrates an example template for burst GRB030329. Figure 2-3 shows burst GRB030723 as measured, with the simultaneous background determined by our method and the difference, which is the inferred source lightcurve.

2.4 Finding the Burst Time Interval

Determining emission duration statistics that are dependent on cumulative counts, such as T_{50} and T_{90}, requires that one focus attention only on the interval of time during which the burst is present, otherwise the noise in the measured cumulative will dominate and produce spuriously long (or short) burst durations. (The noise in the foreground and background lightcurves shows up in the cumulative as a component that is a random walk. The magnitude of this is a stochastic quantity dependent on the duration of the walk, so by not integrating during the source-free, $s = 0$, time intervals, we are minimizing this source of error.) In this section we discuss how

we limit the analysis to periods when the burst is present by using the estimated background and foreground rates obtained with the method of section 2.3.

What distinguishes the presence of the burst in the event data from its absence is the increase in photon count rate, or equivalently, a change in photon arrival time or inter-arrival time distributions. This implies that we may compare the rates or arrival time distributions of measurements of the same quantity at different times, or even better, between background and foreground measurements at the same time. We can apply the Kolmogorov-Smirnov (K-S) test to the simultaneous rates of section 2.3 to evaluate the hypothesis that a burst is present in the data. The null hypothesis is that there is no burst present and the photon arrival times in the foreground and background are distributed identically, yielding a K-S D-statistic probability close to 1. The null hypothesis is rejected when the burst is present and the D-statistic probability tends toward zero.

We know *a priori* that a burst is present in the data since we are analyzing GRBs that were previously localized by the WXM. Therefore we expect the null hypothesis to be rejected for some portion of the data. If it is not rejected, then we know that the GRB is not confirmed and we do not proceed with the determination of T_{90} or T_{50}. Assuming that the null hypothesis is rejected and that the burst is real, we address the determination of the start and end times of the burst by calculating the K-S probability as a function of both the duration of the data window (a limited time segment used to sample the time distribution of photons) and the midpoint of the data window in time. This corresponds to considering all possible foreground time regions to determine the largest range of data that includes emission from the burst.

In general, this search for the correct foreground region would occur in a two-dimensional space parametrized by the data window duration and its center point in time, or equivalently, by the start and end point of the foreground region. (We call these points in time t_0 and t_{100}). In practice we choose the data window size to be a fixed fraction (1/100) of the TAG data buffer length and search only one dimension. We look for the point in time where the null hypothesis is first rejected, starting at the beginning and sliding the window toward the end, then search for the point

where the null hypothesis is last rejected by working from the end. We typically use a probability level of 10^{-2} or less to determine the onset and end of the burst. See figure 2-2. In some cases we have to adjust this level if the probability values show large variance.

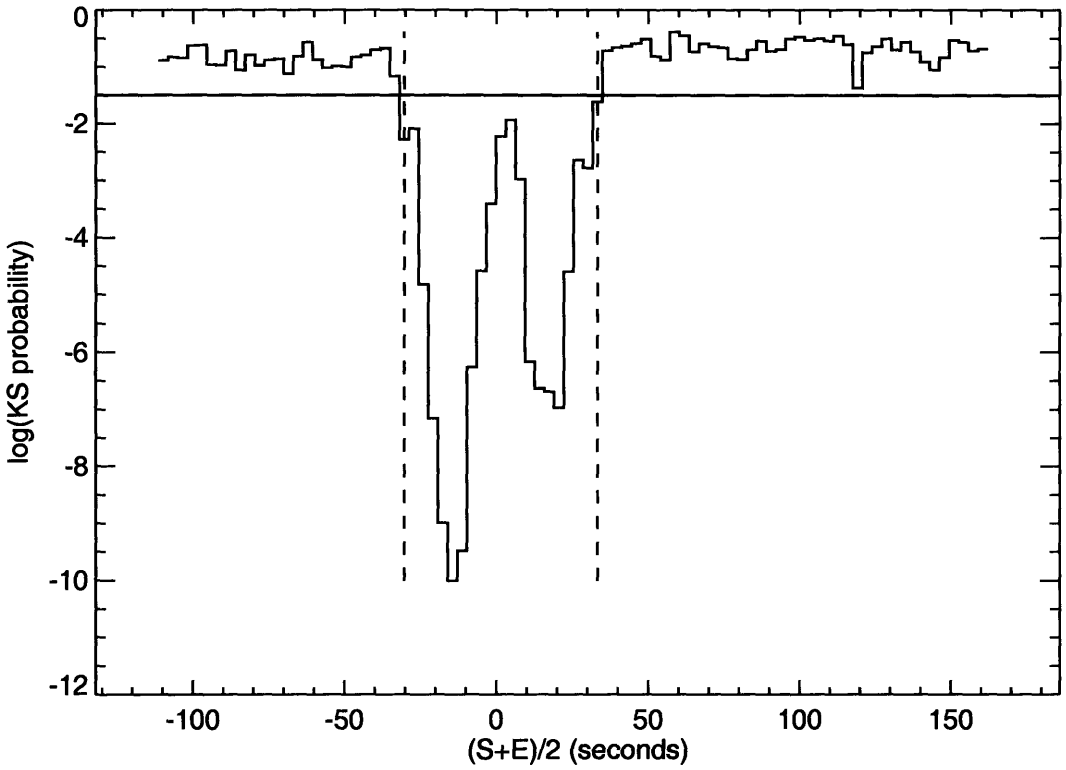

Figure 2-2: Determination of the burst foreground time region. Plotted is the logarithm of the K-S probability as a function of the midpoint of the data window in time relative to the burst trigger. The discrete steps show that the calculation splits the buffer into 100 time intervals for K-S comparison of the background and foreground. The horizontal solid line indicates the probability level we take to reject the null hypothesis (no burst), and the vertical dashed lines indicate the derived foreground region bounds (we extend this by one more data window step in both directions to get lower and upper time bounds.) The increase in probability in the middle is due to the K-S test distinguishing between distributions of count times, not rates, thereby functioning as a burst "edge detector".

We do not worry about finding the exact start and end of the burst but aim to find lower and upper bounds, respectively, because if we have correctly estimated the background rate, the analysis of duration measures described in chapter 3 will be robust against small changes in foreground start and end times. A major advantage of using the K-S test to compare the arrival time distributions is that it is sensitive only

to the fluctuation in time of the photon rates and insensitive to the mean level of these rates, so the background rate estimate need not be scaled relative to the foreground rate for comparison, as long as enough events are included in the window sample to use in a two-sample K-S test. In other words, we do need the value of the scaling parameter β in equation 2.1 for this initial step of the algorithm. However, once a lower bound of the foreground region is found, the β parameter can be estimated from the data prior to it.

2.5 Background Subtracted Lightcurves

As discussed in section 3.3, we use the TAG event-based data product for our analysis. Subtracting background from foreground rates in this case can only be done in the sense of a cumulative as a function of time that is incremented at each event in the foreground and decremented at each event in the background. A complication arises from the fact that the rate of background counts b_1 and b_2 differ by a factor β (equation 2.1). We find β by simply dividing the number of events in the foreground by the number of events in the background *outside* the burst interval determined with the K-S test, as mentioned in section 2.3. We find it is sometimes necessary to fix this region manually when the bootstrap error calculation is applied (section 3.4). With β determined, we need to scale the background rate b_2 by this scalar to get βb_2. We do this by calculating a set of interpolated photon arrival times during the burst time interval, and adding background events at these times to the analysis. This has the effect of scaling the rate without adding excess noise. For purposes of plotting we may bin the data but our analysis of the TAG data is always event- or cumulative-based.

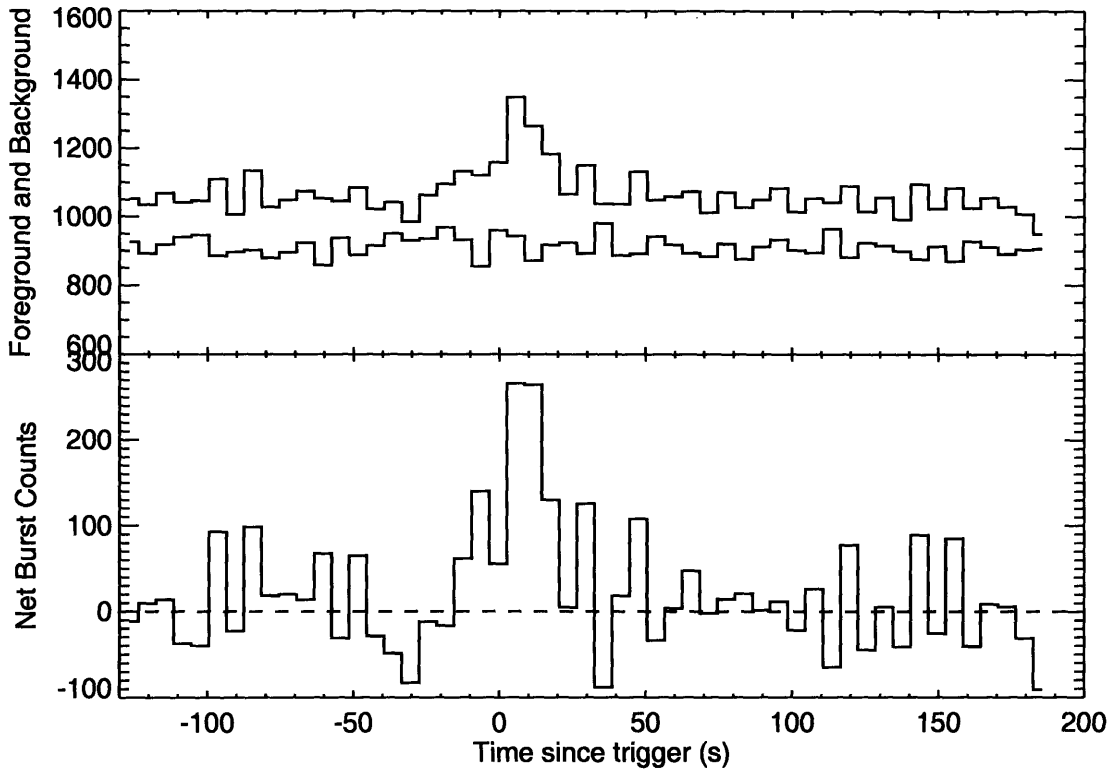

Figure 2-3: Background subtraction applied to GRB030723. Top panel shows the signal and the background for GRB030723 separated into two components (s+b_1 and b_2). S is the signal in the burst, b_1 is the background component measured with s and b_1 is the independent estimate of the background. The lower panel shows the net estimated signal, s+b_1-βb_2, where β is a normalization $\beta = \langle b_1 \rangle / \langle b_2 \rangle$.

Chapter 3

Burst Temporal Parameter Estimation and Error Analysis

The definition of T_{90} and T_{50} provides a convenient recipe for their calculation using the empirical cumulative distribution function of the incident counts in the detector: T_{90} is the time the cumulative of the background subtracted lightcurve spends between 5% and 95% of its maximum, and analogously for T_{50}. Implementing this simple calculation is complicated mostly by the ambiguity in the starting and ending times, the appropriate background rate to subtract (which may be rising or falling), and by the calculation of the errors. Errors are often estimated by adding Poisson deviates to the measured binned time-series count data, recalculating the cumulative and duration parameters of interest.

In contrast, the new method is a purely event-based statistical bootstrap. This means that multiple realizations of the burst are made from the time-tagged photon data by resampling the event times as described below in section 3.2. For each such realized data set, we calculate the cumulative function and the derived T_{90} and T_{50} duration measures (figure 3-1). The histogram of all realizations of these values will be the expected error distribution of T_{90} and T_{50}, and the confidence regions in these quantities may be determined by finding the ranges that enclose the desired percentage of all realizations. Figure 3-2 shows the procedure applied to GRB030723.

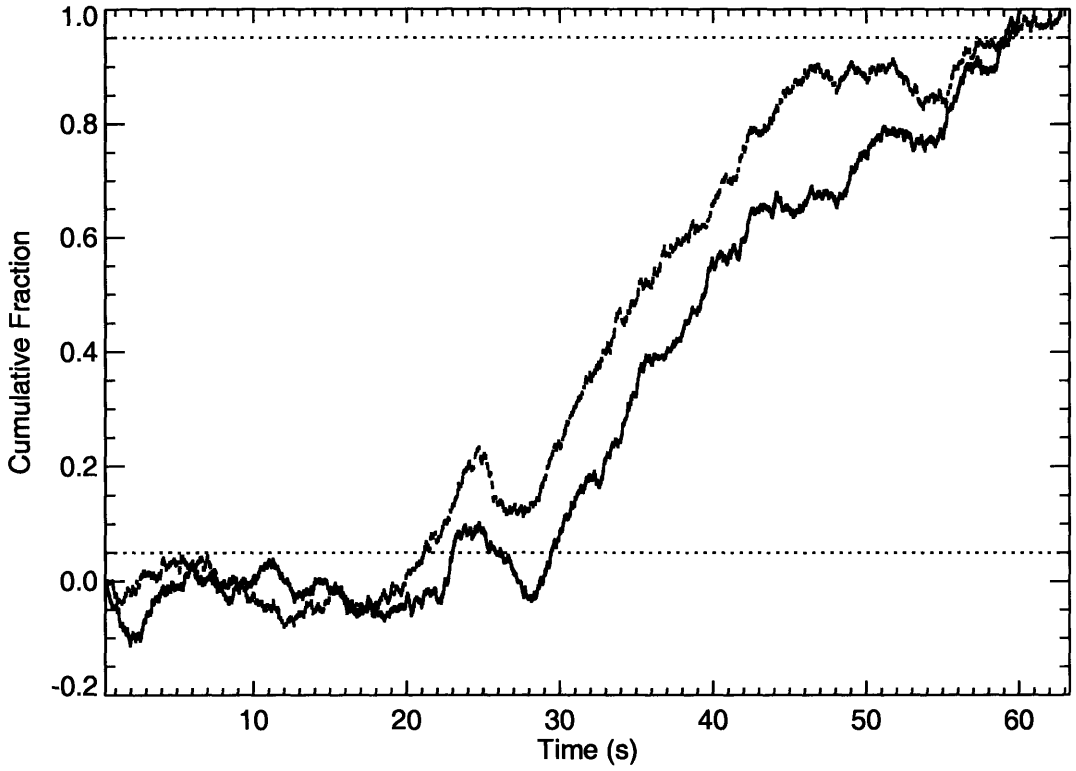

Figure 3-1: The cumulative percentage of counts as a function of time. Plotted with dashed lines is another bootstrap realization of the burst GRB030723. Dotted lines indicate the 5% and 95% fluence levels.

3.1 Duration Measures

Duration measures and their distributions are important statistics of gamma-ray bursts. They lend insight into the energetics ($E_{\rm iso}$) and also provide a basis for discrimination of potential source models. Since the *BATSE* experiment on the Compton Gamma Ray Observatory mission, T_{90} and T_{50} have become the *de-facto* standard measures of burst duration. They are defined as the time elapsed during which the background subtracted burst counts rise from five to 95 percent, and 25 to 75 percent, respectively, of the total burst count fluence. (Kouveliotou et al. 1993; Koshut et al. 1996). The distribution of these duration measures show a bimodality which has led to the belief that there are at least two distinct progenitor classes of gamma-ray bursts.

Another duration measure, defined by Reichart et al. 2001, is the "high-signal

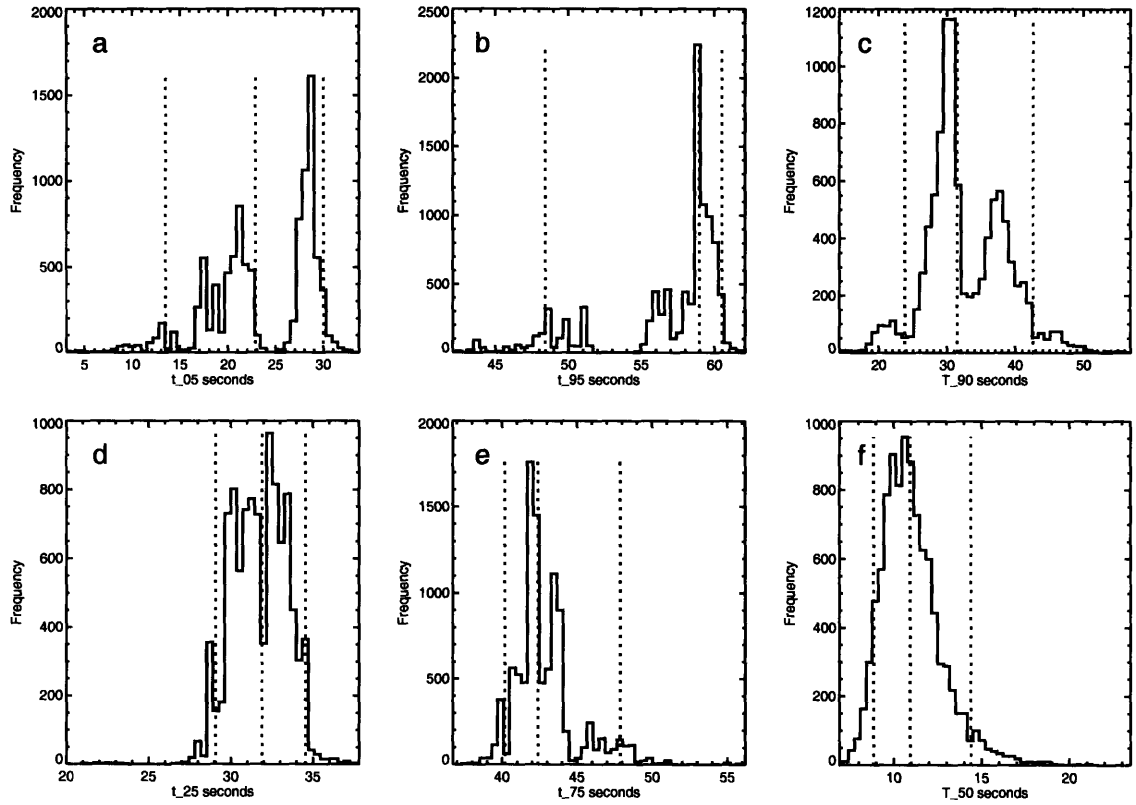

Figure 3-2: Panel a) is a histogram of the t_5, the 5% count fluence time derived from multiple bootstrap realizations of the burst GRB030723. Panel b) is the histogram for t_{95}, defined similarly. Panel c) shows the histogram of differences, $t_{95} - t_5$ which is T_{90}. Panels d) through f) are the corresponding histograms for t_{25}, t_{75} and T_{50}. Indicated by vertical dashed lines are the median values and the boundaries of regions where 90% of the realizations fall.

timescale", designated T_f. This is the time elapsed during the brightest f fraction of the total counts above background for the burst. (We can distinguish this from measures like T_{90} by expressing f as a quantity less than 1.) The high-signal counts need not occur continuously, and for multiple-peaked bursts they generally will not. Reichart et al. (2001) use T_f as a smoothing timescale for burst lightcurves then with the help of smoothed lightcurves they calculate a variability statistic that is correlated with (and is a predictor of) the burst luminosity. When optimizing the fraction f to give a robust and low-variance luminosity estimator, Reichart et al. (2001) typically find $f = 0.45$. Firmani et al. (2006c) also investigate the variability indicator, but use $T_{0.45}$ as an independent variable, and surprisingly find $L_{\rm iso}$–$E_{\rm pk}$–$T_{0.45}$ to be a

much tighter correlation than those using variability. It is also true that the signal to noise of WXM GRBs is insufficient for the reliable calculation of variability, but *is* sufficient for the calculation of $T_{0.45}$. To take advantage of this use of $T_{0.45}$, we develop our similar event-based statistic as described below.

3.2 Statistical Bootstrap

We use a non-parametric bootstrap method for the analysis of the WXM X-ray photon data, and in particular, for the analysis of errors of our duration estimates. The bootstrap in statistics was first put forward by Bradley Efron (Efron 1979, 1982), and belongs to the class of resampling techniques. The fundamental idea is that in the absence of being able to repeat an experiment or an observation (such as a gamma-ray burst), the existing measurements are resampled to form synthetic data sets.

Resampling means that we take *random* samples from the data that we have already measured. For a bootstrap dataset, the number of random *re*-samples, is equal to the number of original measurements. A key feature of this statistical method, is that it is possible to randomly select the *same* sample over and over again. This is why the method is often called resampling with "replacement" (as if one were pulling balls at random from an urn, noting which ones were picked, then placing them back in the urn before pulling the next one at random, unlike what happens in a lottery).

For illustration, suppose one makes four measurements of x. The measured sample is then $\mathbf{x} = (x_1, x_2, x_3, x_4)$. One resampling could be $\mathbf{x}^{*1} = (x_2, x_4, x_1, x_3)$, although this is very unlikely, since each original sample was randomly selected again. This sample is also entirely equivalent to the original data, $\mathbf{x}$. Another resampling might be $\mathbf{x}^{*2} = (x_3, x_1, x_4, x_1)$. Note that x_1 was resampled twice.

The analysis to be done on the data, i.e., whatever statistic we are interested in, is then applied to the synthetic data sets just as it would be applied to the original data. The distribution of the statistic is then calculated as its distribution over the synthetic data sets.

The bootstrap idea is illustrated in figure 3-3. It differs from Monte-Carlo methods

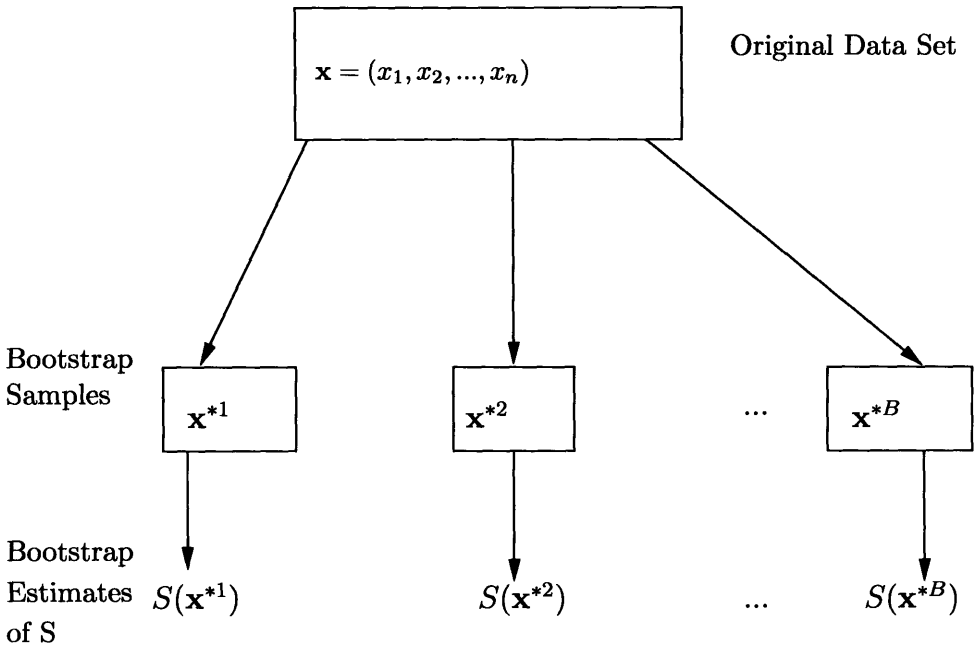

Figure 3-3: Illustration of the bootstrap method (after Efron, B. and Tibshirani, R. 1993). The original data set of n items is resampled with replacement to create B synthetic data sets, $\mathbf{x}^*$, each with n elements. The statistic S is calculated on each of the synthetic data sets.

in that it does not assume an underlying distribution of the data, but rather uses the measured data as the best estimate of their distribution.

3.3 Event Data

The TAG data product of the WXM instrument is particularly suitable for bootstrap analysis. It provides information at the level of each individual photon detected: the energy channel, the position along the detector wire, the wire itself (which also determines the camera, X or Y, that it was detected in), and most importantly, the time of detection with 256 μs resolution. The TAG data are stored in a circular buffer on the spacecraft, which limits the maximum duration recorded. When a burst is triggered on board, the content of the buffer is unmodified until it has been telemetered, with the time of trigger approximately in the middle of the buffer.

3.4 Applying the Bootstrap to the Data

The suitability for bootstrap analysis is due to the unbinned, event-nature of the data. Each recorded time corresponds to a single photon event and we can resample by randomly selecting the individual photons. The bootstrap is performed by re-sampling the event times with replacement for both the foreground and background event streams. For each such realized data set, we calculate the empirical cumulative function and derive the T_{90} and T_{50} duration measures (figure 3-1). The histograms of all realizations of these values will be the expected error distributions of T_{90} and T_{50}, and the confidence regions of these quantities may be determined by finding the ranges that enclose the desired percentage of all realizations. Figure 3-2 shows the procedure applied to GRB030723 and Table 3.1 summarizes the results. Note that the bootstrap method shows the non-Gaussian nature of the errors (see panel 3-2 c) and the 5% and 95% values in table 3.1 are not consistent with Gaussian assumptions and the medians and variances listed.

Measure	5%	95%	Median	Variance
t_{05}	13.47	30.00	22.90	28.95
t_{95}	48.44	60.52	58.98	17.08
T_{90}	23.83	42.65	31.51	34.20
t_{25}	29.06	34.54	31.90	2.95
t_{75}	40.18	47.88	42.39	4.57
T_{50}	8.84	14.38	10.92	3.10

Table 3.1: Summary statistics of duration measures for GRB030723 (see figure 3-2)

Smoothing

Before applying a statistical bootstrap procedure to find the confidence regions, we may smooth the data (which are still just an ordered list of detection times) by assigning each event a time that is the mean of the times of the n^{th} event before and the n^{th} event after the one in question. (That is, $t'_i = (t_{i-n} + t_{i+n})/2$, where t_i indicates the time of the event, i is the index of the events in chronological order, and t' is the smoothed time.) The typical value of n is 50. This procedure preserves time order and narrows the distribution of inter-arrival times (thereby smoothing

the data). In other words, we construct an approximate infinite statistics version of the GRB profile by removing some of the photon shot noise in groups of n nearby photons. This approach has the advantage that is temporally adaptive in the sense that the smoothing tracks variations in signal-to-noise such that bright portions of a GRB lightcurve are smoothed less than faint portions.

Using the K-S Test with the Bootstrap Technique

Care must be taken with applying the K-S statistic to the synthetic data sets of the bootstrap. The two-sample K-S test works for the original data since it is measured with Poisson statistics and the K-S D-statistic is distributed as is described in textbooks. However, the creation of the synthetic bootstrap datasets adds extra variance, which must be accounted for. We have shown for these cases with numerical experiments that the D-statistic is *not* distributed uniformly in the case of the null hypothesis, as would be required to apply the probability cuts. Our solution is to change the test by evaluating the probability for a given D-value, but assuming there are half as many points in the K-S test, which would also increase the variance. Using the same numerical experiments, we showed that the D-statistic is distributed approximately uniformly with this correction, and so we may use the corresponding probability value.

3.5 $T_{0.45}$ Measurements

The T_f burst timescales, where f represents a fraction between 0 and 1, were proposed as smoothing timescales for lightcurves by Reichart et al. (2001) in constructing a Cepheid-like variability estimator. The quantities represent the total duration of the highest f fraction of the background subtracted counts. The definition is illustrated schematically for idealized lightcurves in figure 3-4 for $f = 0.5$ and $f = 0.9$. Reichart et al. found that the optimal choice for f was close to 0.45, which was then used in a different context by Firmani et al. (2006c) in establishing the $L_{\rm iso}$–$E_{\rm pk}$–$T_{0.45}$ relation (section 4.3). Motivated by the above definition, we calculate our own similar statistic

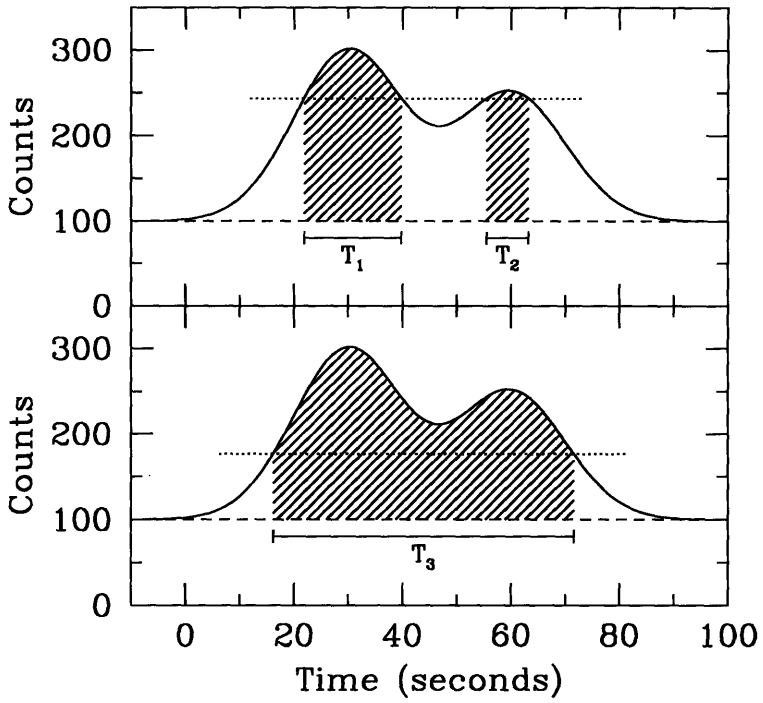

Figure 3-4: Illustration of T_f for schematic lightcurves from Reichart et al. (2001). The top panel shows $f = 0.50$ and the bottom $f = 0.90$. Note the total duration $T_{0.50} = T_1 + T_2$ is made up of discontinuous segments, whereas $T_{0.90} = T_3$ turns out to be one continuous interval.

using event-based methods that we apply to time-tagged data. During times of bright emission, the cumulative of net burst counts rises steeply, that is, takes less time to change by some fixed fractional amount. To find our version of $T_{0.45}$, we calculate the time it takes for the cumulative to reach 5%, 10%, ..., 100% of its maximum ($t_5, t_{10}, ..., t_{100}$ in our notation), take the differences (Δt_i), and sum the shortest 9 intervals. This calculation is easily generalized to shorter but more time intervals, however increasing the number of intervals to get finer resolution has the disadvantage of making the results noisier. Obviously, 5% intervals are the largest with which a 45% smoothing timescale can be calculated. We find the errors on the derived $T_{0.45}$ by applying bootstrap to the lightcurve. An example of the procedure is shown in the bottom panel of figure 3-5. Section 4.3.1 shows a comparison of our event-based $T_{0.45}$ to the traditional binned method used by Firmani et al.. But care should be taken in the interpretation since the data analyzed are from different instruments,

and Firmani's detailed analysis method is unknown to us.

3.6 WXM T_{90}, $T_{0.45}$ Measurements and Error Distribution

We measured the T_{90} (and T_{50}) of all the bursts detected in the WXM with available TAG data. We define the fractional error in the duration measures as the standard deviation of the bootstrap realizations divided by their median. $\delta T_x/T_x$. Discussion of the distributions of the duration measures and their errors is deferred until chapter 5, because we also consider the intrinsic distribution of these quantities, i.e., corrected for cosmological time-dilation and energy-bandpass effects, using the redshifts found in chapter 4.

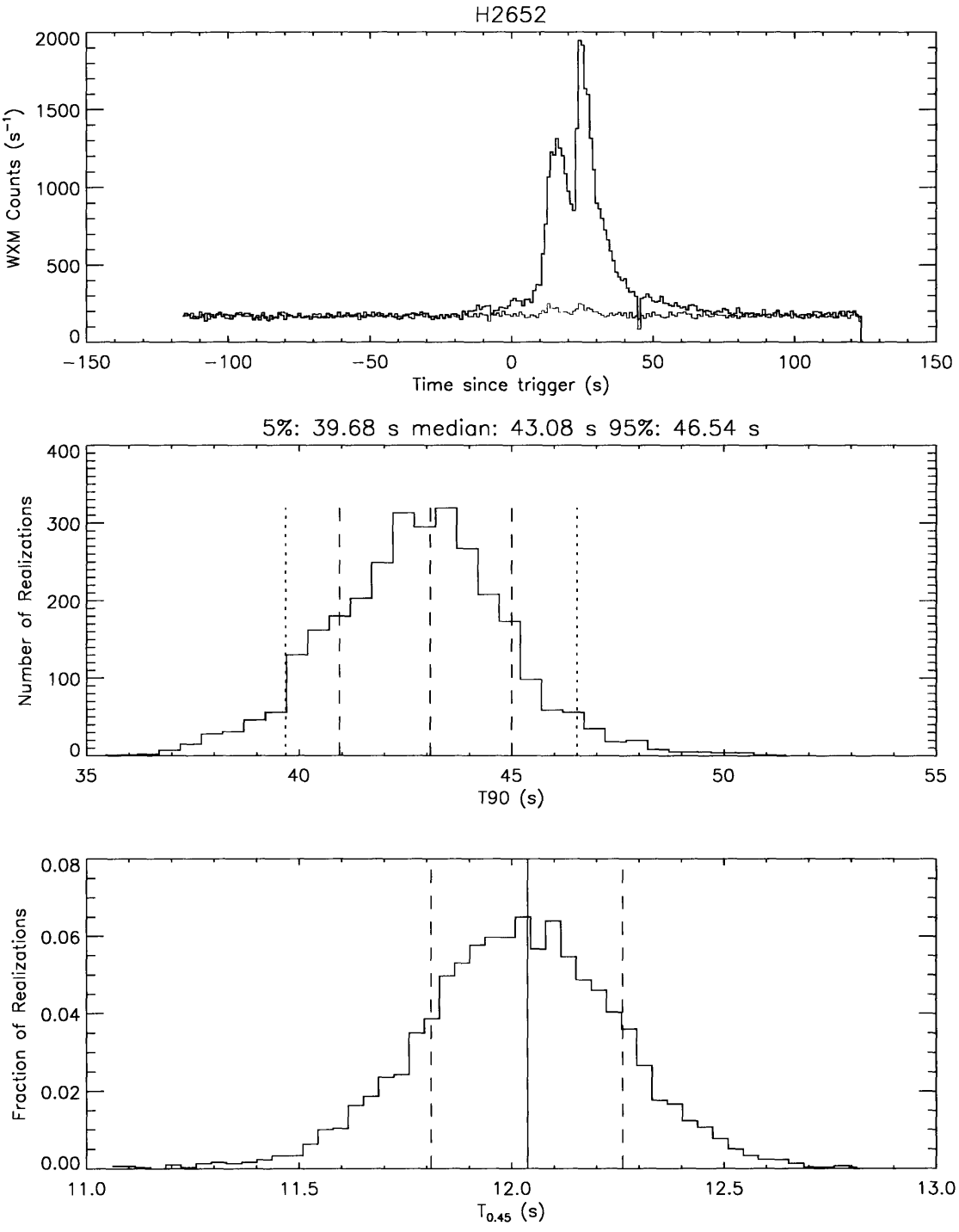

Figure 3-5: Example $T_{0.45}$ and T_{90} calculation with errors for GRB030329. The top panel shows the burst lightcurve and the background rate (green curve). The middle panel shows the T_{90} distribution, the dashed lines indicating the median and one standard deviation values, and the dotted lines bounding the 90% confidence region. The bottom panel shows the $T_{0.45}$ distribution, the vertical solid line indicating the median value and the dashed lines showing one standard deviations. Note that the binning is for plotting purposes only. The vertical axis of the bottom panel is normalized by the number of bootstrap realizations, and may be interpreted as a probability.

Chapter 4

GRB Luminosity Function and Redshift Distribution

4.1 Introduction

In this chapter we describe analyses of *HETE-II* data that attempt to characterize GRBs by finding their distribution in luminosity and space. There are two reasons why these questions must be treated simultaneously. The first is that the raw distributions of these properties are affected by the flux limit of the detector, and since more luminous objects will be visible to larger distances, corrections to number counts must be made. The second reason is that we allow for the possibility that the luminosity distribution evolves with cosmic time, or redshift.

We first describe how it is possible to infer a redshift for bursts that have no spectroscopic measurements, and why this is important. We then apply such a method to WXM bursts to create a catalog of GRBs with peak luminosities and redshifts. We proceed with non-parametric techniques to determine the evolution of the luminosity function under some simplifying assumptions, and the shape of the luminosity function and redshift distribution of GRBs. This analysis carefully includes the effects of the large log-normal errors of the estimated redshifts. Finally we compare to other results and discuss the implications.

4.2 Redshift Estimators

The number of GRBs with spectroscopic redshift measurements has been steadily increasing but is still a small fraction of all the bursts detected. This is most likely due to observational selection effects that are hard to quantify; as evidence of this, one sees that the distribution of spectroscopic GRB redshifts obtained from different satellites varies greatly. For example, after a little over a year of operation, it is seen that *Swift* GRBs have higher mean redshifts than those of *BATSE* or *HETE-II*, and *Swift* may be lacking low redshift bursts. Some of the biases originate in the instruments or their operations (for example optimal orientation for optical follow-ups) and some are selections on the properties of bursts or their host environments (speed of decay of the afterglow, the redshift of the burst, optical column density, etc.) For these reasons, that is, to have a larger and more complete sample of bursts, and to avoid selection biases, it is desirable to have a method of measuring redshifts other than via optical spectroscopy. We refer to these methods as *redshift indicators* or *redshift estimators.*

Redshift estimators are most often constructed using observed phenomenological correlations between gamma-ray burst properties and luminosity. (These correlations are established with bursts that have spectroscopic redshifts, therefore these function as calibrators.) Redshifts may then be calculated given an assumed cosmology, typically the concordance model. Useful estimators involve observer frame quantities, and most useful are those that are derived from the prompt X-ray or γ-ray data alone.

Some of the commonly used estimators are based on the lag-luminosity, variability-luminosity, $E_{\rm pk}$–$E_{\rm iso}$ (Amati) and $E_{\rm iso}$–$E_{\rm pk}$–$t_{\rm break}$ (Ghirlanda) correlations. This last relation is less useful in practice since the jet break times of the bursts often proves to be unmeasurable. The Amati relation has been criticized for having a large degeneracy region in redshift and thereby being unable to differentiate redshifts in the range $0.9 < z < 20$ given the typical one standard deviation errors of the energy estimates (Li 2006).

The $L_{\rm iso}$–$E_{\rm pk}$–$T_{0.45}$ relation, discussed in section 4.3, is a recently reported corre-

lation, which when used to infer redshifts, produces low redshift errors (68% of the calibrator redshift estimates are within 25% of the real values) and the relative uncertainties of the redshift estimates seem uncorrelated with redshift (Firmani et al. 2006c).

4.3 $L_{\rm iso}$–$E_{\rm pk}$–$T_{0.45}$ Relation

Using a total of 27 bursts detected by a number of different missions, all with spectroscopic redshifts, Firmani et al. (2006c) investigate the existence of possible correlations between $L_{\rm iso}$, $E_{\rm iso}$, $t_{\rm break}$, $T_{0.45}$, $E_{\rm pk}$, and variability measure (Reichart et al. 2001). They find for a subset of 19 bursts (for which all the observables are available), a correlation between $L_{\rm iso}$, $E_{\rm pk}$, and $T_{0.45}$ with a remarkably small scatter of 0.06 dex (Firmani et al. 2006c, Eq.9):

$$L_{\rm iso} = 10^{52.11\pm0.03}\left(\frac{E_{\rm pk}}{10^{2.37}\,{\rm keV}}\right)^{1.62\pm0.08}\left(\frac{T_{0.45}}{10^{0.46}\,{\rm s}}\right)^{-0.49\pm0.07}\ {\rm erg\ s^{-1}} \quad (4.1)$$

Firmani et al. note that there are outliers to the relations that were not fitted; these were all low luminosity GRB events (below $L_{\rm iso}$ of $\sim 10^{51.2}$erg s^{-1}) and had peculiarities in their spectral fits with indications that $E_{\rm pk}$ might be lower than first reported.

The quantities in equation 4.1 refer to source frame quantities and to infer an $L_{\rm iso}$ for a burst, one must adjust the observations by the appropriate factor of $(1+z)$: $E_{\rm pk} = E_{\rm pk}^{\rm obs}(1+z)$ and $T_{0.45} = T_{0.45}^{\rm obs}/(1+z)$. But note that the emission time is also affected by the shortening of temporal features at higher energies (Fenimore et al. 1995), so what we observe is $\tilde{T}_{0.45}^{\rm obs} = T_{0.45}(1+z)^{0.6}$.

Redshift Estimation

We now see how the relation can yield burst distances, or redshifts, for those with no spectroscopic measurements. Having established the correlation, one has the ability

to infer $L_{\rm iso}$ from the prompt emission data, and by using the observed bolometric peak flux, P, one can calculate the redshift of the burst by inverting the luminosity distance, since $4\pi D_L^2(z)P = L_{\rm iso}$. We stress that this relation applies to bolometric quantities, and so in practice one has to k-correct (Bloom et al. 2001) the measured peak flux to a sufficiently wide energy band. Firmani et al. choose to use 1-10^4 keV in the source rest frame, which is quite common in the literature. (The k-correction also allows the simultaneous use of observations from different detectors, although this is not important for the analysis of our data described in the sections below.)

Equation 4.1 can then be cast in terms of the observables as

$$L_{\rm iso} = 10^{52.11\pm0.03} \left(\frac{E_{\rm pk}^{\rm obs}\,(1+z)}{10^{2.37}\,{\rm keV}} \right)^{1.62\pm0.08} \left(\frac{\tilde{T}_{0.45}^{\rm obs}}{(1+z)^{0.6}\,10^{0.46}\,{\rm s}} \right)^{-0.49\pm0.07} {\rm erg\ s^{-1}} \quad (4.2)$$

This can then be rewritten to separate out the redshift dependence (using the best-fit values of the exponents) as

$$f(z) = 10^{6.48}\Psi \quad (4.3)$$

where

$$f(z) = \frac{(1+z)^{1.91}}{4\pi D_L^2(z)}, \quad (4.4)$$

$$\Psi \equiv \frac{P(\tilde{T}_{0.45}^{\rm obs})^{0.49}}{{E_{\rm pk}^{\rm obs}}^{1.62}}, \quad (4.5)$$

$D_L(z)$ is the luminosity distance in Gpc, P is the peak flux in erg cm^{-2} s^{-1}, $E_{\rm pk}^{\rm obs}$ is the peak of the energy spectrum in keV and $\tilde{T}_{0.45}^{\rm obs}$ is the high-signal timescale in seconds. The redshift can then be estimated through

$$z' = f^{-1}(10^{6.48}\Psi). \quad (4.6)$$

The success of this approach is illustrated in figure 4-1 (Firmani et al. 2006c) which shows the function $f(z)$ and the actual location of the GRBs with spectroscopic redshifts (those used to establish the $L_{\rm iso}$–$E_{\rm pk}$–$T_{0.45}$ relation) in the Log(Ψ)–Log(z) plane.

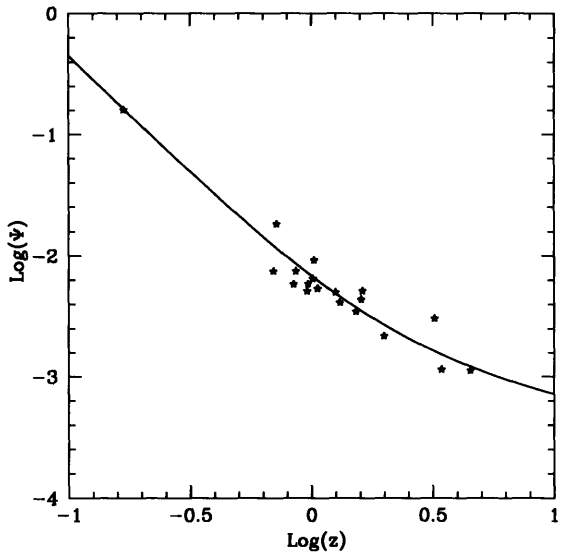

Figure 4-1: Redshift estimation with the Firmani relation (from Firmani et al. 2006c). Graphical illustration of using equation 4.6 to determine redshifts. The solid curve is the function $f(z)$ (equation 4.4). Redshifts are estimated by calculating Ψ from observables (equation 4.5) and determining the z coordinate at which $f(z)$ takes on that value. Also plotted are the points for the bursts used to establish the Firmani relation at their actual spectroscopic redshifts.

Errors in Redshift Estimates

As noted in section 4.2, the errors in the redshift estimates are lower for the Firmani relation than for most other redshift estimators (e.g., Amati). We investigate the effects of the errors in the exponents of equation 4.2. Parametrizing the exponents so that $L_{iso} \propto 10^{\alpha} {E_{\rm pk}}^{\beta} {T_{0.45}}^{\gamma}$, the equation $f(z) = 10^{6.48}\Psi$ becomes:

$$\frac{(1+z)^{\beta-0.6\gamma}}{4\pi D_L^2(z)} = K^2 \times 10^{(2.37\beta+0.46\gamma-\alpha)} \frac{P}{\left(E_{\rm pk}^{\rm obs}\right)^{\beta} \left(\tilde{T}_{0.45}^{\rm obs}\right)^{\gamma}} \tag{4.7}$$

where K is the conversion to cm from Gpc, $\alpha = 52.11 \pm 0.03$, $\beta = 1.62 \pm 0.08$, and $\gamma = -0.49 \pm 0.07$. Note that the solution for z in this equation will in general depend on the burst quantities $E_{\rm pk}$ and $T_{0.45}$ in addition to the parameters α, β, and γ (the dependence on the cosmology through the luminosity distance is assumed to be fixed). Therefore we could proceed by taking specific bursts and estimating the effects of errors in the exponents on z, or by assuming typical values for $E_{\rm pk}$ and $T_{0.45}$. We

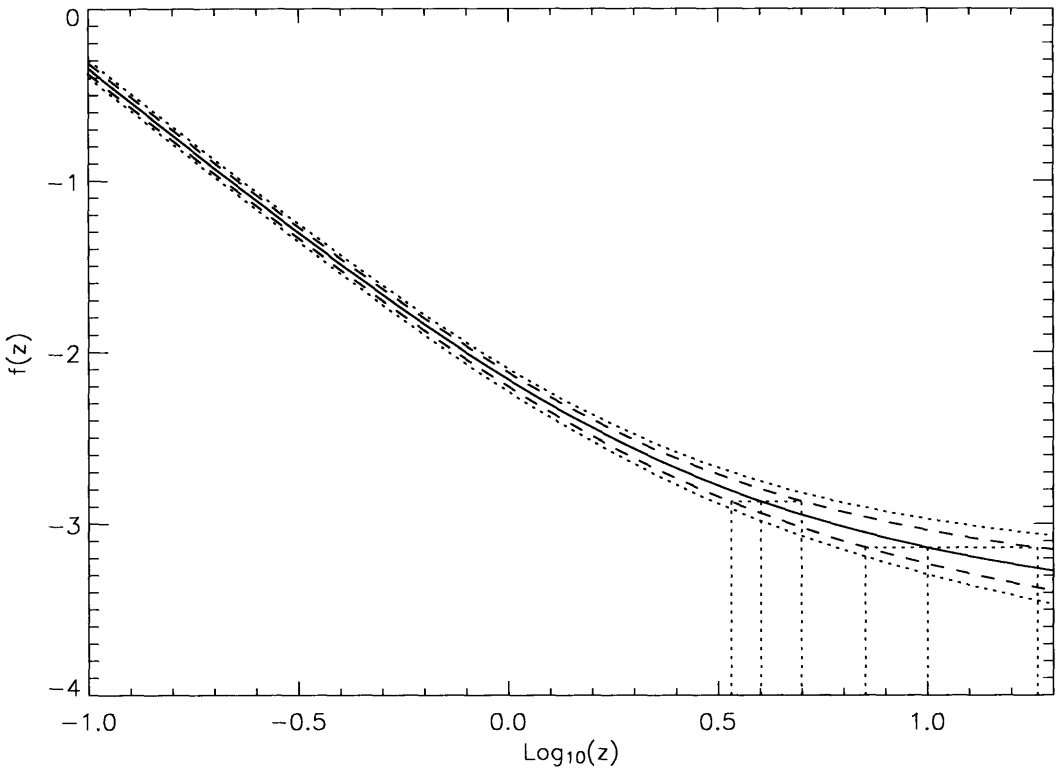

Figure 4-2: Errors in redshift estimates due to the uncertainty in the exponents of the Firmani relation. The solid curve is the function $f(z)$ with the best-fit parameters (equation 4.4). The dashed and dotted lines indicate the one and two standard deviation regions for $f(z)$ due to the uncertainty in the exponents. The effects are seen to be pronounced at high redshifts. The vertical dotted lines indicate that an inferred redshift of 4 has a one sigma logarithmic error of -0.071/+0.097 and at a redshift of 10 this increases to -0.149/+0.262.

choose the latter method and perform a Monte-Carlo study by drawing the exponents from normal distributions with mean and standard deviation as given above, and recalculating $f(z, \alpha, \beta)$ (the left side of equation 4.7). Note that to compare the results graphically on the same plot, one has to account for the fact that a change in α always shifts the effective $f(z)$ curve along the vertical axis, but if $E_{\rm pk}^{\rm obs} = 10^{2.37}$ keV and $T_{0.45}^{\rm obs} = 10^{0.46}$ s, then to first order the curve does not shift due to changes in β and γ. We pick these values as the typical $E_{\rm pk}$ and $T_{0.45}$, and find the results of figure 4-2. The confidence region for z is always larger on the high side of the best estimate than on the low side, and is larger at higher redshifts in general. For $z = 5$, the error is between 0.086 and 0.12 dex, but at $z = 10$ this increases to between 0.15

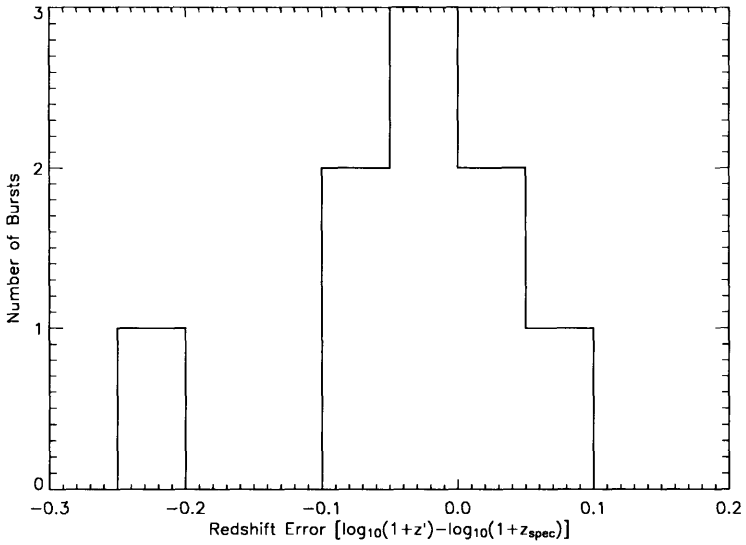

Figure 4-3: Differences in estimated and spectroscopic redshifts. We model this as a log-normal in (1+z) with a standard deviation of 0.093 dex.

and 0.26 dex.

Another way to assess the errors of the redshift estimates is to look at how close they are to the actual spectroscopic measurements (the 'residuals'). In our sample there are nine bursts with spectroscopic redshifts, and the differences are found to have an RMS scatter in $\log(1+z)$ of 0.093 dex (see figure 4-3). This is the model and the magnitude of the errors that we use in subsequent analyses. Note that the foregoing discussion and figure 4-2 are consistent with this view up to a redshift of 5, though one might be tempted to think that the error is lower at smaller z. We believe that the residuals approach takes into account sources of error other than the uncertainty in the fit of the Firmani relation and is thus a better estimate. However, to be conservative, we must allow for two-sigma relative uncertainties of a factor of 1.35, 1.5, and 1.67 for estimated redshifts of 5, 7 and 10, respectively, and we do not draw any conclusions for bursts with estimated redshifts beyond 10.

4.3.1 WXM Catalog of Bursts and the Firmani Relation

$T_{0.45}$ Calculation

In deriving the correlations among prompt emission properties of bursts, Firmani et al. (2006c) use 19 bursts, eight of which were *HETE-II* detections. GRB030226 did not trigger on board the spacecraft and so has no time-tagged data available, therefore, we have in common seven bursts for which we can perform our temporal analysis (i.e., the determination of $T_{0.45}$ and its errors). We use these seven overlapping bursts to "cross-calibrate" our measurements with those of Firmani et al. (2006c) by fitting a linear model of the form $T_{0.45}^{Firmani} = \alpha T_{0.45}^{WXM}$, where $T_{0.45}^{Firmani}$ are the values published in Firmani et al. (2006c). The calibration bursts are shown in figure 4-4 along with the $L_{\rm iso}$–$E_{\rm pk}$–$T_{0.45}$ relation.

For these bursts, the peak of the energy spectrum and the peak bolometric flux are from the tables of Sakamoto et al. 2005, so the high-emission time, $T_{0.45}$, is the only difference. The difference in $T_{0.45}$ (see Figure 4-5) is in part attributable to our different methods of calculation, but we also expect that our measured values will be longer than those derived by Firmani et al. (2006c) due to the much higher energy bandpass of FREGATE than WXM, and due to the well-known narrowing of temporal features of GRB emission as $\sim E^{-0.4}$ (Fenimore et al. 1995). The values published in Firmani et al. (2006c) have been multiplied by a factor of $(1+z)^{0.4}$, which we divide out. The fit also requires that we account for variance in the model as well (i.e., 'structural' rather than a 'functional' model) which we do by adding a systematic standard deviation in quadrature to the standard deviation of the model. We fit in linear space and impose the constraint (as per the model above) that the fit include the origin. We find $\alpha = 0.51$ with a confidence region of 0.46 to 0.56. The fit is shown in figure 4-5. Also note that the $T_{0.45}$ of the seven *HETE-II* calibration bursts span most of the range spanned by the global set of 19 bursts of Firmani et al. (2006c). A histogram of these is shown in figure 4-6.

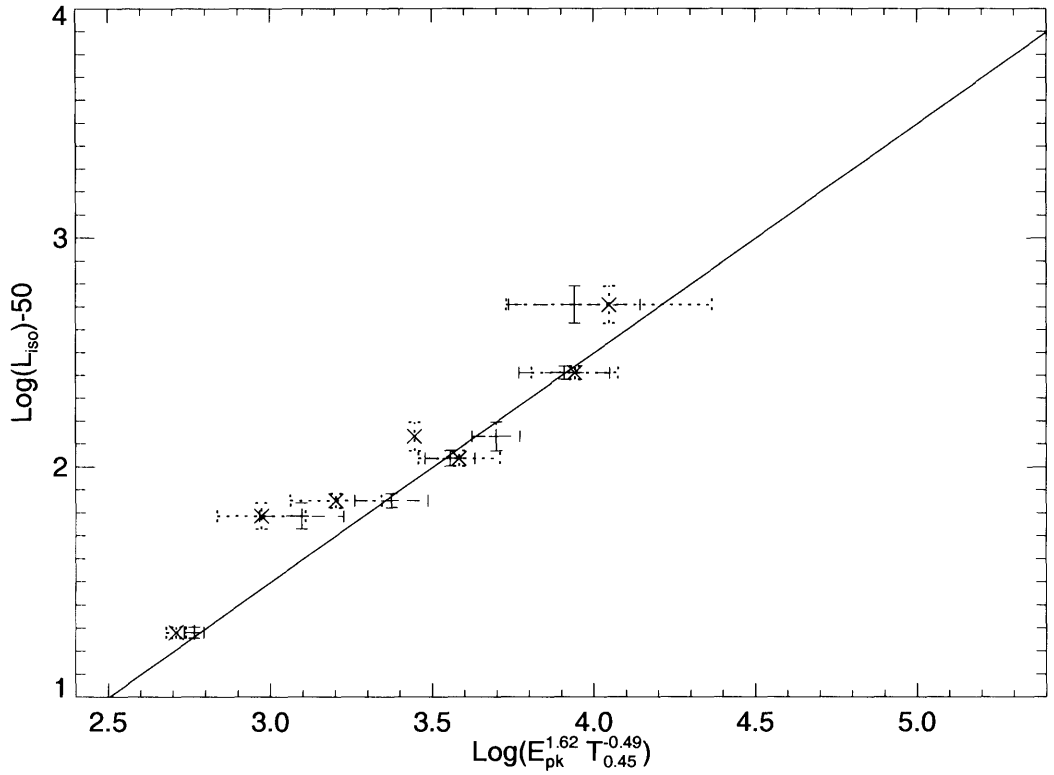

Figure 4-4: The $L_{\rm iso}$–$E_{\rm pk}$–$T_{0.45}$ (Firmani) relation and the seven *HETE-II* GRBs used to calibrate the $\tilde{T}_{0.45}^{\rm WXM}$. The + symbols with solid error bars are the original values by Firmani et al.; × symbols with dashed error bars are the $T_{0.45}$ values from WXM TAG data. The solid line is the $L_{\rm iso}$–$E_{\rm pk}$–$T_{0.45}$ relation of equation 4.1. The ordinates of the corresponding points with dashed and solid errors are the same since only the $T_{0.45}$ parameter is investigated in this step.

$\mathbf{E_{pk}}$ and Peak Flux

We use $E_{\rm pk}$ and peak flux values for WXM bursts as determined by Jernigan (2006). The procedure works for those bursts that were triggered on the spacecraft for which we have WXM TAG and FREGATE event data. For the latter, we compute lightcurves in the 6-400 keV band, and derive maximum count rates per second, the burst foreground ranges and background ranges, usually from the data prior to the burst trigger. From the location of the GRB we determine an appropriate response matrix (RMF) file that serves as a model of the FREGATE instrument for that GRB. We then run XSPEC to determine an approximate spectral fit to the GRB in the form of a cutoff power law.

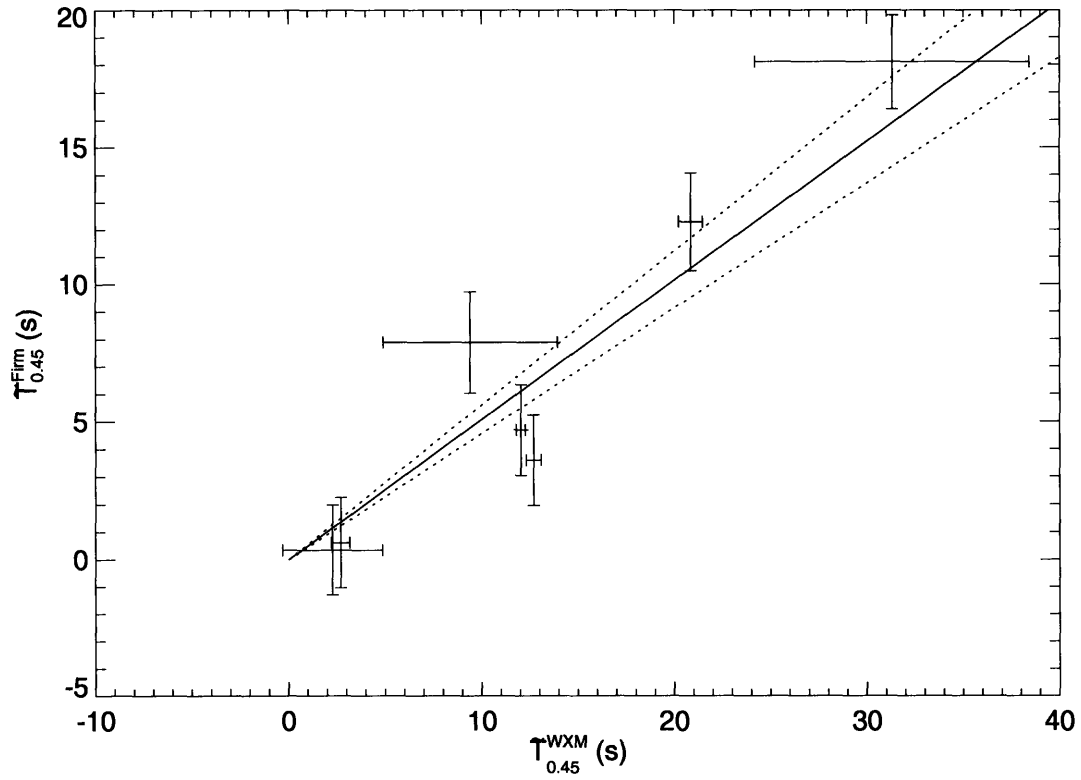

Figure 4-5: Observed $T_{0.45}$ for the seven calibrator bursts. Values published by Firmani et al. (2006c) are along the ordinate and values calculated from WXM TAG data are along the abscissa. The best fit for the one parameter model is the heavy line and the errors are indicated by dashed lines.

From this spectral fit we determine the approximate value of $E_{\rm pk}$, then use XSPEC to calculate bolometric and k-corrections. We first numerically integrate the FREGATE counts in the 6-400 keV band weighted by the instrument model, and then do the same for the total energy in the 1-10^4 keV band for the fitted spectrum without the instrument model. XSPEC can perform this second integral by creating a fake instrument model with a perfect flat response from 1-10^4 keV. The ratio of the second integral to the first measures a bolometric correction factor that determines for each FREGATE count rate the actual flux in the full 1-10^4 keV band. This bolometric correction ratio is multiplied by the peak count rate in the full FREGATE band (6-400 keV) to compute a bolometric energy flux for the GRB. With an assumed cosmology and an estimated redshift this corrected flux can be converted into an $L_{\rm iso}$ for the GRB.

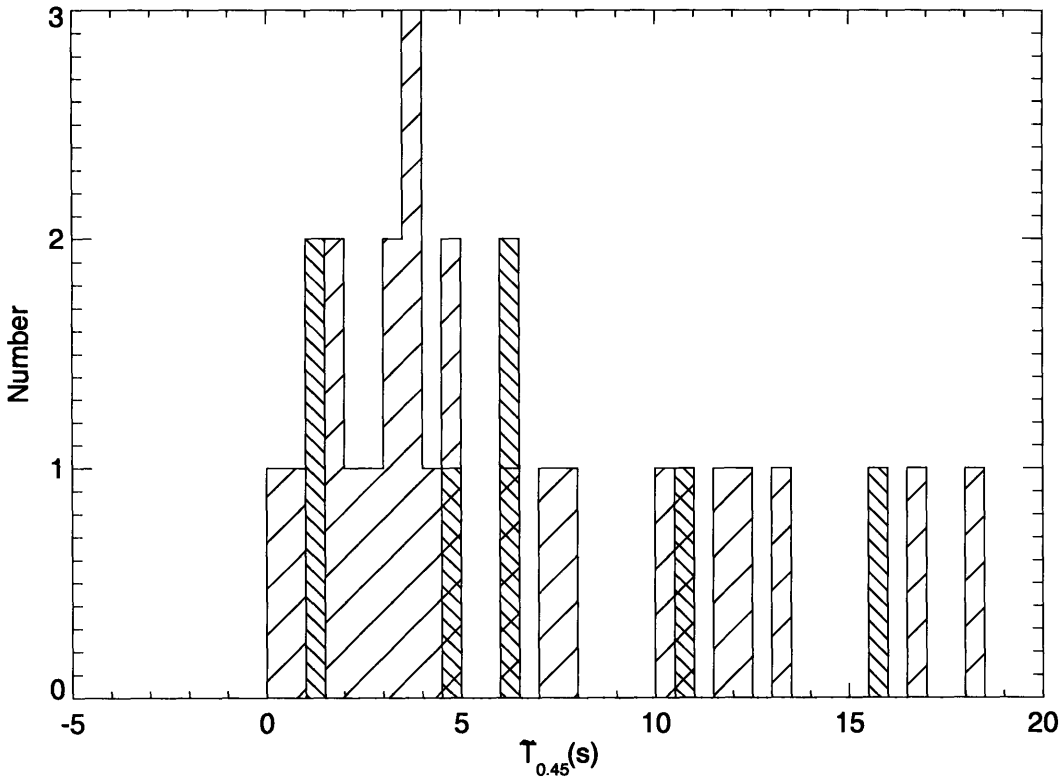

Figure 4-6: Histogram of $T_{0.45}$. Wide hashed are the original 19 of Firmani et al. (2006c) and more densely hashed are the seven from *HETE-II* used to calibrate our catalog. The latter set approximately cover the range of the former.

WXM Catalog of Bursts

The results of the redshift calculations for the WXM bursts and their peak bolometric luminosities are shown in figure 4-7. Also plotted is the flux limit of the survey, 1.5×10^{-7} erg cm^{-2} s^{-1}, which was determined to be the lower flux threshold that includes all bursts in the sample. The calculations use the standard concordance cosmological model, $H_0 = 70$ km s^{-1} Mpc^{-1}, Ω_M=0.3 and Ω_Λ=0.7.

Selection Effects and Completeness

Figure 4-8 shows the results of the analysis of all GRBs detected by *HETE-II* that have measured raw count rates in the FREGATE instrument. By dividing the GRBs into two classes, those that are part of the sample of 31 with estimated redshifts and those not estimated, we can determine if there is any bias in the selection of the

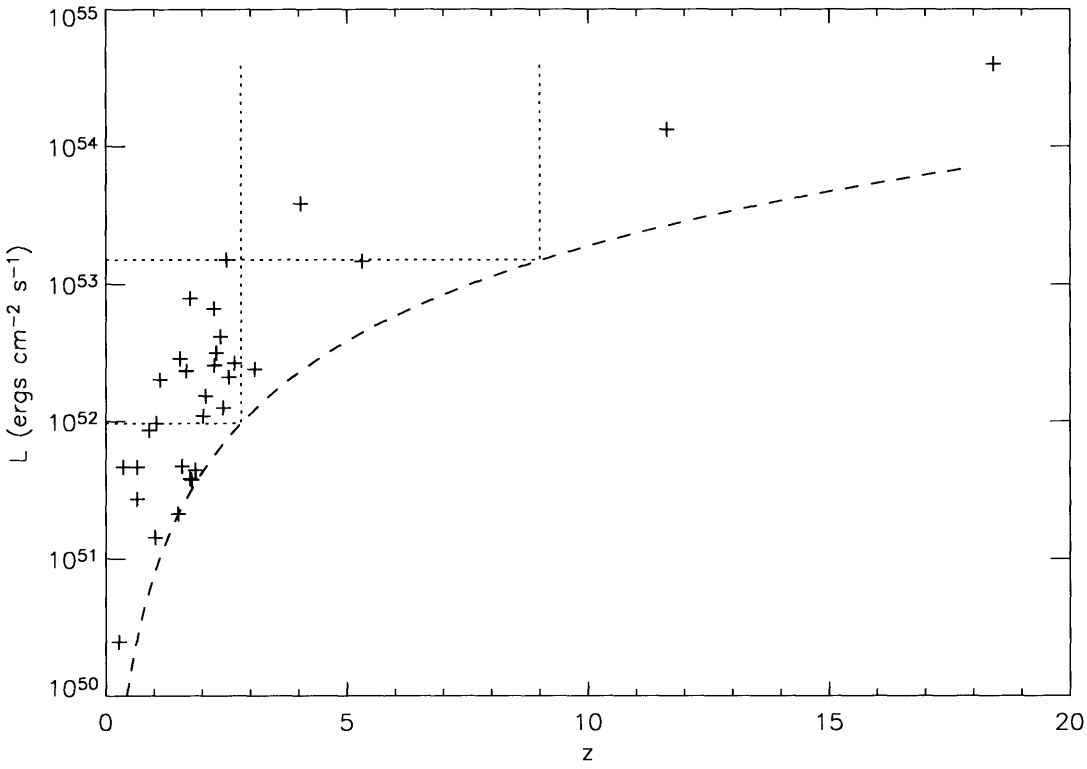

Figure 4-7: Peak isotropic-equivalent luminosity and redshift of WXM-detected bursts. The redshifts are inferred through the Firmani relation. The dashed line represents a flux limit of 1.5×10^{-7} erg cm^{-2} s^{-1} and a ΛCDM cosmology (H_0=70; Ω_M=0.3; Ω_Λ=0.7). The bursts that fall into the upper left quadrants demarcated by the dotted lines are examples of the associated sets defined in equation 4.8.

GRBs used in the analysis of the redshift distribution and luminosity function. We know that the main reasons that only a portion of the GRBs are available for the Firmani estimated z analysis are operational issues (missing telemetry, failed aspect, high background, technical failure to trigger, etc). Figure 4-8 shows that the color distributions of the two classes are consistent with the same underlying distribution if we correctly remove those GRBs that are at high off-axis angles in the FREGATE instrument and are therefore not localized by the smaller field WXM coded aperture instrument. We also know that the performance of the *HETE-II* FREGATE and WXM instruments over time is stable such that we expect the sample of 31 GRBs to be a representative complete flux-limited sample. There is some annual variation in the background rates that might affect the flux limits but the overall GRB detection rate does not vary much as a function of the annual cycle. Since GRB properties are not correlated by the annual cycle, any variation in the flux limit (also see dashed line in figure 4-7) would not affect the measured z distribution and would only modify the luminosity function near threshold. The large dynamic range of GRB luminosities mitigates even this effect.

In summary, we have shown that the sample of 31 is likely to be both without selection bias and complete. The accuracy of the results is limited only by the small sample size but is easily and correctly estimated by bootstrap methods. We have not identified any potential systematic errors at this time. Also, the color-color analysis of the FREGATE data shows a pattern (see figure 1-6(a)) that is likely related to $E_{\rm pk}$, therefore this analysis is appropriate for checking for selection bias in using the $L_{\rm iso}$–$E_{\rm pk}$–$T_{0.45}$ (Firmani) relation, which is the basis of the estimated redshifts.

4.4 Statistical Analysis of the WXM Catalog

We analyze the WXM catalog of bursts to determine the luminosity function and the number distribution of bursts as a function of redshift. We choose to do this with Lynden-Bell's C^- non-parametric method (Lynden-Bell 1971), originally developed for quasars, but applicable generally to data sets with truncation. The method

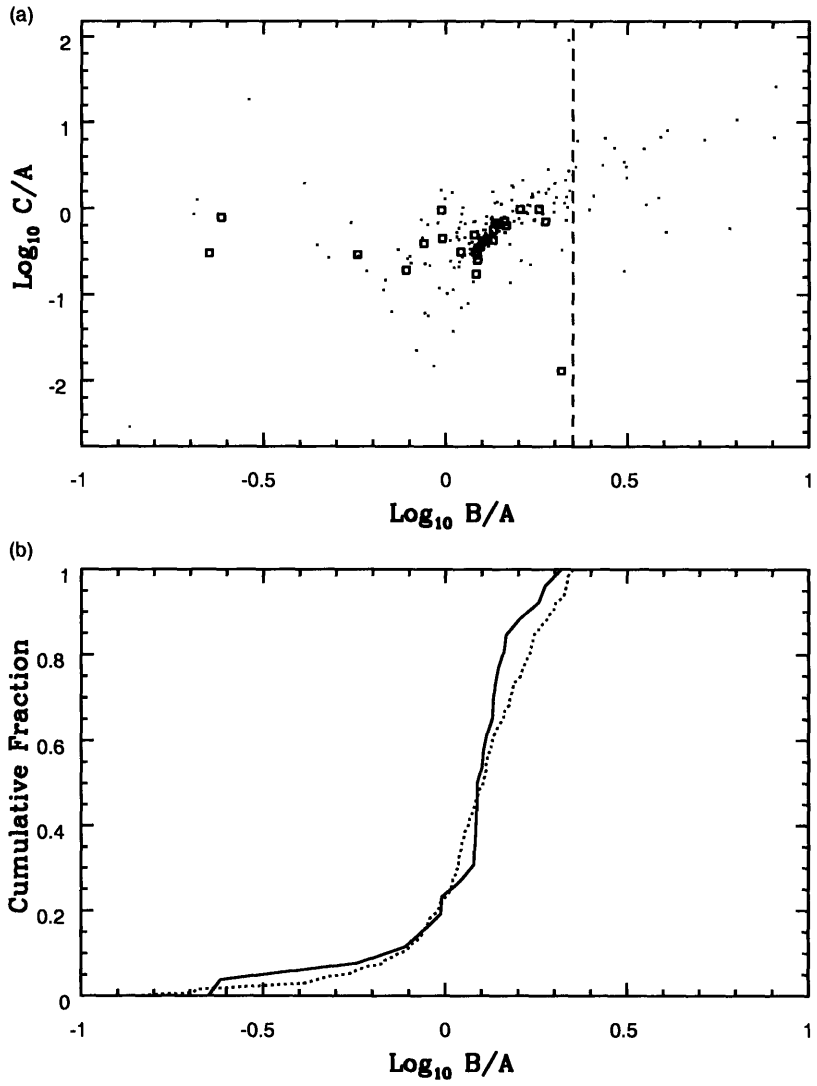

Figure 4-8: Comparison of *HETE-II* GRBs in the sample of 31 that have redshift estimates (squares) and those GRBs without (dots). (a) shows the color-color diagram for all GRBs with measured count rates in the FREGATE A, B and C bands. These bands are in order from low to high energy (also see figure 1-6). The dashed line marks $\log_{10} B/A = 0.35$. The points to the right of this line are GRBs that are far off axis (high incident angle) in the FREGATE instrument where effective area is modified differently in the A, B and C bands due to collimator absorption. The sample of 31 GRBs are detected in both WXM and FREGATE and therefore are all to the left of the dashed line. The dots to the right of the dashed line also show higher values of $\log_{10} C/A$ as expected. (b) shows the cumulative distribution of the B/A ratio for the dots to the left of the dashed line in (a) as a dotted line. The cumulative curve for the sample of 31 (squares in (a)) is the solid line. These two cumulative curves are nearly the same and are consistent with the same underlying distributions according to a K-S test (confidence better than 90%).

has been shown to give luminosity and density functions equivalent to maximum likelihood estimates (Marshall et al. 1983; Choloniewski 1987). We investigate the evolution with redshift of the luminosity function using a closely related rank-order correlation test (Efron & Petrosian 1992) that also applies to truncated data sets. This method has been applied to quasars (Maloney & Petrosian 1999), and gamma-ray bursts (Lloyd-Ronning et al. 2002; Yonetoku et al. 2004; Kocevski & Liang 2006).

Correlations between luminosity and redshift of gamma-ray bursts should not exist unless they are due to an evolving luminosity function or observational selection effects. The aim of the Efron & Petrosian (1992) approach is to eliminate the selection effects and to quantify the evolution. That the flux limit creates an artificial correlation between L and z is well known and the idea is to eliminate this by calculating correlation coefficients only among those bursts that would have been mutually observable. This set is defined as follows: if a burst i was observed, take the set of all bursts that would also have been observed (their luminosity greater than that of i), but limit the set to only those whose observations would in turn imply that i would have been surely observed (their limiting luminosity less than the luminosity of i). This set is often called the "associated set", and is graphically a rectangle in the L-z plane, whose one corner is on the detection limit curve and whose lower edge intersects the burst i. More formally, the set is defined as:

$$J_i \equiv \{j : L_j > L_i, L_{lim,j} < L_i\} \tag{4.8}$$

In this set, we define the rank in redshift, R_i, of burst i as

$$R_i \equiv \left|\{j \in J_i^+ : z_j \geq z_i\}\right| \tag{4.9}$$

where J_i^+ includes the associated set J_i and burst i, and the absolute value signs indicate the number of elements, or cardinality of the set. If there is no correlation between L and z, then R_i will be distributed uniformly between 1 and $N_i = |J_i|$, the number of bursts in the associated set, with expected value $E_i = (N_i + 1)/2$ and variance $V_i = (N_i^2 - 1)/12$. We can now form a correlation statistic similar to

Kendall's tau (a rank-order correlation coefficient) from the rank of each burst:

$$\tau = \frac{\sum_i (R_i - E_i)}{\sqrt{\sum_i V_i}} \tag{4.10}$$

This quantity has zero mean and is normalized to have a standard deviation of one. The significance of the correlation is then given by the value of $|\tau|$.

We can write the bivariate distribution of gamma-ray bursts in luminosity and redshift, $\Psi(L, z)$, explicitly as the separable product of the GRB rate density and the evolving local luminosity function: $\rho(z)\phi(L/g_k(z), \alpha_s)/g_k(z)$, where $\rho(z)$ is the GRB rate density, and α_s parametrizes the shape of the luminosity function. $g_k(z)$ parametrizes the correlation between L and z thereby describing the evolution of the luminosity function with z. Typically, one assumes a functional form $g_k = (1+z)^k$. The evolution of $\phi(L)$ can then be found by letting $L \rightarrow L' \equiv L/g_k(z)$ and varying the parameter k, until $\tau(k)$ is zero. The 1σ error region of the evolution parameter, k, will be determined by the region where $-1 < \tau < 1$.

With the evolutionary effect parametrized, we can proceed with the set (L', z) and calculate the luminosity function and the GRB rate. The Lynden-Bell C-method gives a solution to the cumulative luminosity distribution function, that is, the number of bursts with luminosity greater than a given value:

$$\ln \Phi(L_i) = \sum_{j<i} \ln \left(1 + \frac{1}{N_j}\right) \tag{4.11}$$

(Lynden-Bell 1971; Efron & Petrosian 1992). In eq. 4.11 the L_i are ordered by luminosity ($L_i > L_j \Leftrightarrow i > j$) and the N_j are, as before, the number of bursts in the associated sets. The normalization of the resulting cumulative luminosity distribution is relative. The cumulative distribution in redshift is obtained with the same method, but with the associated sets defined as all bursts with redshift less than that of the given burst and with luminosities above its luminosity limit. In calculating the cumulative redshift distribution with the Lynden-Bell method, the bursts are ordered by their redshifts.

The traditional luminosity function and redshift distribution can be calculated by either taking a numerical derivative of the cumulative, or differentiating an analytic functional form fitted to the data. To find the comoving rate density of GRBs, ρ, we divide the rate per redshift interval, $d\sigma/dz$, by the differential volume at the redshift, and multiply by $(1+z)$ to account for time dilation:

$$\rho(z) = \frac{d\sigma(z)}{dz}(1+z)\left(\frac{dV(z)}{dz}\right)^{-1} \tag{4.12}$$

4.4.1 Accounting for Errors in the Redshift Estimates

Spectroscopic redshifts are sufficiently accurate with normal rather than log-normal errors that a Lynden-Bell analysis is possible in which the errors in z are ignored. The use of an estimator with log-normal errors requires a modified Lynden-Bell approach that has not been addressed in the literature yet.

We have seen that the errors in the Firmani redshift estimator are approximately log-normal with a standard deviation of 0.093 dex. The main manifestation of the errors is that they widen the observed distribution of redshifts compared to the true distribution. This is seen as a scattering of estimated z from the $1 < z < 2$ range into $0 < z < 1$ and the scattering of high $z > 8$ estimates to even higher z. Both these distortions are caused by the convolution of the true redshift distribution with a wide log-normal error distribution. We wish to deconvolve the errors to recover the true redshift distribution.

We oversample the original 31 bursts to adequately represent the error regions of their redshift estimates. (This has the additional advantage that it facilitates taking numerical derivatives of the Lynden-Bell cumulatives in later stages of the analysis.) This oversampling is a Monte-Carlo procedure, *not* a bootstrap, because we have a model of the parent redshift error distribution. For each re-sample, we take the burst redshift and add a deviate to $\log(1+z)$ that is drawn from a normal distribution of zero mean and width 0.093 (i.e., from $\mathcal{N}(0, 0.93)$). We also add a normal deviate to log(L) drawn from a normal of width 0.2 merely to smooth our luminosity function

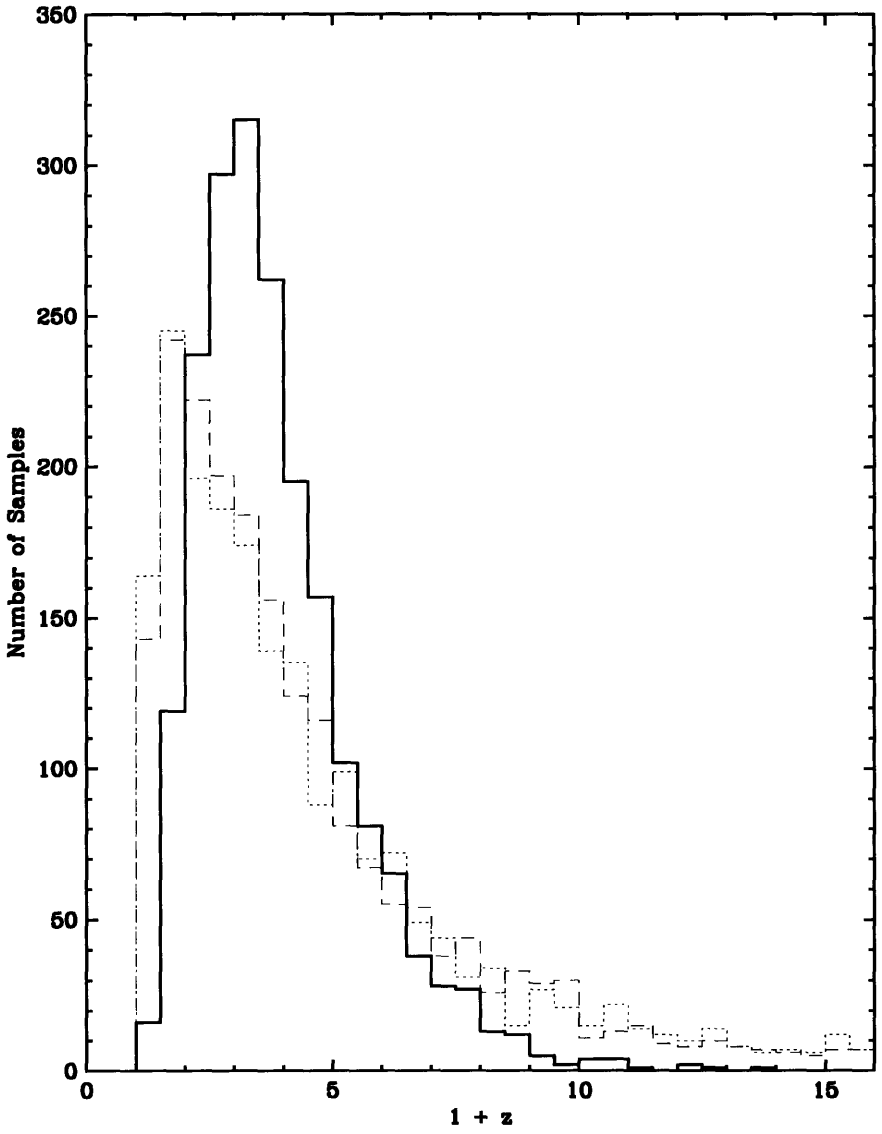

Figure 4-9: Deconvolution of redshift estimates and errors. Plotted are histograms of the roughly 2000 redshifts resampled from the original 31. (Not plotted are the luminosity values, which are also resampled in pair with the redshifts.) The dotted curve is a smoothed version of the measurements (2000 rather than 31 points). The smoothing is due to independent log-normal errors from estimating the redshifts *and* the resampling. This curve has points scattered into low and high z. The solid curve is the estimated true flux-limited z distribution. The solid histogram is convolved twice with the log-normal errors to compute the dashed histogram. Since the dashed histogram approximately matches the dotted histogram with excess low and high points, the solid curve is a correct approximation of the true flux-limited z distribution.

results (with a dynamic range in L of 3 orders of magnitude, this will have little effect on the derived luminosity function). This resampled distribution represents our "measurements" and is shown in figure 4-9 as the dotted line (only the z values are histogrammed). The information content is still just that of the redshifts and luminosities of the original 31 bursts, and size of the error in log(1+z).

But now resampling has actually introduced the measurement error acting twice on the true redshift distribution: once in the original redshift estimation via the Firmani relation, and once in resampling procedure just described. (One can think of a hypothetical set of spectroscopic measurements as the "true" distribution.) To estimate the true distribution, we add a random deviate to log(1+z) that has the tendency to increase z when it is less than one, and decrease it when it is larger than 8, in the process reducing the tails of the distribution. The expected change in each point is less than the 1 sigma error in the redshift estimation. The *ad hoc* function we use is

$$\Delta \log(1+z) \sim \mathcal{N}\left(e^{-z} - \left(1 - e^{(-z/8)^2}\right), \sigma\right) \tag{4.13}$$

where $\sigma = 0.093$.

The result of this transformation is shown as the solid curve in figure 4-9. To prove that this *ad hoc* method works and indeed recovers the correct true z distribution, we apply the log-normal redshift errors *twice* to the distribution shown in the solid curve, getting the dashed line in figure 4-9. This is equivalent to the dotted line we started with under a K-S test. Note that both the large shift of the peak to lower z and the modest excess of z's in the range $z > 10$ has been recovered while shifting the individual z's by less than one sigma on average.

In the final step, the (L,z) pairs represented by the solid curve are cut at the flux-truncation limit of the original 31 bursts, as shown in figure 4-10. The remaining pairs are now intended to model the correct flux-limited distribution of z *without* the effects of the log-normal errors. They form the input to the Lynden-Bell method to deduce the luminosity function and z distribution of GRBs, corrected for flux truncation.

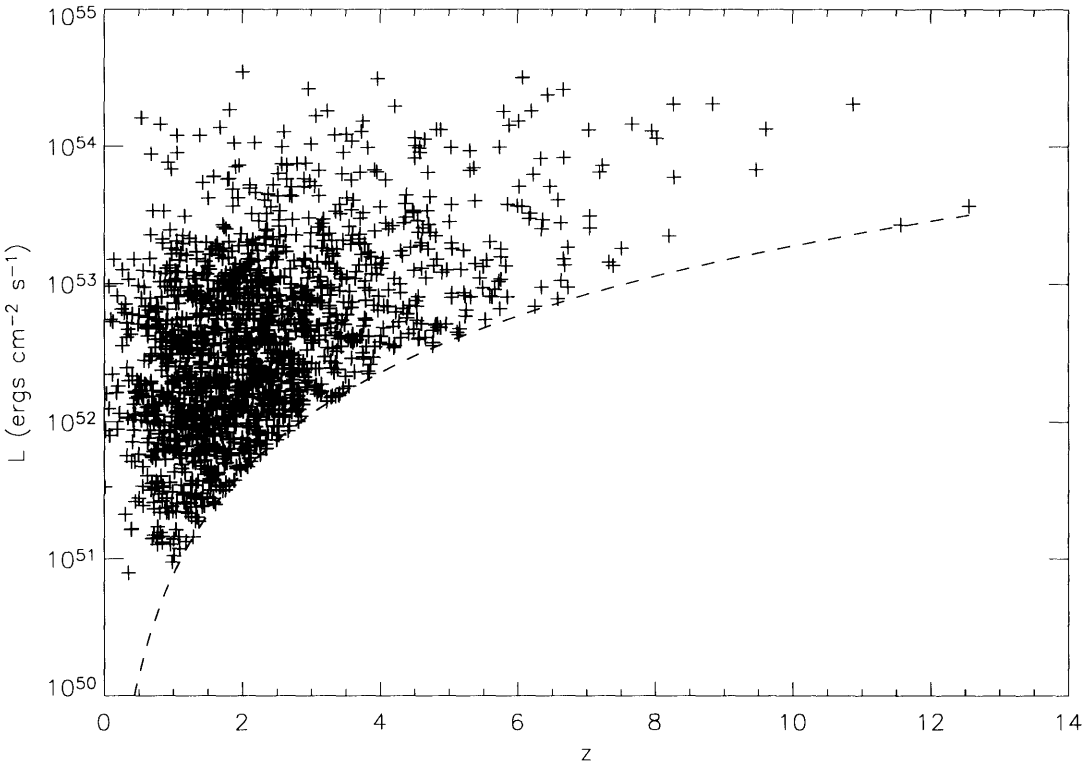

Figure 4-10: The Monte-Carlo resampling of the data in the Luminosity – z plane. The resampling allows for the effects of the large log-normal errors in the redshift estimates.

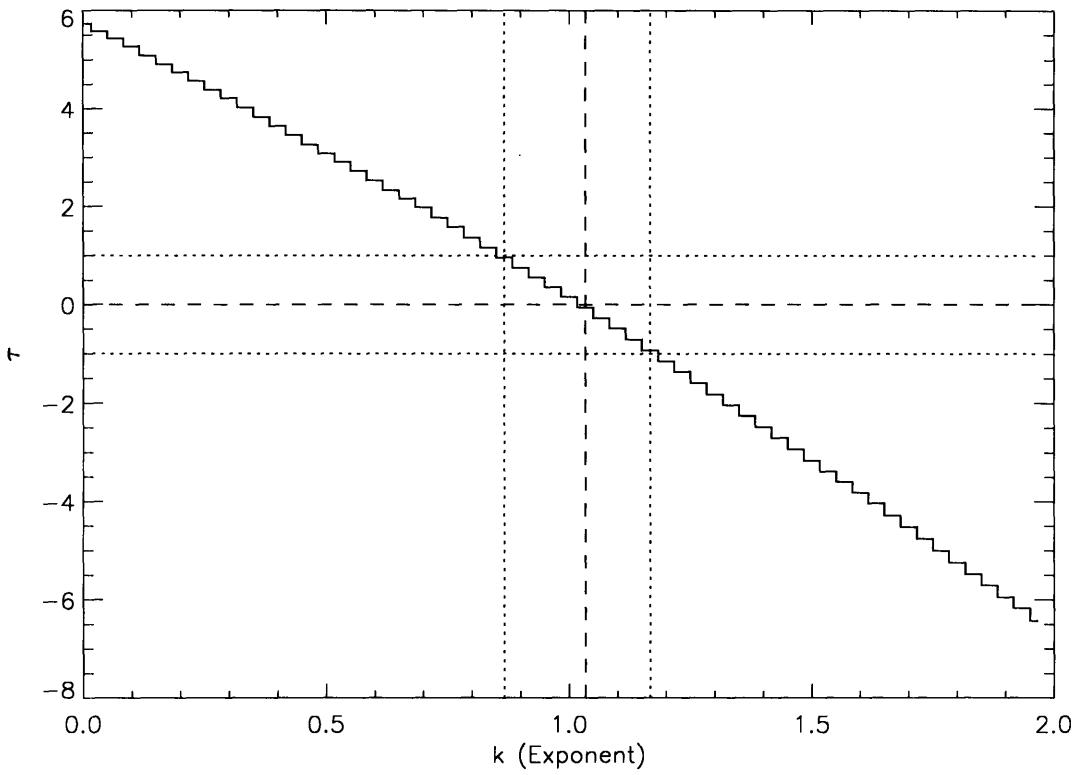

Figure 4-11: The τ coefficient of correlation between redshift and luminosity as a function of the power of $(1+z)$ in the luminosity rescaling $L \rightarrow L/(1+z)^k$. The dotted lines indicate the values that yield the one standard deviation interval and the dashed line indicates the value where the correlation vanishes ($\tau = 0, k = 1.03$).

4.5 Results

Luminosity Evolution

Figure 4-11 shows the correlation as a function of the exponent k of the evolution function, $g_k(z) = (1+z)^k$. The results are confirmed by a bootstrap analysis as shown in figure 4-12. Our data reject the non-evolving luminosity function at a significance of 5.7 σ, with an implied luminosity evolution of $L \propto (1+z)^{1.03^{+0.13}_{-0.16}}$. These results are within the limits of $L \propto (1+z)^{1.4\pm0.5}$ found by Lloyd-Ronning et al. (2002) using a similar analysis of 220 *BATSE* GRBs with the luminosity-variability relationship, and about two standard deviations from $L \propto (1+z)^{1.7\pm0.3}$ found by Kocevski & Liang (2006) who analyzed the 900 GRB *BATSE* set of redshift and luminosities calculated by Band et al. (2004) using the lag-luminosity relationship.

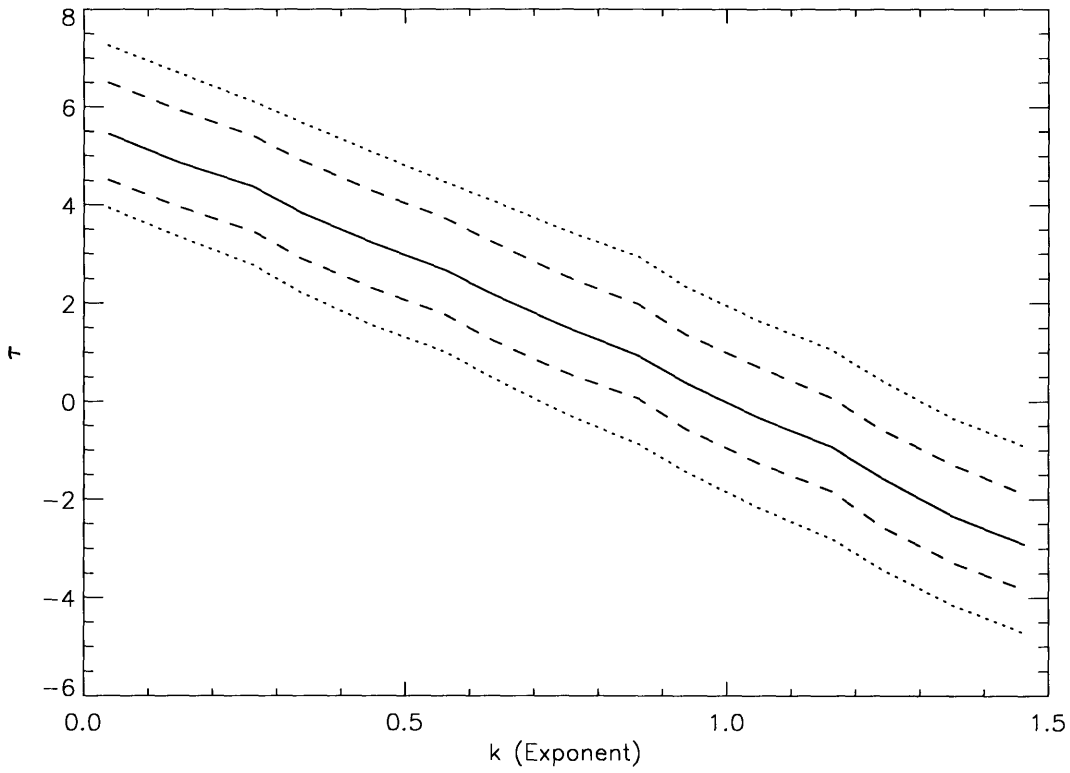

Figure 4-12: Error analysis of the luminosity function evolution parameter. Note that variations in the bootstrapped result at k=0 imply $4 < \tau < 8$, clearly rejecting a model with no evolution ($k = 0$). The solid line is the median of the bootstrap realizations, the dashed lines enclose the 68% confidence region (± 1 standard deviation), and the dotted lines bound the 90% region. Note that the dashed lines are ± 1 in τ, which just confirms that τ is constructed to have unit variance.

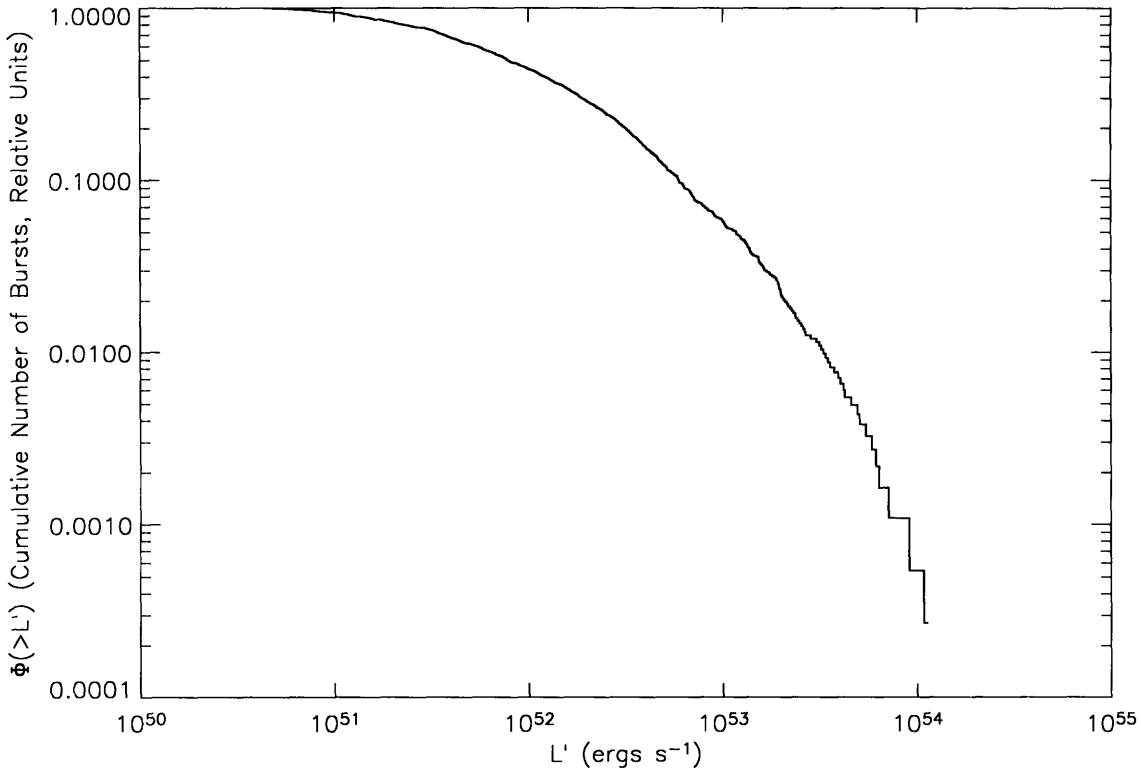

Figure 4-13: The cumulative gamma-ray burst luminosity function (number of objects with luminosity greater than the abscissa) as determined by the non-parametric Lynden-Bell method. The luminosity is the peak, isotropic equivalent luminosity, scaled to remove evolutionary effects. The Lynden-Bell method does not give the normalization, which is separately set to 1.0.

Luminosity function

Figure 4-13 shows the cumulative luminosity function of GRBs, and figure 4-14 shows the differential luminosity function with a dashed line of $L^{-1.52}$ over-plotted. That power-law was found by Donaghy et al. (2003), who performed a maximum likelihood analysis of *BATSE* GRBs using the variability-luminosity indicator and a power-law parametrized luminosity function. Our results are consistent with this behavior, but show a shallower slope at low luminosity and may be better described by a broken power-law. Kocevski & Liang (2006) and Lloyd-Ronning et al. (2002) also find that the differential luminosity power-law index is approximately -1.5 for $L' < 10^{52}$, although their inferred luminosities tend not to range as high as ours.

Our and the aforementioned authors' empirical non-parametric luminosity func-

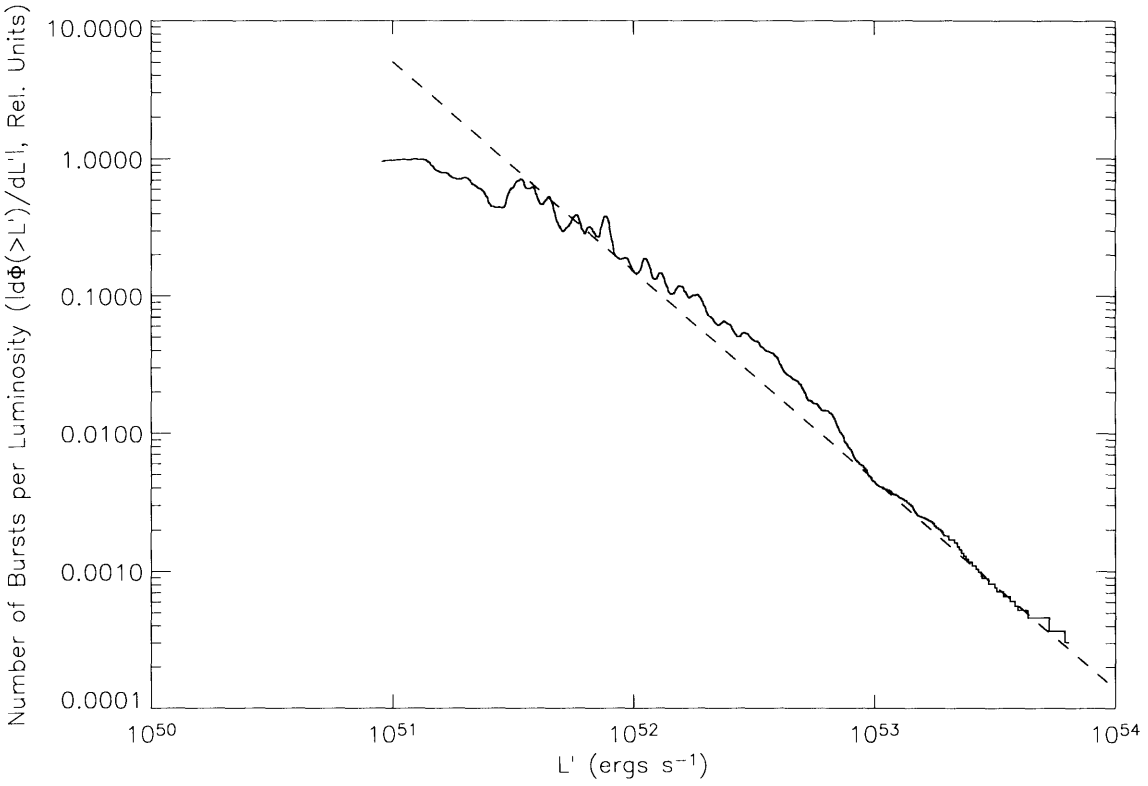

Figure 4-14: GRB luminosity function, derived by numerically differentiating the values of figure 4-13. The differentiation is over a multi-point interval, so successive points are somewhat correlated, in addition to the curve being derived from 31 original points. The dashed line indicates the slope of a power law GRB luminosity function fit found by Donaghy et al. (2003) from a likelihood analysis of *BATSE* data, based the variability-luminosity estimator.

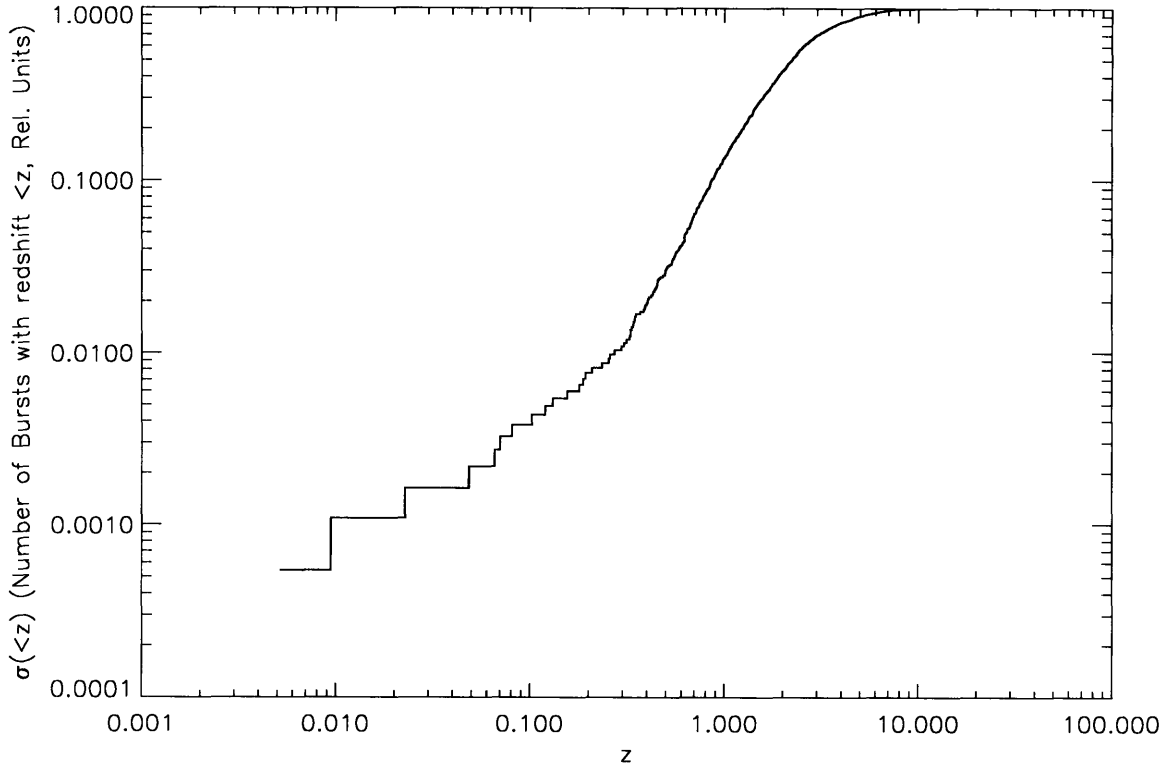

Figure 4-15: Cumulative GRB Rate as a function of redshift as given by the non-parametric Lynden-Bell method. The normalization is set to 1.0.

tions do not show log-normal form, which is assumed throughout Woods & Loeb (1995); Bromm & Loeb (2002, 2006) and by Sethi & Bhargavi (2001).

GRB rate vs. Redshift

Figures 4-15 and 4-16 show the derived cumulative and differential GRB rates, respectively, to within a normalization factor. The differentiation was performed simply with a slope calculation over a multi-point interval. While this introduces correlations in the derivative from point to point, we again point out that a significant amount of smoothing is already present in the 2000 point resampling of the original 31 bursts. Figure 4-17 shows the errors on the calculation that were obtained with bootstrap estimation. The steep drop beyond a redshift of two is statistically significant (see section 6.3). In figure 4-18 we compare the relative-normalized number of GRBs observed as a function of redshift to what is expected from a uniform density in con-

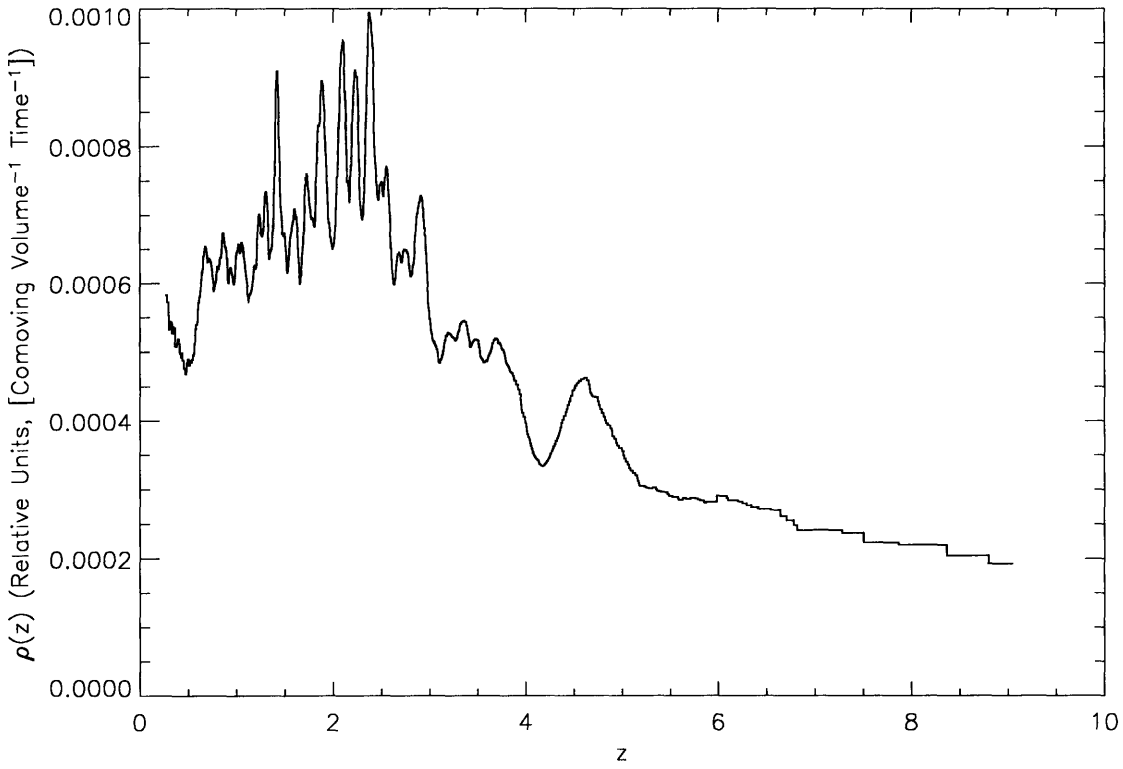

Figure 4-16: Comoving GRB Rate density. Calculated by numerically differentiating the values of figure 4-15 and applying equation 4.12. The differentiation is over a multi-point interval, so successive points are somewhat correlated. The fast variations are due to residual Poisson noise from the set of 2000 (L,z) pairs. The general trend of the curve is a true estimate of the rate density.

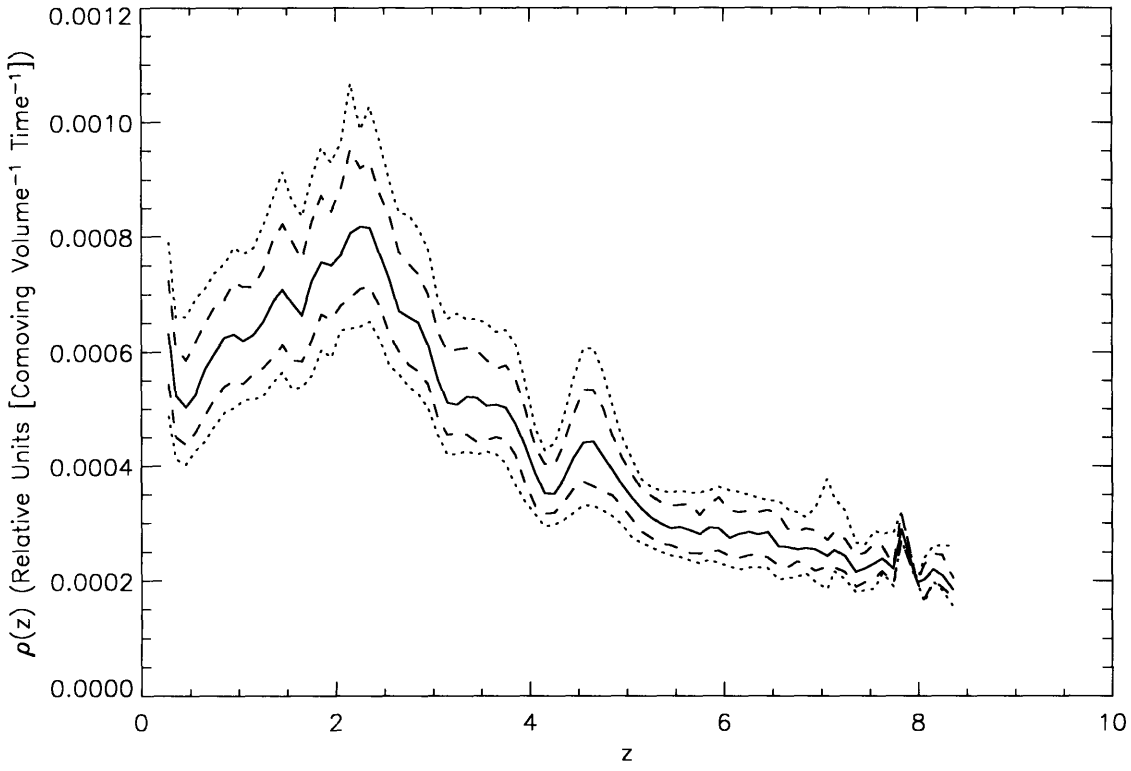

Figure 4-17: Error analysis of the comoving GRB rate density. Calculated by performing bootstrap realizations of the 2000 point Monte-Carlo data set. The solid line is the median of all realizations, the dashed lines enclose the 68% confidence region ($\pm\sigma$), and the dotted lines enclose the 90% regions. The analysis confirms that the fast variations are due to Poisson noise.

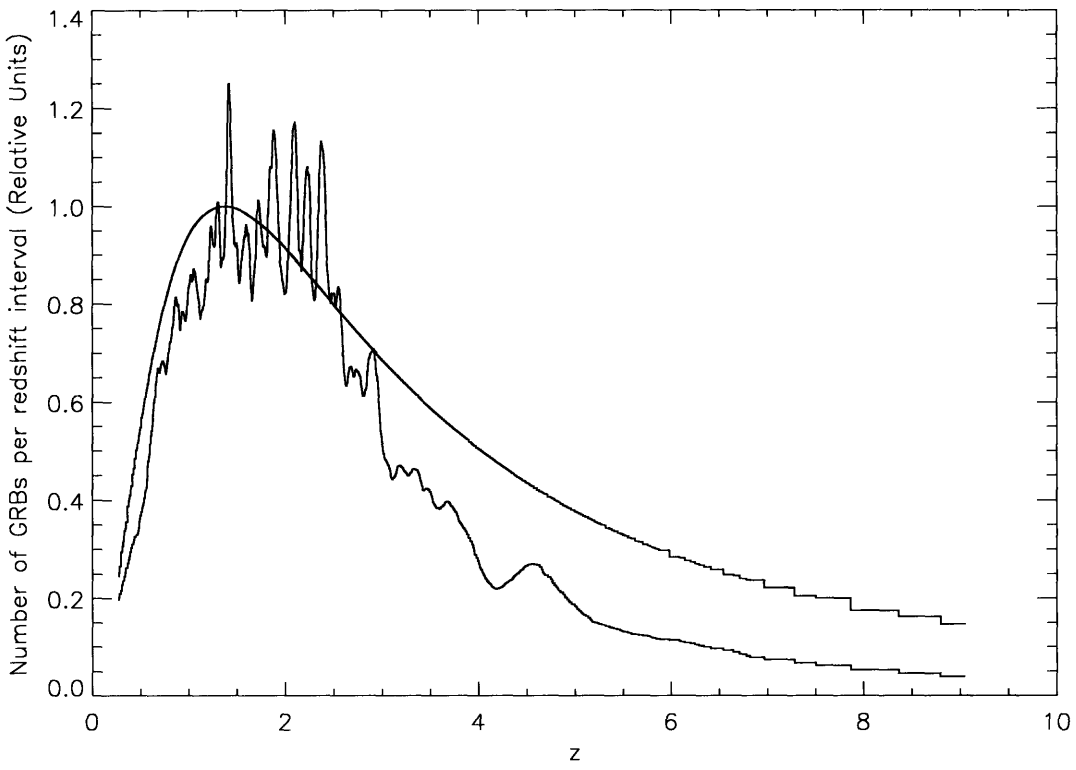

Figure 4-18: Comparison of the *HETE-II* GRB redshift distribution and uniform comoving rate density. The smooth curve is the calculated distribution for a uniform comoving rate density, normalized to its maximum (y-axis scale). Our observed results are over-plotted on a relative scale.

cordance cosmology. The previous figure 4-16 is the ratio of these two. Figure 4-19 shows the raw histogram of redshifts from the Monte-Carlo resampling in comparison to Lynden-Bell C-method rate. Lastly, figure 4-20 shows that the Lynden-Bell method predicts many more intermediate ($2 < z < 6$) redshift bursts than would be expected from simply the 31 in our sample.

The GRB rate curves (figures 4-16 and 4-18) deserve special mention since Lloyd-Ronning et al. (2002) and Yonetoku et al. (2004) found upward trending rates with redshift and only Kocevski & Liang (2006) showed a turnover beyond a redshift of 2, all based on *BATSE* bursts.

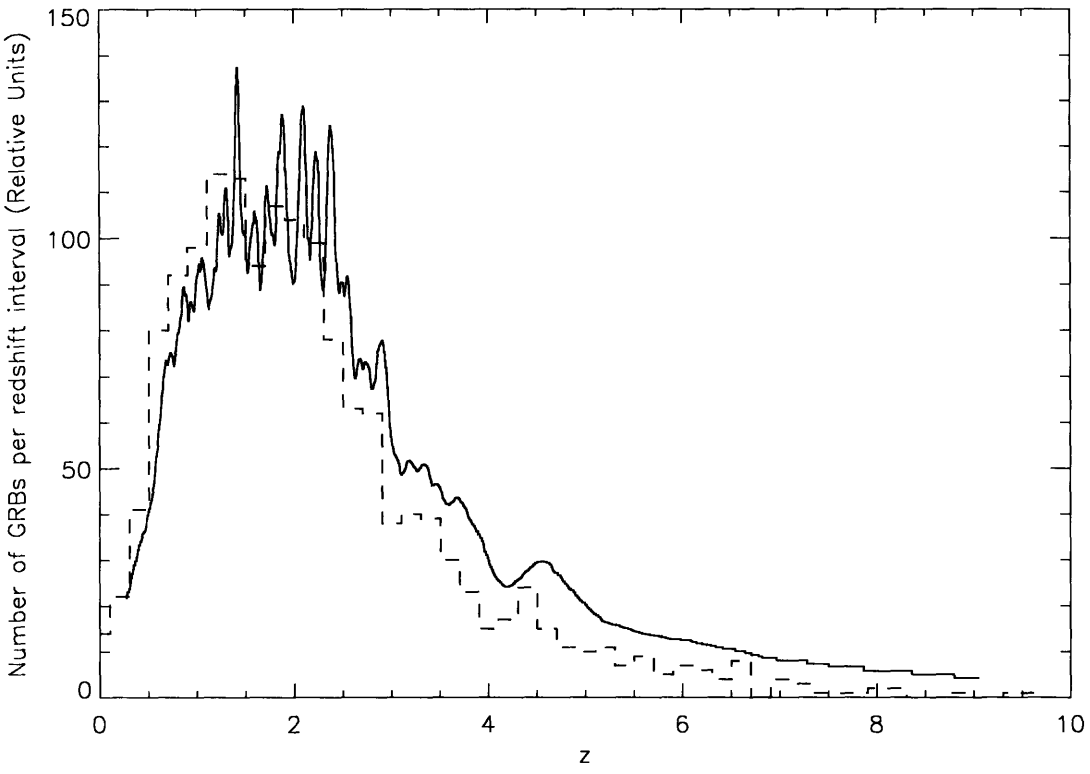

Figure 4-19: Comparison of the uncorrected redshift distribution and the result of the Lynden-Bell method, numerically differentiated. As expected, the agreement is close, but when the differential result of the C^- method is scaled to match the low redshift end of the raw distribution, the high redshift wing shows an excess. Although the differences are small, the effects at high z (> 4) have significant physical implications.

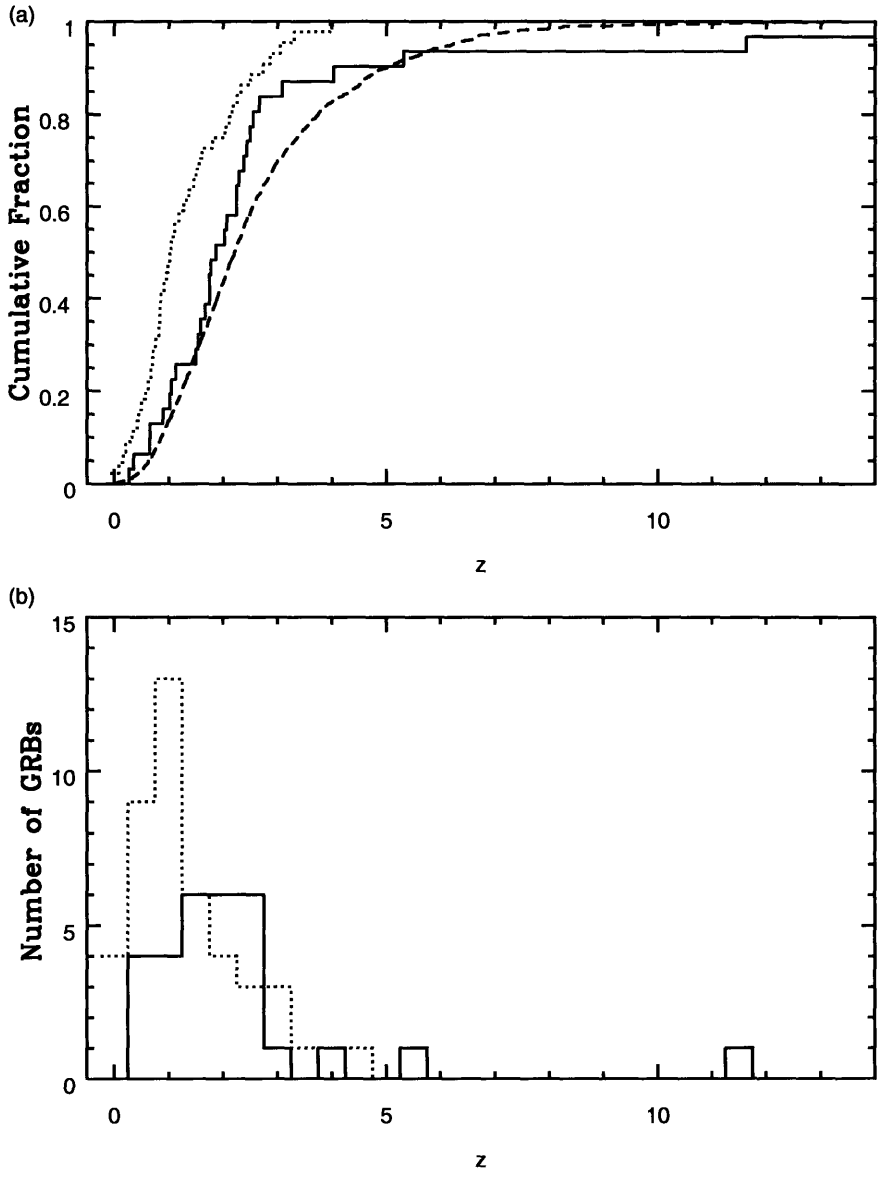

Figure 4-20: Comparison of spectroscopic redshifts and WXM redshift indicators. Panel (a) shows cumulative distributions. The dotted curve is the cumulative of spectroscopic z's from Amati (2006). The solid curve is the raw cumulative of our 31 points. The dashed curve is the Lynden-Bell corrected version. Note that the Lynden-bell matches the solid curve up $z = 2$, deviates lower from $2 < z < 6$, and deviates slightly higher for $z > 6$. Panel (b) curves show the dotted and solid curves as histograms.

Chapter 5

Observed and Intrinsic Duration Distributions

In section 3.6 we described how the parameters T_{90} and $T_{0.45}$ are computed for each individual GRB. The methodology not only determines the median value of T_{90} and $T_{0.45}$ but also their full non-Gaussian error distributions via a bootstrap approach. In this section we discuss properties of the aggregate distribution over all bursts of T_{90}, $T_{0.45}$, and their fractional errors. We summarize the error distribution of individual bursts by calculating the median and the 68% confidence limits centered on the median. These limits would correspond to one sigma limits in cases where the errors are normally distributed, but they are still a useful and valid summary of the error distribution in the general case. The following analysis does not depend on whether or not the Gaussian model is valid in either a linear or logarithmic scale.

5.1 Fractional Error Distributions

We estimate the fractional error of T_{90} by the size of the 68% confidence region divided by the median ($\delta T_{90}/T_{90}$), and similarly for $T_{0.45}$. This approach was first carried out for the T_{90} durations of the *BATSE* catalog (see figure 5-1 from Koshut et al. 1996).

The fractional error distributions of the *BATSE* T_{90} (T_{90}^{B}), the *HETE-II*/WXM T_{90} (T_{90}^{H}) and the *HETE-II*/WXM $T_{0.45}$ ($T_{0.45}^{H}$), all show approximate log-normal

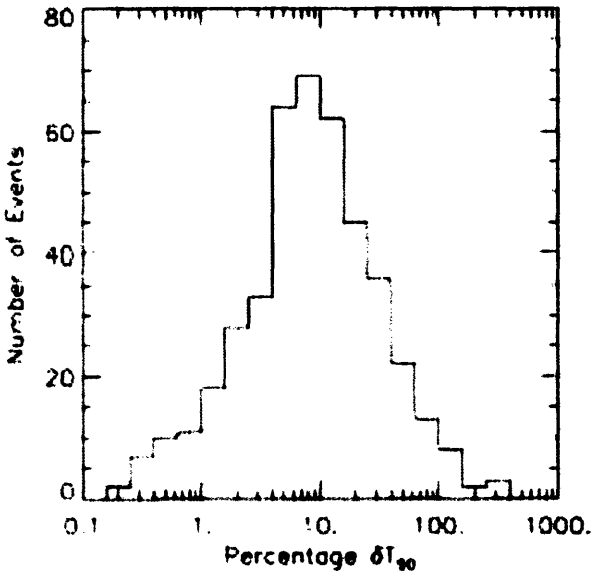

Figure 5-1: Relative error distributions of *BATSE* T_{90}. (Figure 3a from Koshut et al. (1996)).

distributions (figures 5-1, 5-3 panels a and c). The median fractional error for *BATSE* is about 10% ($\log_{10} \delta T_{90}^B/T_{90}^B = -1$). For the WXM, $\log_{10}(\delta T_{0.45}^H/T_{0.45}^H) \simeq -0.30 \pm 0.40$, and $\log_{10}(\delta T_{90}^H/T_{90}^H) \simeq -0.40 \pm 0.35$. The larger median errors for the WXM compared to *BATSE* are due to the lower average signal-to-noise (S/N) for WXM GRBs, since the aperture is much smaller than that of *BATSE*. However, the width of the log-normal distributions of all three fractional errors are nearly the same (about 0.4 dex). Although the median fractional error of the larger aperture instrument is smaller, they both detect many individual GRBs that have T_{90} and $T_{0.45}$ with fractional errors in excess of 100%. An aperture 100 times larger than *BATSE* would be needed to reach a median fractional error of 0.01 (a factor of $\sqrt{100} = 10$ improvement in S/N), an accuracy that would still have one sigma fluctuations of about 10%, if we assume the log-normal form of the fractional error distribution does not change.

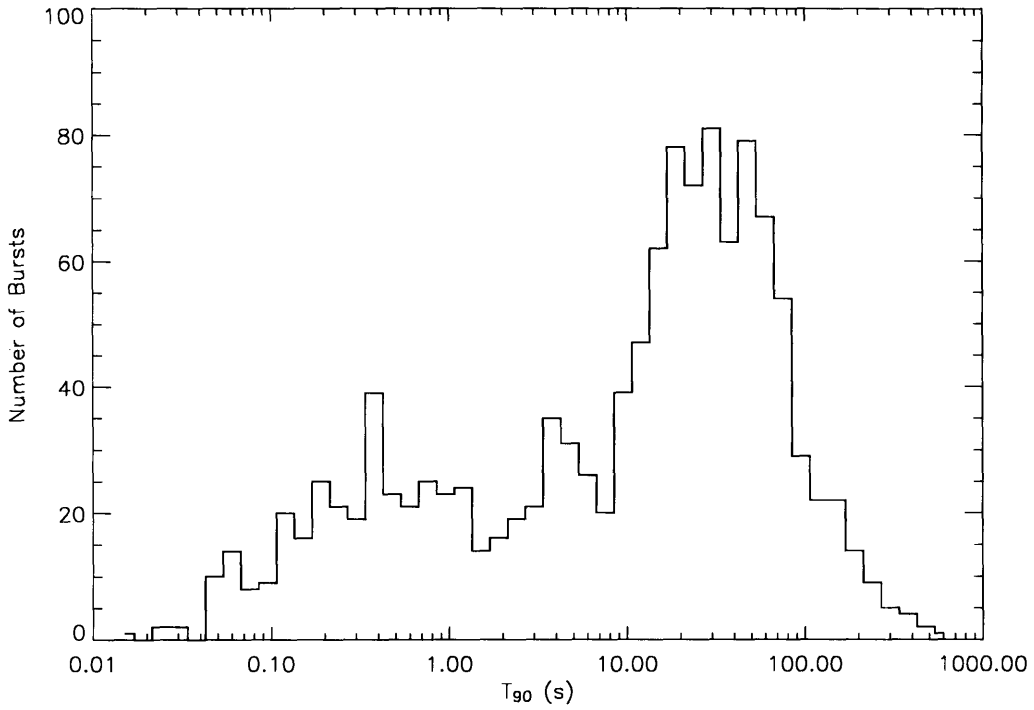

Figure 5-2: Distribution of T_{90} of the *BATSE* 4B catalog.

5.2 Duration Distributions

5.2.1 Intrinsic WXM T_{90} Distribution

With z estimates for the WXM sample of GRBs, we can calculate the histograms of T_{90} and the redshift-corrected (intrinsic) T_{90} as shown in figure 5-4 (a) and (c), respectively. For a comparison with the observed *BATSE* T_{90} distribution see figure 5-2. (In making the comparison we are only addressing the GRBs with $T_{90} > 2s$, i.e., the long GRBs. Short GRBs are not included in the WXM sample of 31.) We do not have estimates of z for the *BATSE* GRBs, so we cannot directly compare the redshift-corrected *BATSE* and WXM distributions. (An independent analysis of the *BATSE* GRBs and the application of the Firmani z estimator is beyond the scope of this thesis.) The redshift correction factor of $(1+z)^{0.6}$ is the product of $(1+z)^{1}$, the time dilation factor, and $(1+z)^{-0.4}$, an energy bandpass related correction factor similar to the one found by Fenimore et al. (1995) for energy-dependent pulse widths, and also used by Firmani et al. (2006c) for $T_{0.45}$. Unlike the situation with energy

spectra where we can rely on the Band model, no good model exists for the instrument bandpass dependence of the T_{90} parameter that would allow a clear correction as a power of $(1+z)$.

We find both the observed and intrinsic *HETE-II* T_{90} distributions are consistent with a log-normal form with better than 90% confidence based on a K-S comparison test. The log-normal form does not depend on the specific values of the exponent of the $(1+z)^k$ correction factor.

5.2.2 T_{90} Fractional Error and T_{90} Distributions

Assuming independence of the errors and the durations, we can write the observed dispersion in T_{90} as the sum (in quadrature) of the width of the error distributions and the intrinsic duration distribution:

$$\sigma^2_{\log T_{90,obs}} = \sigma^2_{\log T_{90,intrinsic}} + \sigma^2_{\log T_{90,error}} \tag{5.1}$$

Figures 5-3(c), 5-4(a) and (c) show that the widths of the T_{90} error distribution, the observed and the redshift-corrected T_{90} distributions are nearly the same. Equation 5.1 then implies that the log-normal wings (right and left) of the T_{90} distributions are consistent with being due to the errors of measurement, and are therefore not necessarily related to any physical properties of GRBs as suggested by several authors (McBreen et al. 1994, 2001; Ioka & Nakamura 2002).

The log-normal errors for the *BATSE* T_{90} distribution also shows a width comparable to that of the observed T_{90} distribution, according to the published report on the analysis methods of the *BATSE* catalog (figure 5-1 and Koshut et al. (1996)). As stated above, the *HETE-II* data confirm this result and we report for the first time the likely conclusion that the wings of the T_{90} distribution are a measurement artifact.

Quantitatively, any residual log-normal distribution that is a true physical property of GRBs likely has a standard deviation $\sigma_{\log T_{90,intrinsic}} \leq 0.3\sigma_{\log T_{90,obs}}$. This estimated upper limit is based on a K-S test for a model that convolves a true GRB

related log-normal with the measured log-normal relative error distribution. The data then are consistent with a physical T_{90} log-normal variance of zero, or more realistically, the functional form has small variance. The functional form need not have a logarithmic argument and could even be a Gaussian or exponential in T_{90}. The small sample of 31 GRBs from the WXM data archive is not sufficient to quantify these possibilities other than to reject the notion that the full log-normal effect is an intrinsic GRB property.

5.2.3 Intrinsic $T_{0.45}$ Distribution

Figure 5-5 shows a similar type of analysis of the distribution of the $T_{0.45}$ parameter as what was just discussed for the T_{90} parameter shown in figure 5-4. Here the results are quite different. The observed $T_{0.45}$ distribution (figure 5-5(a) and (b)) shows extension in the logarithm of the parameter. However, the distribution is not consistent with a log-normal distribution. Note the lack of a Gaussian wing beyond a $T_{0.45}$ greater than 15 seconds ($\log T_{0.45} > 1.4$). To show this more clearly in the cumulative curve the reflection of the distribution about the median in both the abscissa and ordinate is plotted as a dashed curve. The curve and its reflection differ in K-S value by 0.2, which is rejected at the 90% confidence level as due to a chance sampling error. This means that the symmetric form of a log-normal is not present.

More importantly, the redshift-corrected $T_{0.45}$ distribution (figure 5-5(c) and (d)) is not consistent with a log-normal distribution and is in fact a good match to an exponential distribution with a mean of 6 ± 1 seconds on a linear (not log) scale. This basic result does not depend strongly on the choice of the power of $(1+z)$ shown in figure 5-5(c) and (d). For example replacing the $(1+z)^{0.6}$ with $(1+z)^{1}$ which would be true for pure time dilation effect, would still show an exponential distribution in the linear abscissa with a mean of 5 seconds instead of 6 seconds. Although an exponential distribution has standard deviation of order the mean, this shows a duration measure of GRBs that is much tighter than a log-normal distribution. We do not have a clear physical interpretation of the $T_{0.45}$ parameter, but it seems to quantify the duration of a GRB better than T_{90}, hence the success of the $T_{0.45}$ based Firmani z estimator.

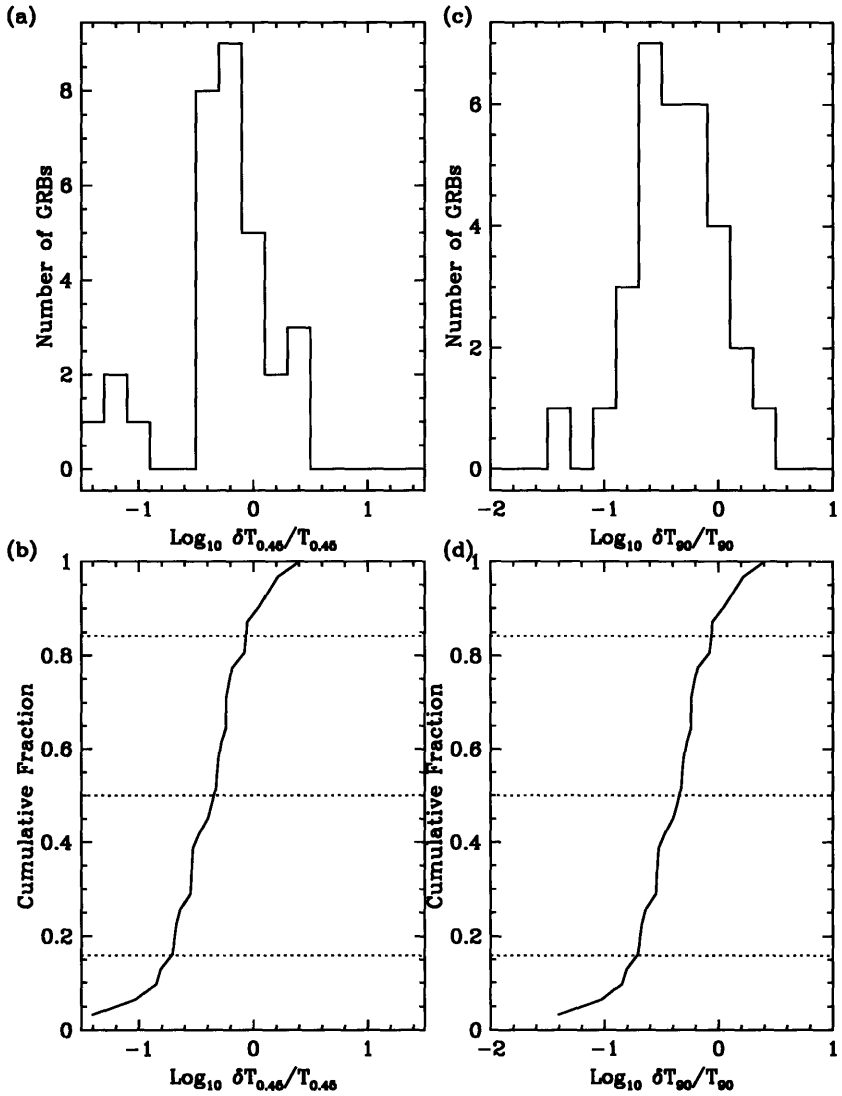

Figure 5-3: Summary of relative error distributions of $T_{0.45}$ and T_{90}. (a) The histogram of the logarithms of the differences in the 68% confidence limits of $T_{0.45}$ divided by the median value of $T_{0.45}$. The histogram is binned in dex 0.2 size bins for visualization. These errors show approximate Gaussian nature in the logarithm of the fractional $T_{0.45}$ error. The mean error is slightly less than unity. The right hand side of the distribution indicates that for some significant fraction of the $T_{0.45}$ the errors exceed 100% (10^0). (b) The cumulative curve of the same data shown in (a) with the same abscissa scale. The dotted lines cross the solid curve at the minus one sigma, median and plus one sigma levels. The curve is consistent with a Gaussian (31 points) at better than 90% confidence determined by a K-S comparison. (c) The same as (a) except for the relative errors of T_{90}. (d) The same as (b) except for the cumulative error distribution of T_{90}. The mean relative error for T_{90} is also slightly less than unity. Also a significant number of T_{90} errors exceed 100% as occurred for the $T_{0.45}$. Both $T_{0.45}$ and T_{90} relative errors are best characterized by log-normal distributions.

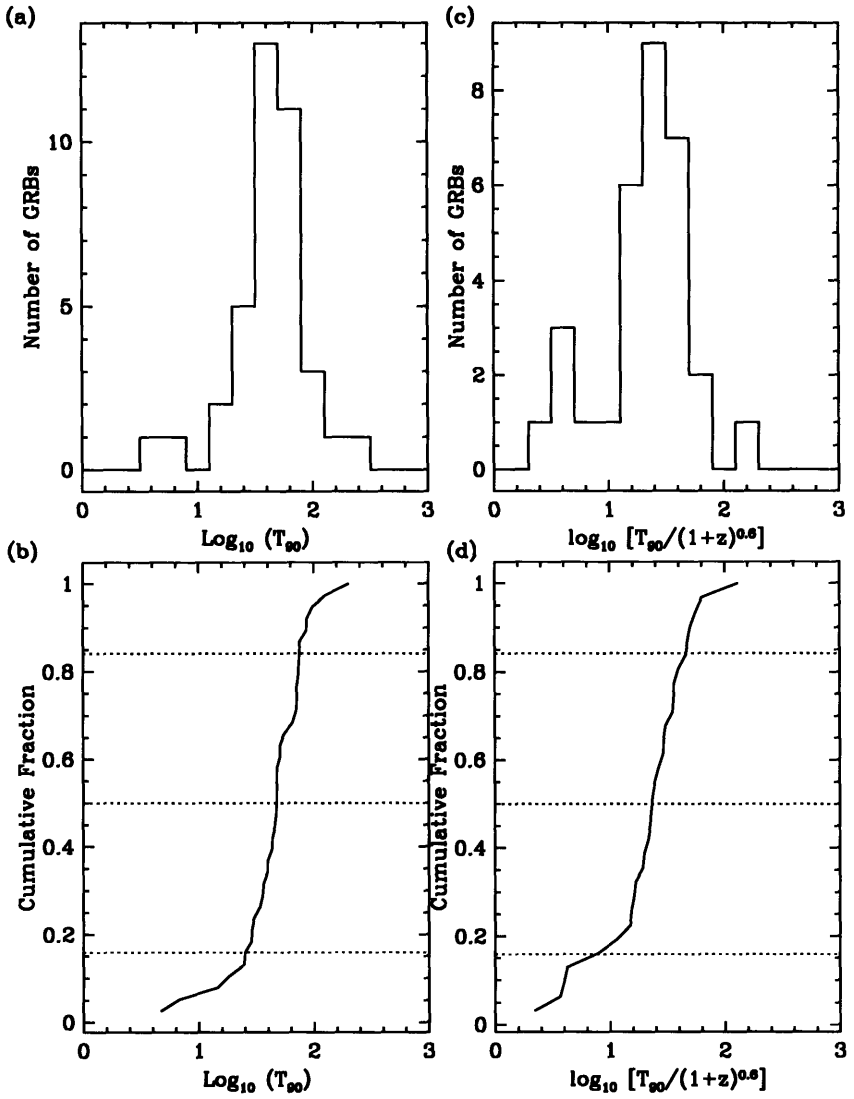

Figure 5-4: Histograms of observed (a) T_{90} and (c) redshift-corrected T_{90}. There are 7 bursts for which we have T_{90} but not z', thus there are 38 bursts in (a). The abscissa units are in seconds. The range of the abscissa shows three decades for easy comparison with figure 5-3. The cumulative distributions are shown in panels (b) and (d). Both of these distributions are approximately log-normal. The plus and minus one sigma and median level is shown by the dotted horizontal lines in (b) and (d). The T_{90} log-normal Gaussian has a mean of 1.65 and a variance of ± 0.23. The intrinsic or redshift-corrected T_{90} log-normal Gaussian has a mean of 1.40 and variance of ± 0.39. The redshift correction factor of $(1+z)^{0.6}$ is the product of $(1+z)^{1}$ and $(1+z)^{-0.4}$, the time dilation factor and a likely k-correction factor similar to the one cited by Fenimore et al. (1995) for energy dependent pulse width and Firmani et al. (2006c) for $T_{0.45}$. The cumulative curves in (b) and (d) are consistent with Gaussians with better than 90% confidence according to a K-S test. Note that for 31 points and K-S difference of 0.2 has less than a 10% chance of occurring due to Poisson sampling variations.

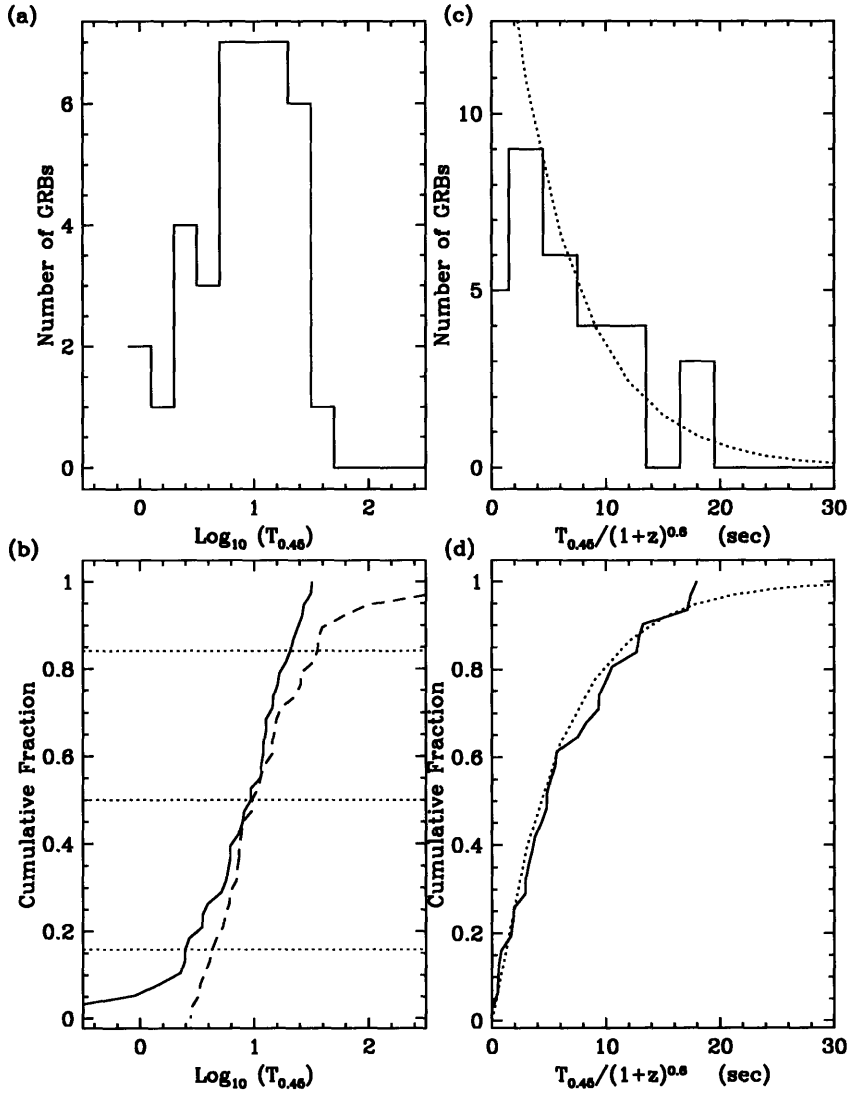

Figure 5-5: Histograms and cumulative curves for $T_{0.45}$ similar to figure 5-4 for T_{90}. (a) Histogram of $\log_{10}(T_{0.45})$. There are 7 bursts with $T_{0.45}$ but no z', so there are 38 bursts in panel (a). (b) the cumulative distribution of the data in (a) with the plus and minus one sigma and median levels shown. Also shown is the reflection of the model about the mean. The maximum K-S difference 0.2 at the high end of the curve shows that this log-normal model is very near the 90% confidence limit for 31 points. The 68% confidence limit at a K-S value of 0.12 is clearly ruled out. This distribution has substantial extension in the logarithm of $T_{0.45}$ but does not fit a log-normal shape very well. The sharp drop at $\log(T_{0.45}) = 1.6$ (or 20 seconds) does not match a Gaussian tail. This indicates that the $T_{0.45}$ parameter does not suffer from large errors at high values to the extent of the T_{90} parameter. Panel (c) shows the intrinsic (redshift- corrected) distribution of $T_{0.45}$. This is well described by an exponential, as shown by the dotted line. Panel (c) shows the cumulative of the data and the exponential, indicating very good agreement and small K-S D statistic.

Chapter 6

Conclusions

In Chapters 1 through 3 we presented technical aspects of our work, and in Chapters 4 and 5.2.3 we applied these ideas to *HETE-II* data to determine intrinsic distribution properties of gamma-ray bursts. In this chapter we conclude by discussing further our results in relation to high redshift GRBs, the GRB luminosity function, and its evolution. We discuss the connection of our work to cosmology and star formation rates and conclude with a view toward future experiments and a final summary.

6.1 High Redshift Bursts

In interpreting the redshift estimates, and in particular two of our highest values of z' of 18.4 and 11.6, it is important to note the distinctions between estimated redshifts and spectroscopic redshifts. Spectroscopic redshifts are often quoted with one standard deviation errors of 0.01 or better and are assumed to be normally distributed. Redshift estimates, on the other hand, are modeled to have log-normal errors. Indeed, we find that the error in $\log_{10}(1+z')$ in comparison to spectroscopic redshifts is approximately normal, with standard deviation 0.093 ± 0.031 (section 4.3). Consider what this means for a burst with an estimated redshift of $\sim$11: its two-sigma confidence region extends from $\sim$5.8 to $\sim$20. Li (2006) points out that the errors of the redshifts inferred from the Amati relation are even more severe. Hence the need for more accurate luminosity indicators. We also note that photometric redshift errors,

while larger than those of spectroscopic redshifts, are nevertheless normal and still much smaller than redshift estimator errors.

It is also important to note that the log-normal error of 0.093 was found for the Firmani relation in the spectroscopically available range of z up to 3.2. In section 4.3 we showed that the uncertainty in the Firmani relation itself will be comparable in magnitude, and much larger at redshifts higher than 10. In these regimes not only might the scatter increase, but the validity of the Firmani relation itself can come into question. Thus we have to assume that we have unmodeled and likely large systematic errors at high z'. Yonetoku et al. (2004) also realized this in connection with the Amati redshift estimator, and in their analysis truncated their dataset at a redshift estimate of 12. It is quite possible that the redshift range in excess of 10 might not be spectroscopically investigated for some time yet. This requires spectrographs that operate at very long wavelengths and time on the largest of telescopes. Consequently, it will be difficult to establish the errors of the Firmani relation at such high redshifts.

We may also look at the errors on the quantities in equation 4.5, namely those of $T_{0.45}$, P, and $E_{\rm pk}$. We believe that errors on the peak flux will dominate due to the large bolometric correction (extrapolating the flux from the observed band of 30-400 keV to 1-10^4 keV). It is also difficult to determine E_0 (and $E_{\rm pk}$) for bursts that have high values ($>$ 400 keV) for these parameters, and overestimating $E_{\rm pk}$ would imply higher redshift estimates. However, bursts with ill-determined E_0 have been excluded from our sample, and we do not find that the high z' bursts also necessarily have high $E_{\rm pk}$. Neither propagating the errors in equation 4.5, nor accounting for the uncertainty in the fitted exponents of equation 4.2 will capture all sources of errors, and presently we believe that the best way to characterize their distribution is as we have done, by looking at the deviation of the estimates from known spectroscopic redshifts.

Given the large confidence regions, we view the redshift estimates as a statistical ensemble and realize that there might be outliers. (Even in sets of spectroscopic redshifts there are outliers, since large errors could be due to misidentification of emission or absorption lines or misidentification of the GRB host galaxy for which

the lines are measured.) By their nature as outliers, these bursts are likely to have their redshifts estimated at the extremes of their error ranges, and so for the very high z' samples, the true values are probably lower. Nevertheless, looking at the set statistically, we can ask what the probability is of having detected a burst with a redshift larger than a given value, say 5. Inspection of the cumulative of burst counts with respect to redshift (figure 6-3) shows that on aggregate, there are about 10% that are above 5, which is approximately 3 bursts for a sample of 31. If we assume that the cumulative of the tail of the distribution is Poisson distributed with mean of 3, that gives a probability of zero events at $z > 5$ of 5%. Thus we have shown that $\sim$10% of all gamma-ray bursts should be from $z > 5$, and that the Firmani relation is still sufficiently functional to allow us to probe this essentially unexplored region of the universe.

6.2 Luminosity Evolution

The strong evidence that we found for an evolving isotropic equivalent luminosity function is not inconsistent with the "standard energy reservoir" of Frail et al. (2001) and Bloom et al. (2003). First, we note that the standard energy is the integrated luminosity after correcting for (model-dependent) jet collimation angles and for the burst durations, therefore the comparison is not quite valid. Also, most of the bursts in these studies occurred in a redshift range of 1 to 3, where an evolution of the form $\propto (1+z)^{-1}$ would result in changes in average properties on the order of a factor of 2. This is less than the reported scatter of the "standard" E_γ. A more constraining finding by Kocevski & Liang (2006) is that E_γ is uncorrelated with redshift, although this is a formal result that is not unexpected given the large scatter, narrow redshift interval, and 25 data points. Furthermore, since we are comparing an evolutionary change of distribution properties to a set of individual measurements, any inconsistency would be tenuous.

Nevertheless, if the gamma-ray burst energy is approximately constant with redshift, but the luminosity function is evolving, that is an indication that the burst

durations, jet opening angles, or jet structures are evolving in such a manner that higher redshift bursts appear to be more luminous. Evolution of burst properties is physically plausible since there is evidence of evolving metallicity and initial stellar mass function in the universe. Theoretical models could explain how larger mass progenitors, or ones with higher angular momentum or higher mass loss rate, can produce more luminous bursts (MacFadyen & Woosley 1999).

A uniform jet model assumes that the energy emitted per solid angle, $\epsilon(\theta)$, is uniform across the jet, and the various achromatic afterglow lightcurve break times are mostly due to different jet angles. In this simple model the higher luminosities would imply narrower jet angles, yet the same data that show no evidence for correlation between E_γ and z also show no correlation between the inferred jet opening angle (θ_{jet}) and z (Kocevski & Liang 2006). Other jet structures, such as Gaussian ($\epsilon(\theta) \propto \mathcal{N}(\theta; 0, \sigma_\theta)$) and power-law ($\epsilon(\theta) \propto \theta_j^{-k}$), are also able to account for observed breaks in the afterglow lightcurves as a function of viewing angle (θ_v), and have additional degrees of freedom that could account for evolution, such as a power-law index that is a function of redshift

The more complex jet profiles can also lead to predictions about the shape of the luminosity function. Power-law jets predict luminosity functions with a slope of $-(1 + 2/k)$ (Zhang & Mészáros 2002) while Gaussian jets predict a slope of -1 (Lloyd-Ronning et al. 2004). If we assume a power-law form, our results of chapter 4 (which showed consistency with the luminosity function of the form $d\Phi(> L')/dL' \propto L'^{-1.5}$), imply that $k = 4$, or $\epsilon(\theta) \propto \theta_j^{-4}$. It is clear we need more bursts to better quantitatively determine the luminosity function and its evolution before being able to strongly discriminate between GRB jet models. Importantly, more bursts would also let us investigate of the evolution of the *shape* of the luminosity function by splitting the data into redshift intervals.

6.3 Cosmology

Cosmological parameters and the Hubble diagram

Studies of the expansion history of the Universe and the possibility of the existence of a medium with negative pressure (repulsion), often called "dark energy", are performed by Hubble diagram studies. These diagrams plot an independent measure of distance (e.g., luminosity distance) against the spectroscopically determined redshifts of objects. In the simplest form of the procedure, the objects must be "standard candles", that is, of known luminosity, for the luminosity distance to be a truly independent measure of distance. One can than vary the cosmological parameters until a best fit to the data is found.

The procedure is more complicated when the objects plotted are not perfect, idealized standard candles, as in the case of supernovae Ia (SNe Ia). The solution is to "standardize" the candles, i.e., to find some other distinguishing factor that can be used to infer the true luminosity of the objects, such as the decay rate of the lightcurve, then calibrate this effect with nearby supernovae where the cosmology does not affect the measurements. With standardized supernovae Ia, Riess et al. (1998) and Perlmutter et al. (1999) demonstrated that the expansion of the Universe is accelerating. SNe Ia occur in the local universe in large numbers but their observability is limited to about $z \leq 1.7$.

The situation is reversed with gamma-ray bursts: they are observable in the prompt emission to high redshifts (currently the highest spectroscopic redshift is 6.3, with the typical around 2) but they occur very infrequently locally. Their luminosity also varies greatly as we have seen in this thesis, and so they are by no means standard candles. However, luminosity estimators allow one to calculate the luminosity of the GRBs from other observables and thereby allow them to be placed on the Hubble diagram (e.g., figure 6-1) (Schaefer 2003; Ghirlanda et al. 2004b; Firmani et al. 2006a,b). With the lack of nearby bursts, calibration becomes a problem due to the 'circularity' in using the cosmological parameters to establish the luminosity indicator relation, then using the luminosity indicators to fit for the cosmological parameters.

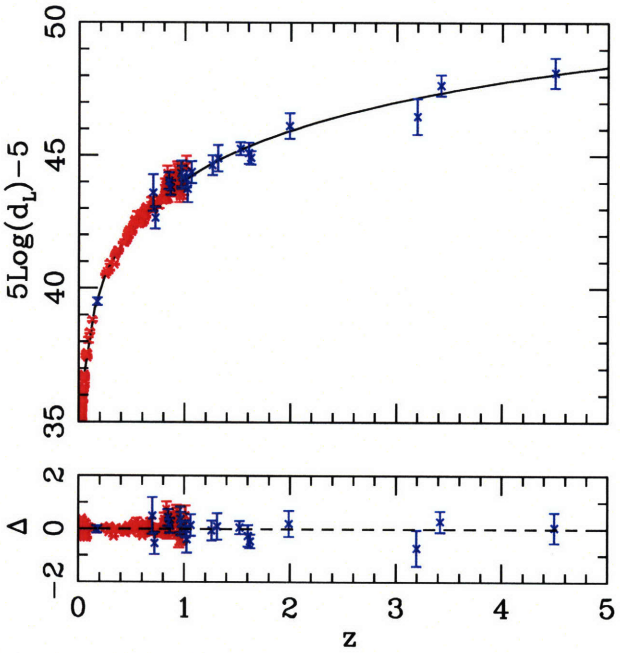

Figure 6-1: Top panel is a Hubble diagram of GRBs from Firmani et al. (2006b) for a concordance cosmology. The residuals are shown in the bottom panel. The red symbols are Type Ia supernovae, the blue are GRBs. Note the scarcity of GRBs at low redshift of the lack of SNe at high redshifts, hence the complementarity of the two types of objects. It is also clear that the GRB luminosity distances have much larger errors than those of supernovae.

Firmani et al. (2006b) solve this issue by fitting the cosmological parameters and the $L_{\rm iso}$–$E_{\rm pk}$–$T_{0.45}$ jointly with an iterative Bayesian approach. They show that their 19 GRB sample is complementary to the 117 SN Ia and greatly helps constrain the cosmological parameters. Furthermore, the best fit is consistent with the standard concordance cosmology.

A key point in the foregoing is that this type of analysis does not require an unbiased or complete flux-limit sample, but any set of bursts with spectroscopic redshifts and accurately determined spectral and temporal parameters. The sample sizes currently are too small for the confident investigation of deviation from concordance cosmology, but with larger samples of spectroscopic z's this method will be seen to

be a useful and independent complement to other techniques.

Statistical Studies

In contrast to the above, another type of study builds models out of luminosity functions, GRB rates, spectra, and cosmological parameters, and attempts to constrain cosmological parameters, sometimes jointly with GRB properties, with distributions of observables. These observables might be GRB peak intensity, peak flux, or the fractions of bursts that can be characterized as X-ray flashes, X-ray Rich bursts, or GRBs (Kommers et al. 2000; Firmani et al. 2004; Daigne et al. 2006). In these studies the completeness of the sample, freedom from observational biases, and known flux limits are important. The analyses in this thesis fall into this category, requiring complete, unbiased samples.

We have taken the concordance cosmology as a prior, which we believe is a well founded assumption. Firmani et al. (2006a) have pointed out that the $L_{\rm iso}$–$E_{\rm pk}$–$T_{0.45}$ relation has minimum variance near the concordance values of $\Omega_{\rm M}$ and Ω_Λ, and the exponents of $T_{0.45}$ and $E_{\rm pk}$ in the best fitting $L_{\rm iso}$–$E_{\rm pk}$–$T_{0.45}$ relation do not change significantly with $\Omega_{\rm M}$ and Ω_Λ. This gives us confidence in the robustness of our results. Our analysis of the GRB redshift distribution for cosmologies other than concordance, with an unaltered or slightly different $L_{\rm iso}$–$E_{\rm pk}$–$T_{0.45}$ would yield the same results, since the redshift estimator is calibrated against (invariant) spectroscopic redshifts. In an alternate cosmology, the main difference would be the luminosity–redshift relation (i.e., luminosity distance), which by calibration, would have to yield the same redshifts, though perhaps with slightly larger errors. The same could not be said of our luminosity function results, where the analysis would have to be carried through to investigate a change of $\Omega_{\rm M}$ and Ω_Λ.

We may conclude that our results point to a rough consistency of the GRB density with a uniform comoving density in the concordance model (see figure 4-18), however the derived rate density curve falls below the uniform density model for the nearby universe ($z < 1$). The log-normal redshift estimate errors in this region are large compared to the scale over which the GRB rate changes appreciably ($dN/d\ln(1+z)$)

and the deconvolution method that corrects for this bias is more susceptible to unknown systematic errors. Also, the scarcity of observations in the smaller cosmological volume in this redshift region leads to larger relative Poisson fluctuations.

At higher redshifts, the relative low rate is statistically consistent with the uniform density model within a standard deviation (fig 4-17), and though there are likely systematics affecting the measurements, such as the extrapolation of the Firmani relation to higher redshifts ($z >\sim 5$), we conclude that a rate several times what we infer is highly unlikely. Note that we see a decline in the rate relative to the constant density model already above a redshift of 2.5, which is *within* the range of the spectroscopic redshifts used in the Firmani relation.

6.4 GRB Rate and Star Formation Rate

By now there is much accumulated evidence to indicate that gamma-ray bursts, and long-duration bursts ($T_{90} > 2$ s) in particular, are associated with supernovae (for a recent review, see Woosley & Bloom 2006), star-forming galaxies and star-forming regions of galaxies (e.g. Paczyński 1998; Fruchter et al. 1999; Le Floc'h et al. 2003; Le Floc'h 2004). Coupled with the evidence that GRBs are likely the end-stage of massive, short-lived stars, it is logical to assume that the GRB rate should trace the cosmic star formation history. Interest in GRBs and their relation to stars is further heightened by the fact that the γ-rays are expected to be visible (not appreciably scattered or absorbed) out to very high redshift ($\sim$20)(Lamb & Reichart 2000). This could make possible the detection of the earliest stars ever formed, the so-called population-III (or Pop III) stars, which are thought to have reionized the Universe. Indeed, the recent discovery of a very long GRB with a spectroscopic redshift of 6.29 (Kawai et al. 2006), the highest one for a GRB to date, seems to point in this direction, as does the higher median redshift of *Swift* detections than those of previous missions.

Bromm & Loeb (2006) construct theoretical star formation models and calculate the expected GRB rate (figure 6-2) as well as the expected contribution from Pop III

stars. In particular, they calculate that with a limiting flux of 0.2 photons s^{-1} cm^{-2}, the fraction of bursts detected by *Swift* above a redshift of 5 is expected to be about 10%. They also calculate that Pop III stars are likely to be detected at the rate of only 0.1 yr^{-1}.

Our measured GRB rate density qualitatively agrees with the Bromm & Loeb (2006) predicted GRB formation rate, peaking close to a redshift of 2. These theoretical models agree with observation and detailed numerical simulations (Ascasibar et al. 2002; Mannucci et al. 2006). Given the Bromm & Loeb (2006) limits for *Swift*, we cannot reasonably hope to see any population III bursts in the *HETE-II* data, unless their rate were two to three orders of magnitude more frequent. Drawing inferences at redshifts as high as where the Pop III weak chemical feedback cases peak in figure 6-2 (the more favorable of the alternatives for purposes of detection), is also fraught with uncertainty since this would extrapolate the Firmani relation to well beyond the range where it was calibrated, as discussed in section 6.1.

Nevertheless, our current results also indicate that 10% of the *Swift* bursts should originate above a redshift of 5. Figure 6-3 shows in the dashed curve the cumulative rate of GRBs that we measure with our analysis. At a redshift of 5 this curve is at the 90% level. The dotted curve shows the cumulative distribution of *Swift*'s spectroscopic redshifts, which indicates that only about 5.6% (3 of 53) of the spectroscopic redshifts originate above $z = 5$. (Note that fast rise of this curve from zero seems to imply a dearth of low redshift bursts.) This is clearly a lower bound on the fraction, since only about a quarter of *Swift* bursts have spectroscopically determined redshifts. Since *Swift*'s flux limit is much lower than that of *HETE-II*, its overall cumulative should more closely follow the form found with the Lynden-Bell method and the Firmani redshift estimates (compare the dotted and dashed curve in figure 6-3).

6.5 Future Projects

Looking forward, we see the greatest avenue for progress in further observational confirmation and more tests of the Firmani relation. With more bursts available,

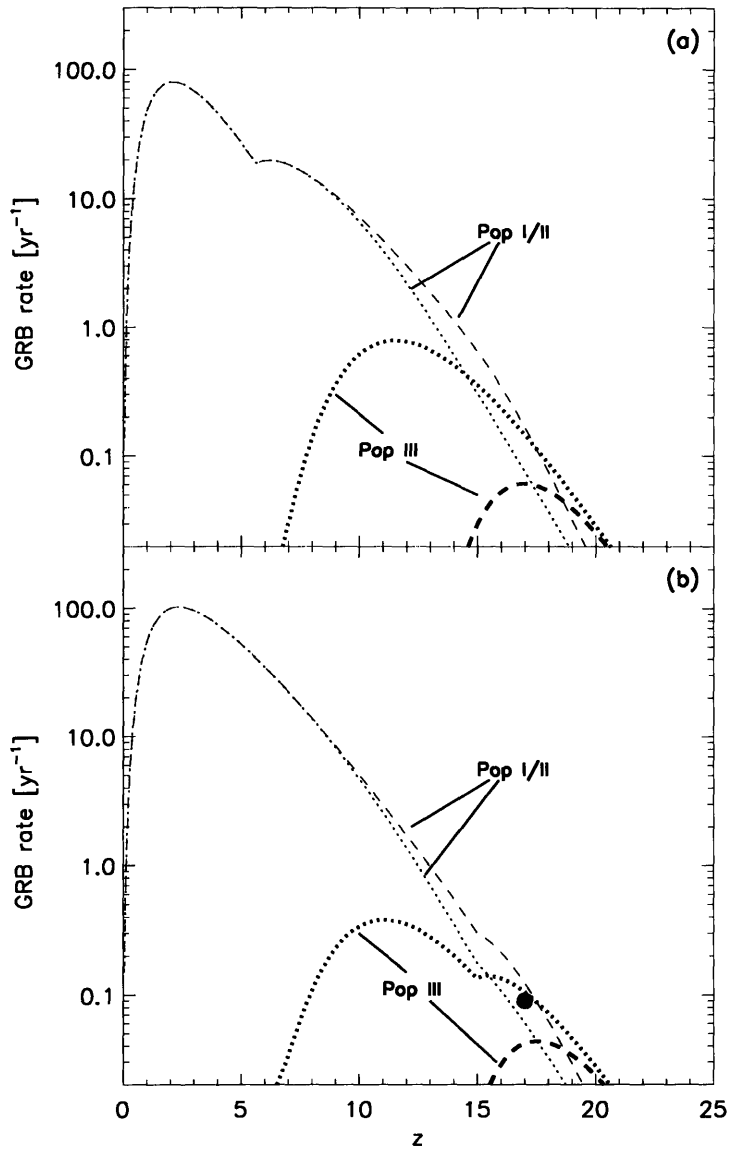

Figure 6-2: Figure 2 of Bromm & Loeb (2006). Predicted *Swift* observation rates of gamma-ray bursts for late reionization (top panel) and early reionization (bottom panel). Contributions to Pop I/II and Pop III formation rates under weak and strong chemical feedback (dotted and dashed lines). The large dot is the GRB rate from Pop III stars under the assumption that they reionized the Universe at $z \sim 17$. Of note is the very small contribution of Pop III stars to the integral under the curves in all cases.

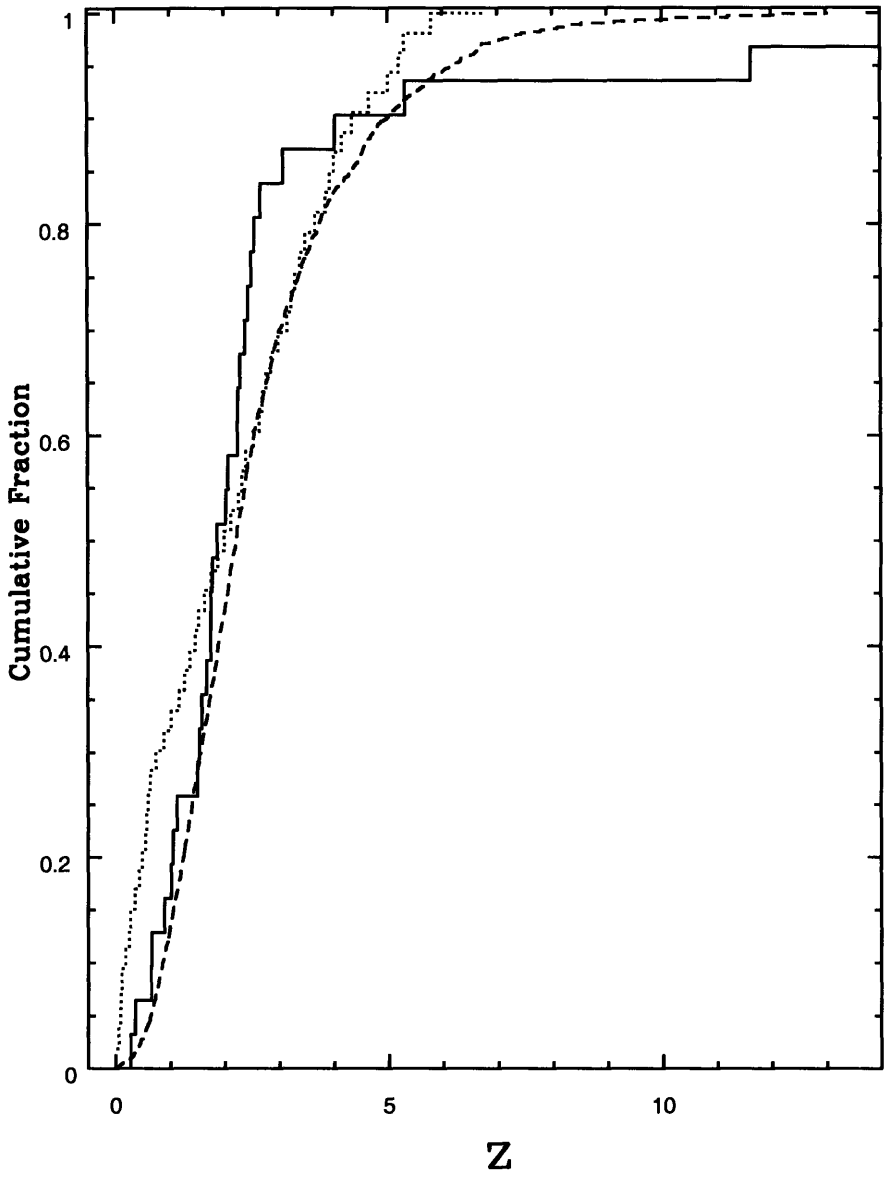

Figure 6-3: Cumulative redshift distribution of GRBs. The dotted line indicates the spectroscopically measured *Swift* bursts. The solid staircase is the Firmani redshift estimates of the 31 bursts in our sample. The dashed line represents the cumulative of redshift estimates derived with the Lynden-Bell C–method (chapter 4).

the intrinsic scatter of the relation will be reduced, and it might be possible that the properties of outliers, and the reasons for their being outliers will become clear. With more bursts, the number that will have well-determined spectral properties will also increase. It is also possible that record setting high-redshift spectroscopic observations will be able to calibrate or confirm the relation at high z. It will be possible to better quantify the luminosity evolution, and as mentioned above, the form of the luminosity function will be better determined at each redshift interval. The evolution parametrization of $(1+z)^{-k}$ can then be also tested. We would also expect to see an improvement in the errors of the GRB rate vs. redshift curve as the square-root of the increase in the number of bursts. Finally, it is also possible that other, tighter, relations will be discovered that can serve as redshift estimators with even smaller error.

Clearly there will still be a need for redshift estimators to attain flux-limited samples free of spectroscopic observational bias. More *HETE-II* bursts are not likely, certainly not in large numbers. *Swift* has trouble determining $E_{\rm pk}$ for $\sim$75% of bursts detected (Butler 2006) so applying the Firmani relation will not avoid selection biases.

More promising is the Gamma-Ray Large Area Space Telescope (*GLAST*) with its Burst Monitor (GBM) (Lichti et al. 2001), to be launched by NASA on 7 October 2007. This instrument has an energy pass-band of 5 keV to 25 MeV and will provide unprecedented ability to determine $E_{\rm pk}$ over a large energy range. Operating together with *Swift* to provide accurate locations, the two missions will be able to fully characterize bursts and test the Firmani relation.

Our ideas, including the background subtraction method, would also be applicable to the proposed small satellites with coded aperture detectors that could detect $\sim$1000 GRBs per year (Lamb et al. 2005), and to the *EXIST* mission which is planned to detect just as many (Grindlay & The Exist Team 2006). With the Firmani relation, a complete L–z sample could be attained with only selective follow-up afterglow observations from the ground.

6.6 Summary

In this thesis we report the development of a new background subtraction technique for coded aperture mask instruments, and a new approach for determining GRB duration statistics via a photon-by-photon bootstrap analysis of event-level data. We then analyze the *HETE-II* WXM bursts using these techniques.

We are the first to apply to a complete flux-limited sample of bursts a recently discovered luminosity and redshift indicator that is based only on the prompt emission properties of GRBs (Firmani et al. 2006c).

Using our bootstrap calculation of the confidence regions of the duration statistics and the estimated redshifts of 31 GRBs, we analyze both the observed and intrinsic duration distribution properties of GRBs. We show that the observed distributions of T_{90} are highly affected by measurement errors of log-normal form. It is possible that the true intrinsic distribution of GRB durations may not be log-normal, contrary to assumptions in several publications (McBreen et al. 1994, 2001; Ioka & Nakamura 2002; Horváth 2002). We compare the *HETE-II* T_{90} results with those reported for the BATSE catalog. We further show, for the first time, that the intrinsic $T_{0.45}$ distribution is best modeled by an exponential with a mean $T_{0.45}$ of 6 ± 1 seconds.

With a rank-order correlation analysis that takes into account the flux limitation of the sample, we see strong evidence ($5.7\ \sigma$) for the evolution of GRB luminosities as $L \propto (1+z)^{1.03}$.

We calculate the redshift distribution and the luminosity function of GRBs, correcting for the flux limitation of the *HETE-II* WXM and FREGATE instruments with the non-parametric method of Lynden-Bell (1971). We develop and apply a Monte-Carlo method to account for errors in the redshift estimates. These errors are log-normal and large, unlike the errors in spectroscopic and photometric redshifts that tend to be Gaussian and small. We also use a bootstrap approach to estimate the confidence region of the measured GRB redshift distribution.

Our results show that the GRB rate density falls off beyond a redshift of two, consistent with the Kocevski & Liang (2006) analysis of *BATSE* bursts and with

theoretical predictions of Bromm & Loeb (2006).

Our flux-corrected GRB rates imply that *Swift* will detect 10% of its bursts at redshifts greater than five, also in agreement with the theoretical star formation models of Bromm & Loeb (2006).

The methods set forth in this thesis will be applicable to future missions, with the greatest improvement resulting from a larger sample of bursts.

Appendix A

WXM Bursts

Table A.1 lists the temporal parameters for the sample of 31 bursts used in our analysis to determine the GRB rate and luminosity function. Table A.2 lists the $E_{\rm pk}^{\rm obs}$, the peak flux, and the parameters of the cutoff power-law spectral model for the same bursts. Table A.3 lists the redshift indicator and isotropic equivalent luminosity implied by the $L_{\rm iso}$–$E_{\rm pk}$–$T_{0.45}$ (Firmani) relation.

Figures A-1 through A-31 show lightcurves and distributions of T_{90} and $T_{0.45}$ (along with confidence regions) for the 31 bursts in the sample.

Burst ID	GRB name	$T_{0.45}^{\rm obs}$	T_{90}
1896	GRB020124	$9.4^{+4.1}_{-4.9}$	$47.2^{+2.8}_{-8.1}$
1902	GRB020127	$5.2^{+2.6}_{-2.1}$	$50.6^{+32.7}_{-24.1}$
1963	GRB020331	$16.7^{+2.6}_{-3.3}$	$47.7^{+4.5}_{-4.9}$
2262	GRB020813A	$20.8^{+0.6}_{-0.6}$	$75.1^{+1.3}_{-1.6}$
2380	GRB021004	$16.0^{+4.1}_{-4.5}$	$65.5^{+4.8}_{-8.5}$
2434	GRB021104A	$9.4^{+2.8}_{-3.0}$	$36.4^{+10.2}_{-5.8}$
2448	GRB021112A	$0.9^{+1.1}_{-0.7}$	$14.6^{+5.0}_{-7.7}$
2493	GRB021211	$2.7^{+0.6}_{-0.3}$	$28.5^{+52.1}_{-20.5}$
2650	GRB030328	$31.3^{+3.4}_{-10.9}$	$70.9^{+8.4}_{-26.8}$
2652	GRB030329A	$12.0^{+0.2}_{-0.2}$	$43.1^{+1.9}_{-2.1}$
2779	GRB030725	$26.4^{+4.7}_{-4.0}$	$202.5^{+44.2}_{-13.0}$
2818	GRB030823	$27.3^{+7.2}_{-8.7}$	$96.5^{+10.8}_{-18.0}$
2821	GRB030824	$4.4^{+2.0}_{-1.9}$	$27.1^{+9.6}_{-7.0}$
2849	GRB030913	$2.5^{+1.4}_{-1.2}$	$18.2^{+1.8}_{-5.5}$
2925	GRB031111B	$7.9^{+3.8}_{-3.0}$	$46.9^{+12.6}_{-12.0}$
2976	GRB031220	$6.2^{+2.1}_{-2.0}$	$28.7^{+10.0}_{-6.6}$
3128	GRB040319	$3.5^{+2.3}_{-2.2}$	$25.1^{+7.0}_{-9.4}$
3218	GRB040511	$11.5^{+3.3}_{-3.0}$	$47.4^{+5.2}_{-10.9}$
3489	GRB040810	$11.5^{+3.1}_{-2.2}$	$71.1^{+38.2}_{-24.3}$
3557	GRB040912B	$24.1^{+6.9}_{-6.9}$	$86.3^{+10.8}_{-14.1}$
3558	GRB040916	$22.0^{+5.1}_{-5.3}$	$86.9^{+9.3}_{-9.2}$
3564	GRB040924	$2.3^{+4.3}_{-0.9}$	$75.6^{+56.7}_{-45.8}$
3568	GRB041004	$5.7^{+4.3}_{-3.7}$	$47.6^{+12.6}_{-14.8}$
3570	GRB041006	$12.7^{+0.4}_{-0.4}$	$35.7^{+2.6}_{-2.5}$
3622	GRB041211B	$12.6^{+2.4}_{-2.3}$	$39.7^{+12.9}_{-6.3}$
3666	GRB050123A	$6.2^{+2.0}_{-2.0}$	$30.1^{+7.2}_{-6.9}$
3711	GRB050408	$12.1^{+0.7}_{-0.6}$	$33.8^{+2.7}_{-2.6}$
3862	GRB050709	$0.2^{+0.3}_{-0.2}$	$4.7^{+4.3}_{-3.3}$
3889	GRB050807	$14.5^{+2.9}_{-2.9}$	$50.6^{+9.5}_{-5.3}$
3947	GRB051021	$19.1^{+5.1}_{-6.1}$	$74.0^{+32.3}_{-29.6}$
4010	GRB060121	$1.5^{+0.4}_{-0.4}$	$6.8^{+2.1}_{-1.8}$

Table A.1: Temporal properties of the bursts in our sample. The measurements and errors are derived by the methods of chapter 3. Error limits indicate 68% confidence regions centered on the median values.

BID	GRB name	E_{pk}^{obs}(keV)	P (erg cm^{-2} s^{-1})	α^1	$E_0{}^1$	A^1
1896	GRB020124	91.73	4.56×10^{-7}	-0.994	91.18	5.030
1902	GRB020127	123.83	1.89×10^{-6}	-0.7788	101.4	3.563
1963	GRB020331	123.29	6.68×10^{-7}	-0.8542	107.6	3.137
2262	GRB020813A	186.50	2.85×10^{-6}	-0.5914	132.4	3.727
2380	GRB021004	96.52	3.99×10^{-7}	-1.004	96.91	2.690
2434	GRB021104A	38.98	1.84×10^{-7}	-0.453	25.20	1.434
2448	GRB021112A	18.63	1.71×10^{-7}	-0.9986	18.60	2.535
2493	GRB021211	68.28	2.16×10^{-6}	-1.346	104.4	86.15
2650	GRB030328	177.08	1.25×10^{-6}	-0.9326	165.9	1.778
2652	GRB030329A	108.79	1.05×10^{-5}	-1.366	171.6	51.92
2779	GRB030725	133.39	1.63×10^{-6}	-1.195	165.7	23.88
2818	GRB030823	42.06	2.60×10^{-7}	-1.156	49.83	5.311
2821	GRB030824	60.44	2.90×10^{-7}	-0.2571	34.68	0.0771
2849	GRB030913	160.08	7.32×10^{-7}	-1.031	165.2	5.487
2925	GRB031111B	59.06	2.68×10^{-7}	-0.538	40.40	0.2236
2976	GRB031220	41.96	2.89×10^{-7}	-0.4983	27.94	0.9415
3128	GRB040319	210.98	7.88×10^{-7}	-1.656	613.3	11.40
3218	GRB040511	141.31	9.38×10^{-7}	-0.5768	99.29	1.307
3489	GRB040810	198.60	1.74×10^{-6}	-0.8283	169.5	8.614
3557	GRB040912B	53.98	1.81×10^{-7}	-0.9874	53.31	2.222
3558	GRB040916	39.10	1.47×10^{-7}	-0.7663	31.69	0.4007
3564	GRB040924	51.95	2.53×10^{-6}	-1.164	62.14	57.58
3568	GRB041004	57.20	3.67×10^{-7}	-1.244	75.66	19.71
3570	GRB041006	63.19	1.51×10^{-6}	-1.338	95.46	65.32
3622	GRB041211B	359.97	2.45×10^{-6}	-0.8924	325.0	2.972
3666	GRB050123A	70.89	4.86×10^{-7}	-0.9844	69.80	8.938
3711	GRB050408	19.45	1.11×10^{-6}	-1.979	926.3	190.4
3862	GRB050709	91.92	3.04×10^{-6}	-0.9083	84.20	20.36
3889	GRB050807	159.05	4.91×10^{-7}	-1.828	924.7	38.34
3947	GRB051021	143.84	7.85×10^{-7}	-0.8665	126.9	1.153
4010	GRB060121	144.54	3.80×10^{-6}	-0.6629	108.1	8.531

Table A.2: Spectral properties of the bursts in our sample, including the parameters of the cutoff power-law fit, the peak flux and the peak of the energy spectrum.
[1]These parameters are defined for the cutoff power-law model in section 1.1.3. Units of E_0 are keV and of A are cm^{-2} s^{-1}.

BID	GRB name	z′	L′ (erg s^{-1})
1896	GRB020124	2.66	2.64×10^{52}
1902	GRB020127	1.53	2.85×10^{52}
1963	GRB020331	2.24	2.55×10^{52}
2262	GRB020813A	1.12	1.99×10^{52}
2380	GRB021004	2.55	2.08×10^{52}
2434	GRB021104A	1.74	3.81×10^{51}
2448	GRB021112A	1.77	3.72×10^{51}
2493	GRB021211	0.89	8.58×10^{51}
2650	GRB030328	1.66	2.32×10^{52}
2652	GRB030329A	0.35	4.64×10^{51}
2779	GRB030725	1.05	9.66×10^{51}
2818	GRB030823	1.01	1.41×10^{51}
2821	GRB030824	3.08	2.39×10^{52}
2849	GRB030913	11.6	1.32×10^{54}
2925	GRB031111B	2.43	1.24×10^{52}
2976	GRB031220	1.58	4.69×10^{51}
3128	GRB040319	18.4	3.99×10^{54}
3218	GRB040511	2.37	4.13×10^{52}
3489	GRB040810	2.23	6.62×10^{52}
3557	GRB040912B	1.86	4.40×10^{51}
3558	GRB040916	1.50	2.11×10^{51}
3564	GRB040924	0.65	4.61×10^{51}
3568	GRB041004	2.02	1.09×10^{52}
3570	GRB041006	0.64	2.70×10^{51}
3622	GRB041211B	4.03	3.84×10^{53}
3666	GRB050123A	2.06	1.52×10^{52}
3711	GRB050408	0.26	2.49×10^{50}
3862	GRB050709	2.49	1.50×10^{53}
3889	GRB050807	5.30	1.47×10^{53}
3947	GRB051021	2.28	3.15×10^{52}
4010	GRB060121	1.74	7.88×10^{52}

Table A.3: Shown are the redshift estimates and the isotropic luminosities based on the $L_{\rm iso}$–$E_{\rm pk}$–$T_{0.45}$ relation and concordance cosmology. Results are based on the duration and spectral values of tables A.1 and A.2.

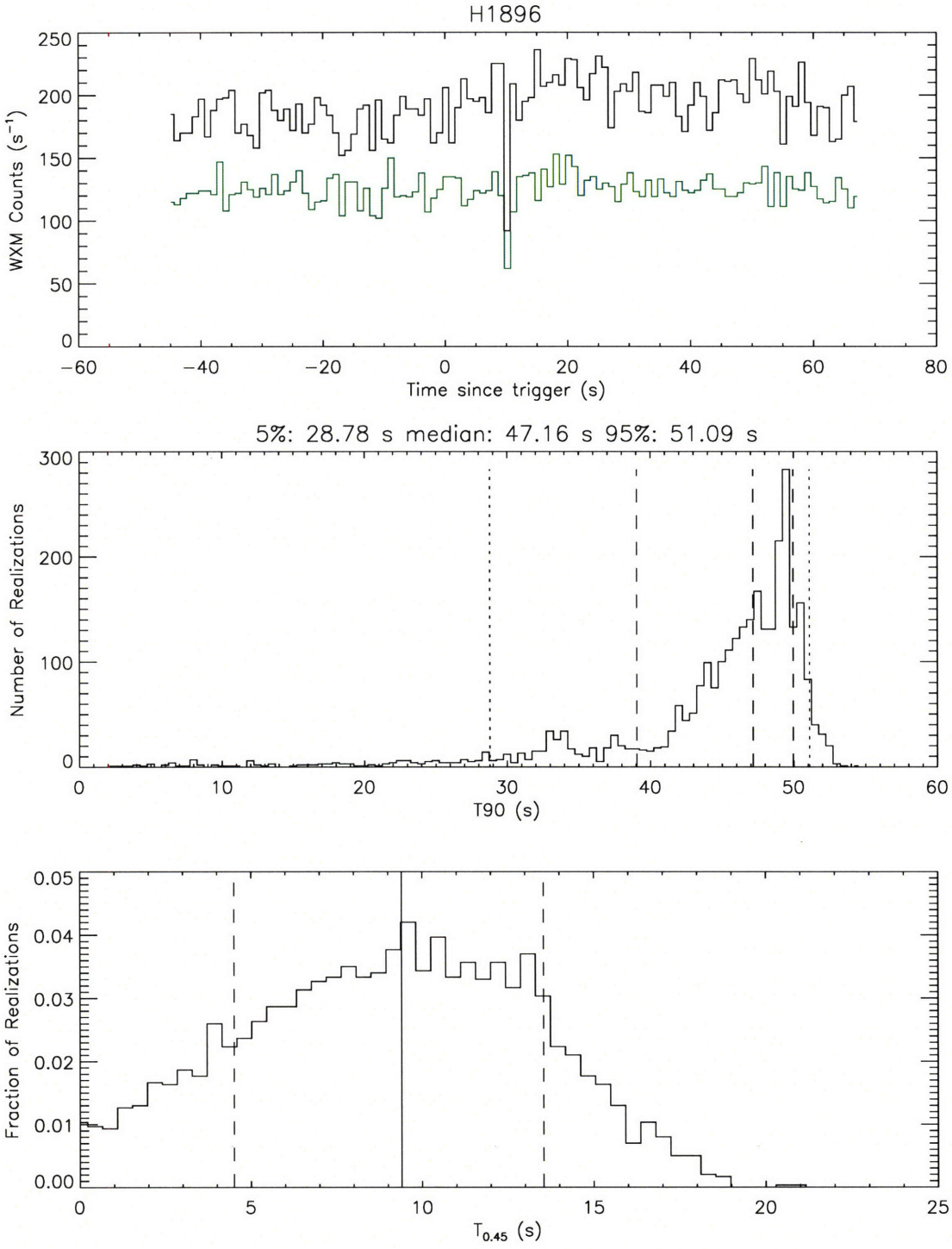

Figure A-1: BID H1896. The top panel shows the burst lightcurve and the background rate (in green). The middle panel shows the T_{90} distribution, with dashed lines indicating the median and one standard deviation, and dotted lines bounding the 90% confidence region. The bottom panel shows the $T_{0.45}$ distribution with a solid line indicating the median and dashed lines showing one standard deviations.

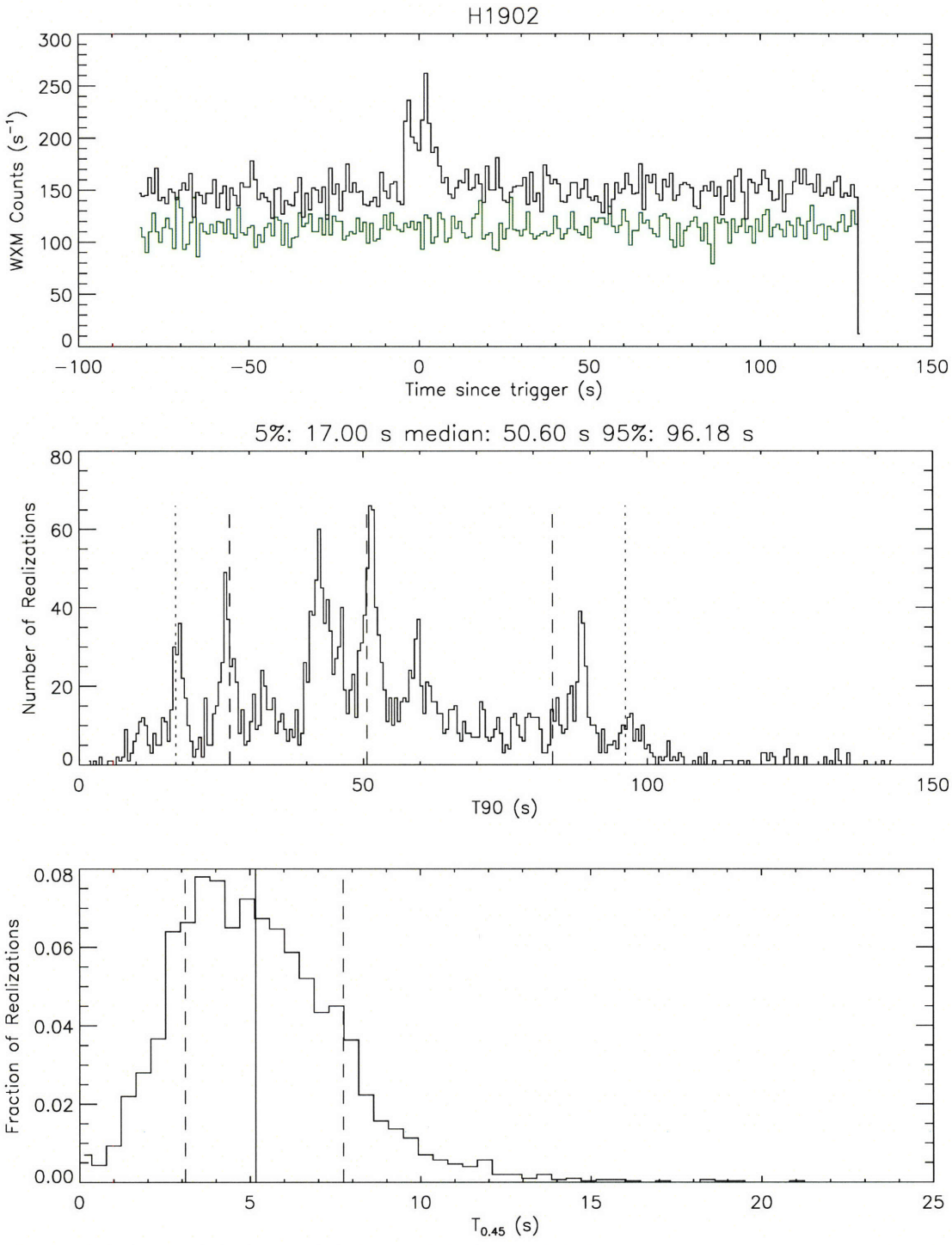

Figure A-2: BID H1902. The top panel shows the burst lightcurve and the background rate (in green). The middle panel shows the T_{90} distribution, with dashed lines indicating the median and one standard deviation, and dotted lines bounding the 90% confidence region. The bottom panel shows the $T_{0.45}$ distribution with a solid line indicating the median and dashed lines showing one standard deviations.

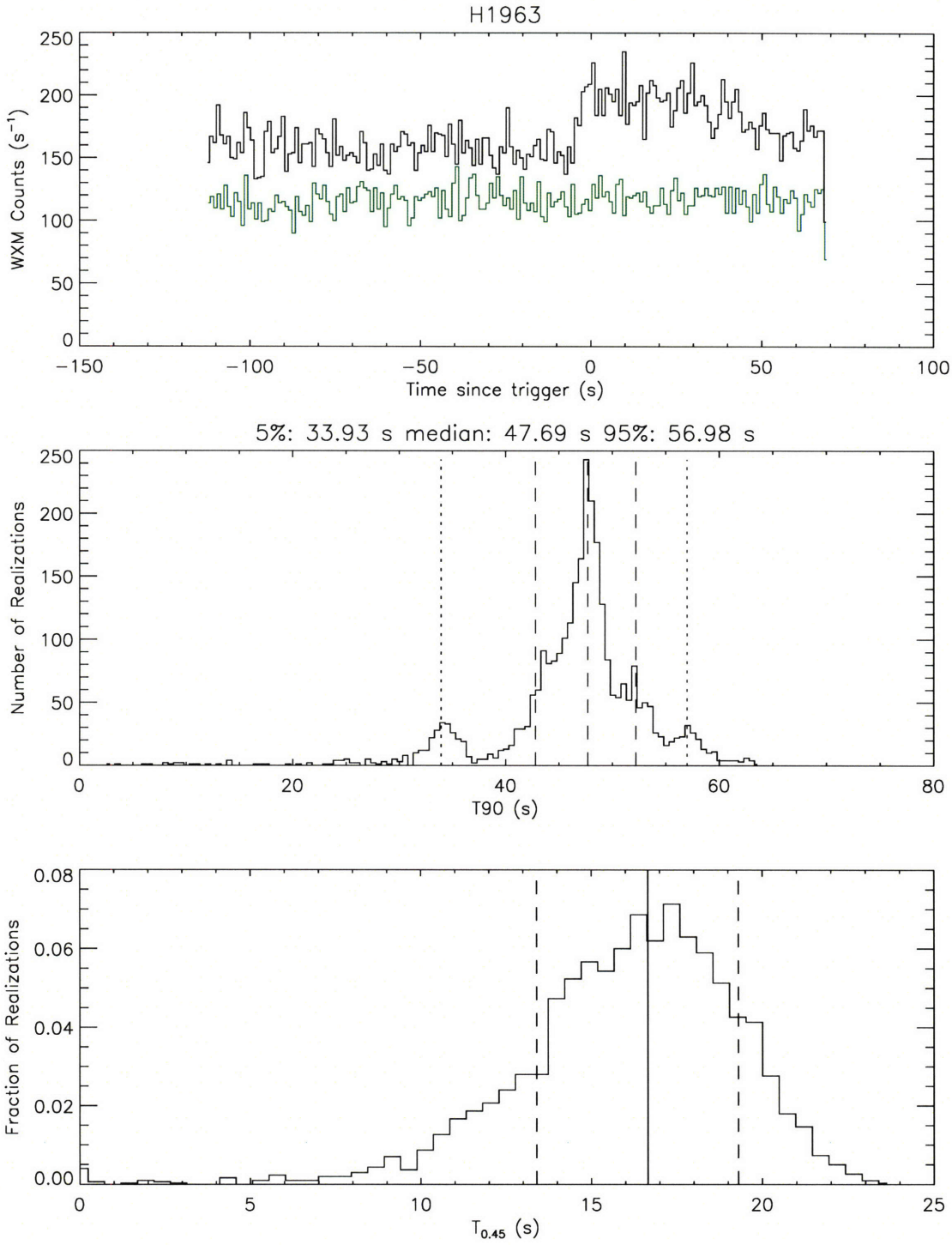

Figure A-3: BID H1963. The top panel shows the burst lightcurve and the background rate (in green). The middle panel shows the T_{90} distribution, with dashed lines indicating the median and one standard deviation, and dotted lines bounding the 90% confidence region. The bottom panel shows the $T_{0.45}$ distribution with a solid line indicating the median and dashed lines showing one standard deviations.

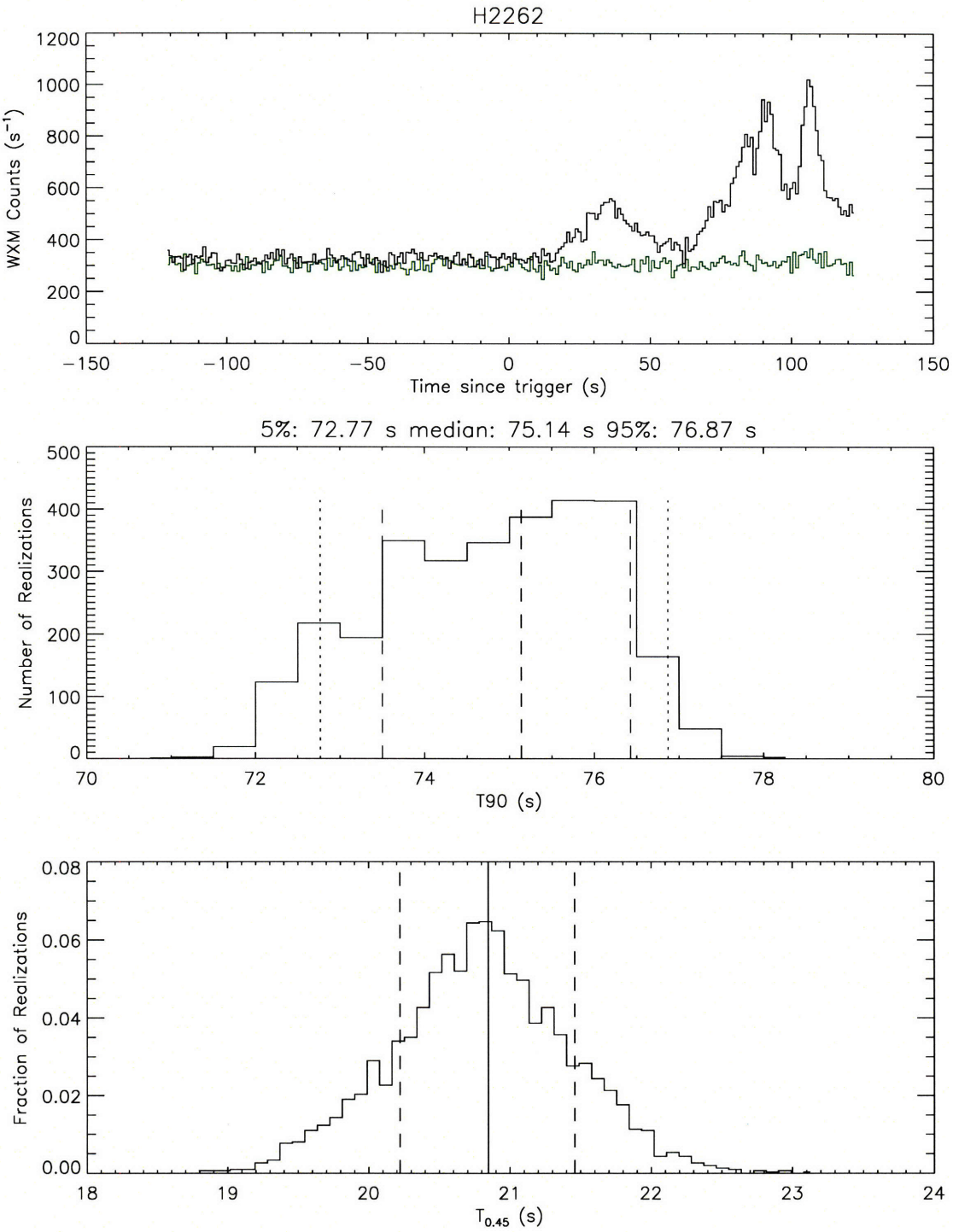

Figure A-4: BID H2262. The top panel shows the burst lightcurve and the background rate (in green). The middle panel shows the T_{90} distribution, with dashed lines indicating the median and one standard deviation, and dotted lines bounding the 90% confidence region. The bottom panel shows the $T_{0.45}$ distribution with a solid line indicating the median and dashed lines showing one standard deviations.

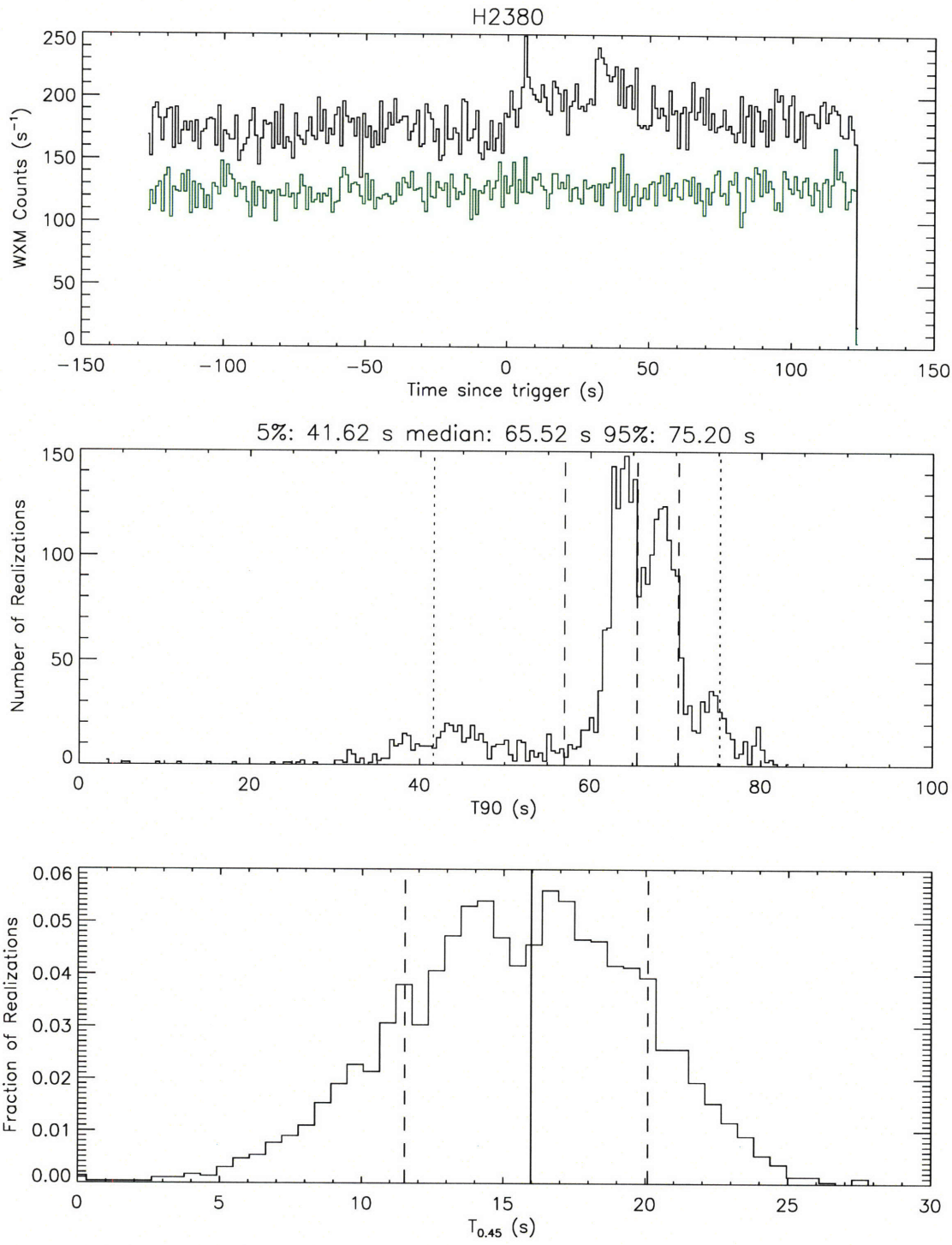

Figure A-5: BID H2380. The top panel shows the burst lightcurve and the background rate (in green). The middle panel shows the T_{90} distribution, with dashed lines indicating the median and one standard deviation, and dotted lines bounding the 90% confidence region. The bottom panel shows the $T_{0.45}$ distribution with a solid line indicating the median and dashed lines showing one standard deviations.

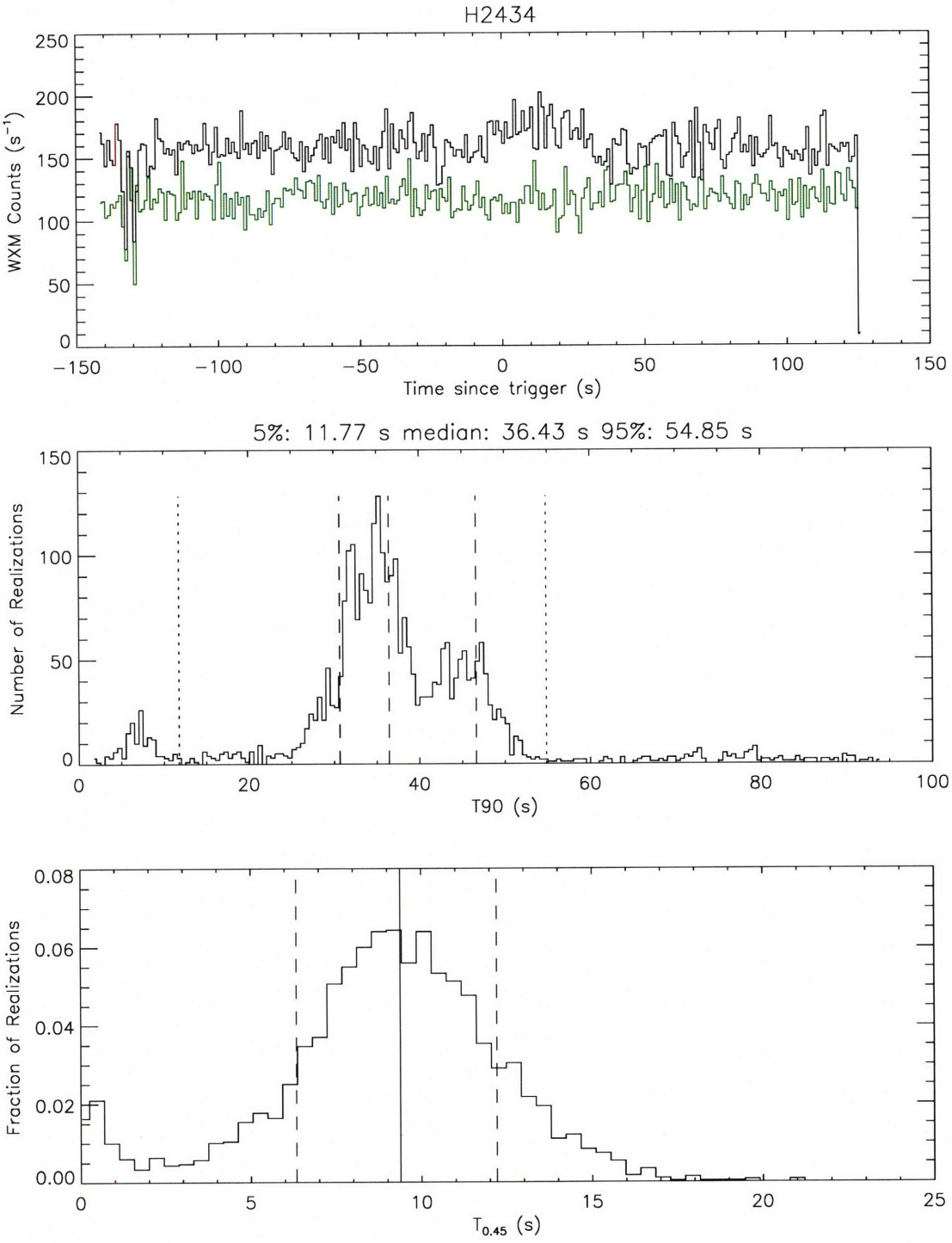

Figure A-6: BID H2434. The top panel shows the burst lightcurve and the background rate (in green). The middle panel shows the T_{90} distribution, with dashed lines indicating the median and one standard deviation, and dotted lines bounding the 90% confidence region. The bottom panel shows the $T_{0.45}$ distribution with a solid line indicating the median and dashed lines showing one standard deviations.

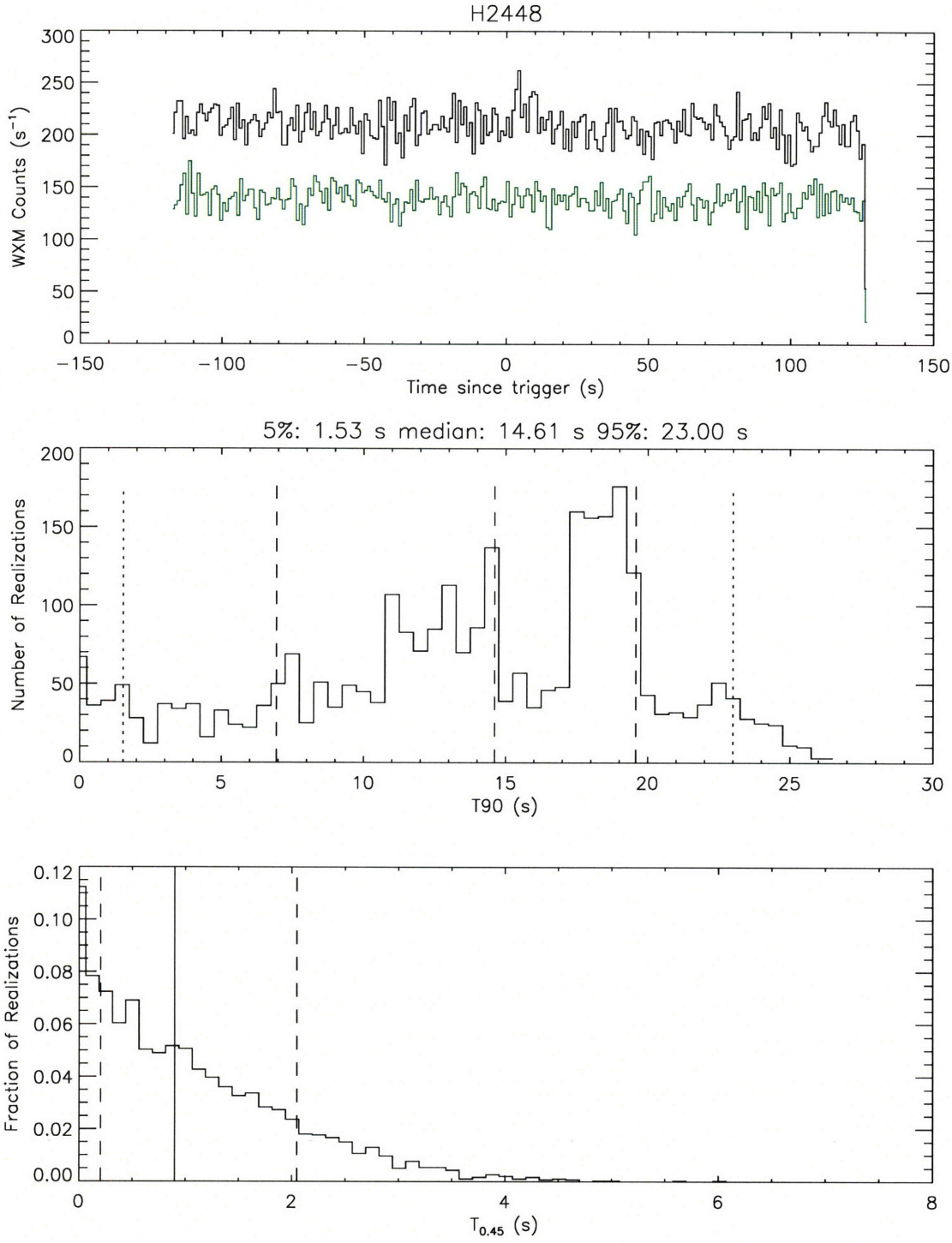

Figure A-7: BID H2448. The top panel shows the burst lightcurve and the background rate (in green). The middle panel shows the T_{90} distribution, with dashed lines indicating the median and one standard deviation, and dotted lines bounding the 90% confidence region. The bottom panel shows the $T_{0.45}$ distribution with a solid line indicating the median and dashed lines showing one standard deviations.

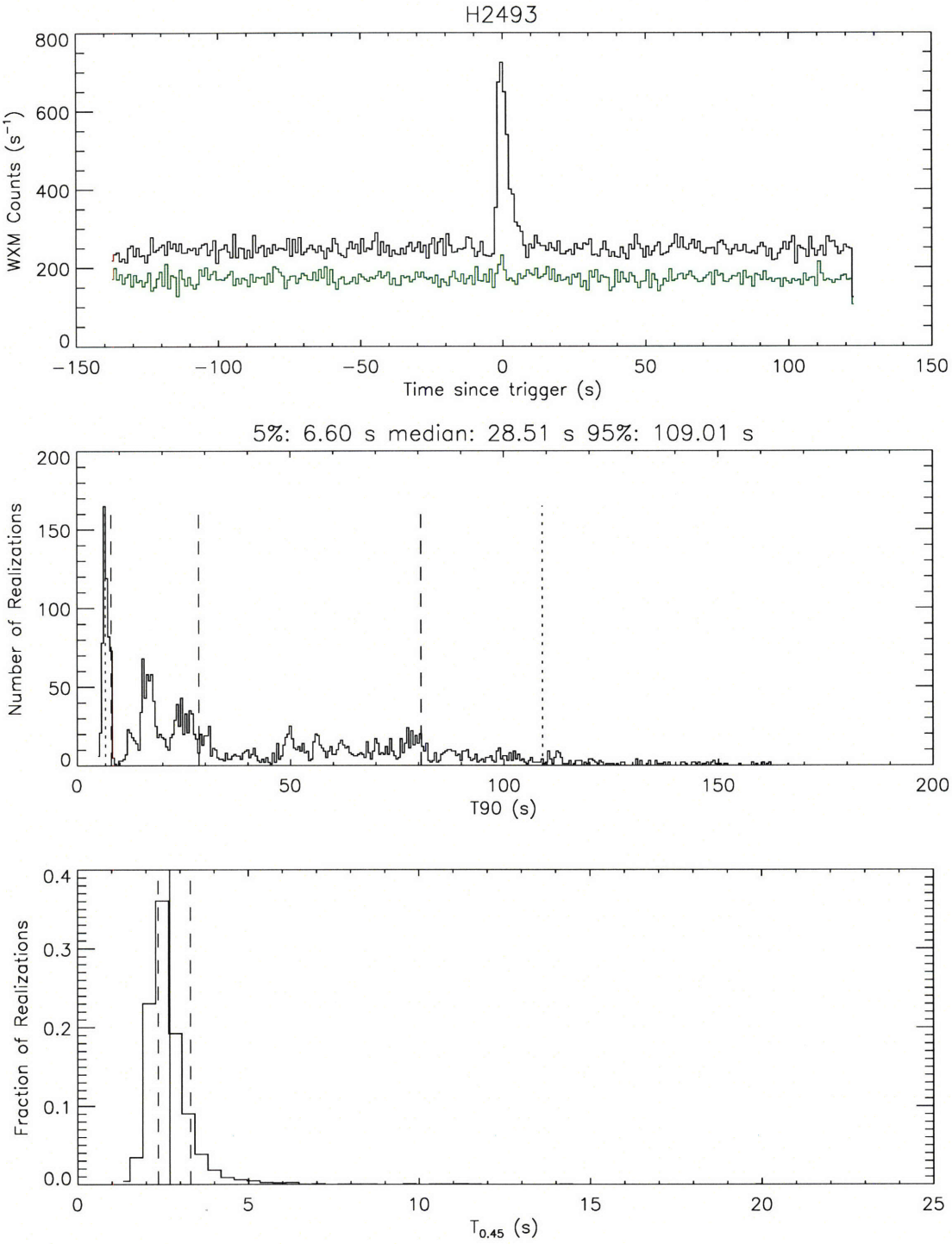

Figure A-8: BID H2493. The top panel shows the burst lightcurve and the background rate (in green). The middle panel shows the T_{90} distribution, with dashed lines indicating the median and one standard deviation, and dotted lines bounding the 90% confidence region. The bottom panel shows the $T_{0.45}$ distribution with a solid line indicating the median and dashed lines showing one standard deviations.

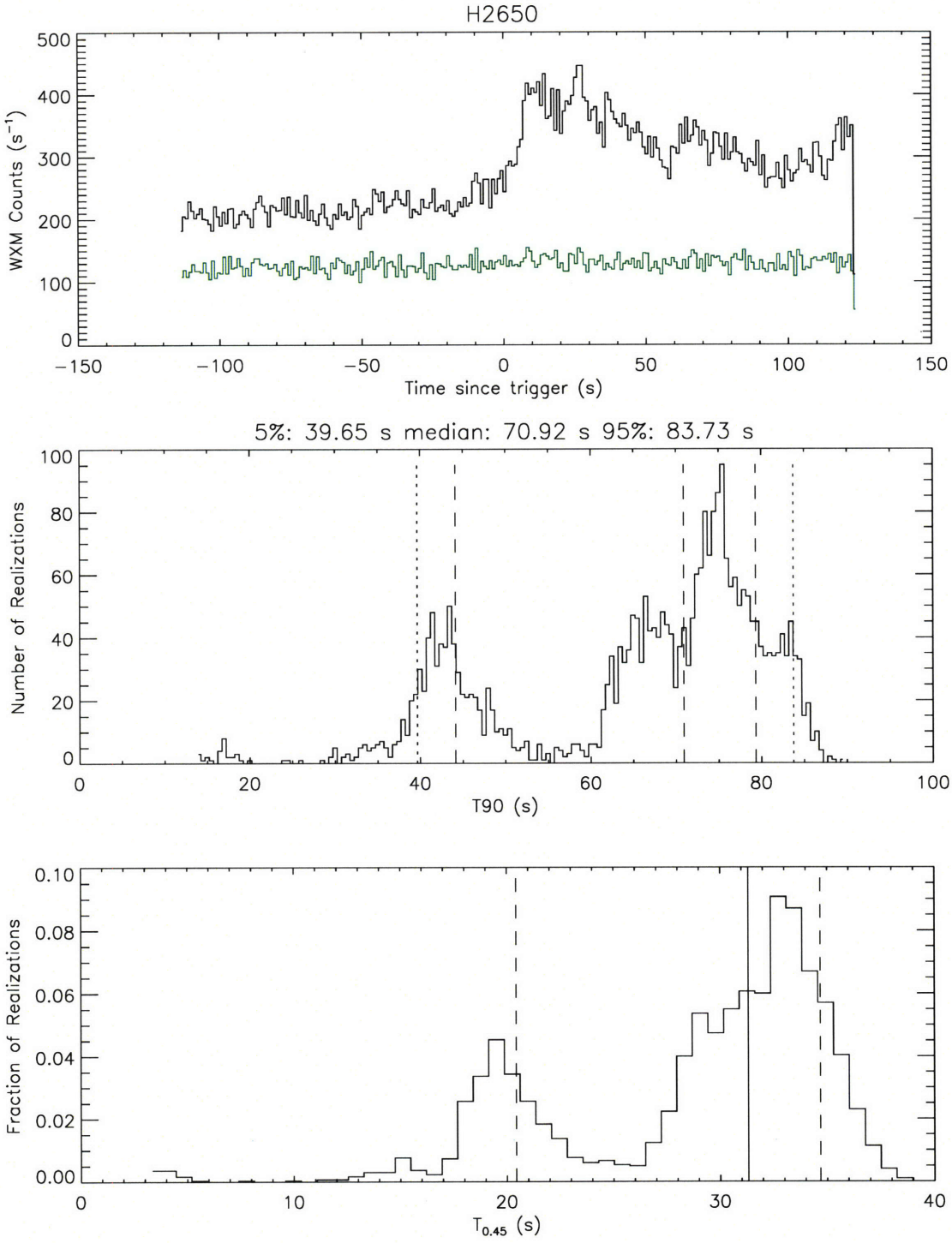

Figure A-9: BID H2650. The top panel shows the burst lightcurve and the background rate (in green). The middle panel shows the T_{90} distribution, with dashed lines indicating the median and one standard deviation, and dotted lines bounding the 90% confidence region. The bottom panel shows the $T_{0.45}$ distribution with a solid line indicating the median and dashed lines showing one standard deviations.

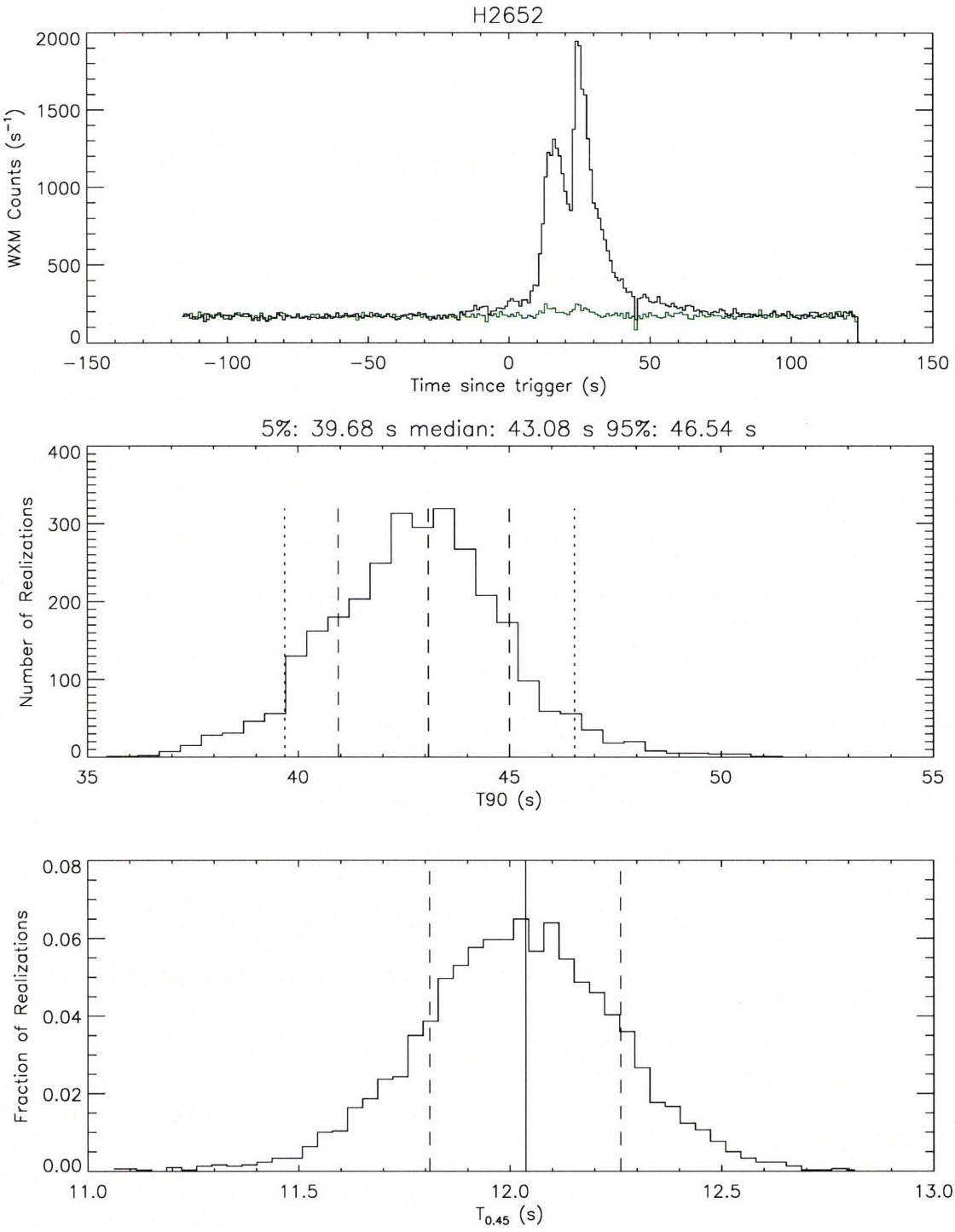

Figure A-10: BID H2652. The top panel shows the burst lightcurve and the background rate (in green). The middle panel shows the T_{90} distribution, with dashed lines indicating the median and one standard deviation, and dotted lines bounding the 90% confidence region. The bottom panel shows the $T_{0.45}$ distribution with a solid line indicating the median and dashed lines showing one standard deviations.

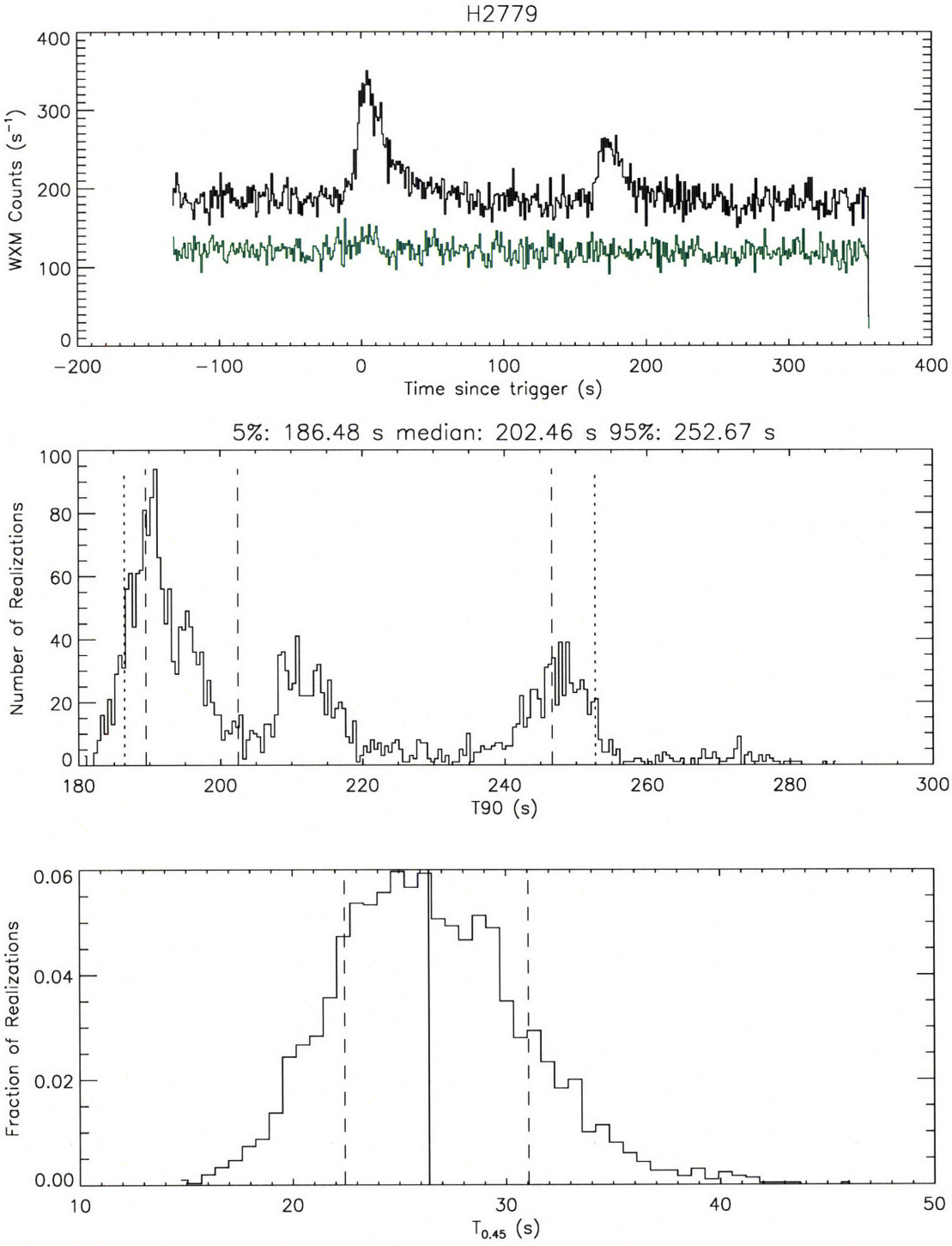

Figure A-11: BID H2779. The top panel shows the burst lightcurve and the background rate (in green). The middle panel shows the T_{90} distribution, with dashed lines indicating the median and one standard deviation, and dotted lines bounding the 90% confidence region. The bottom panel shows the $T_{0.45}$ distribution with a solid line indicating the median and dashed lines showing one standard deviations.

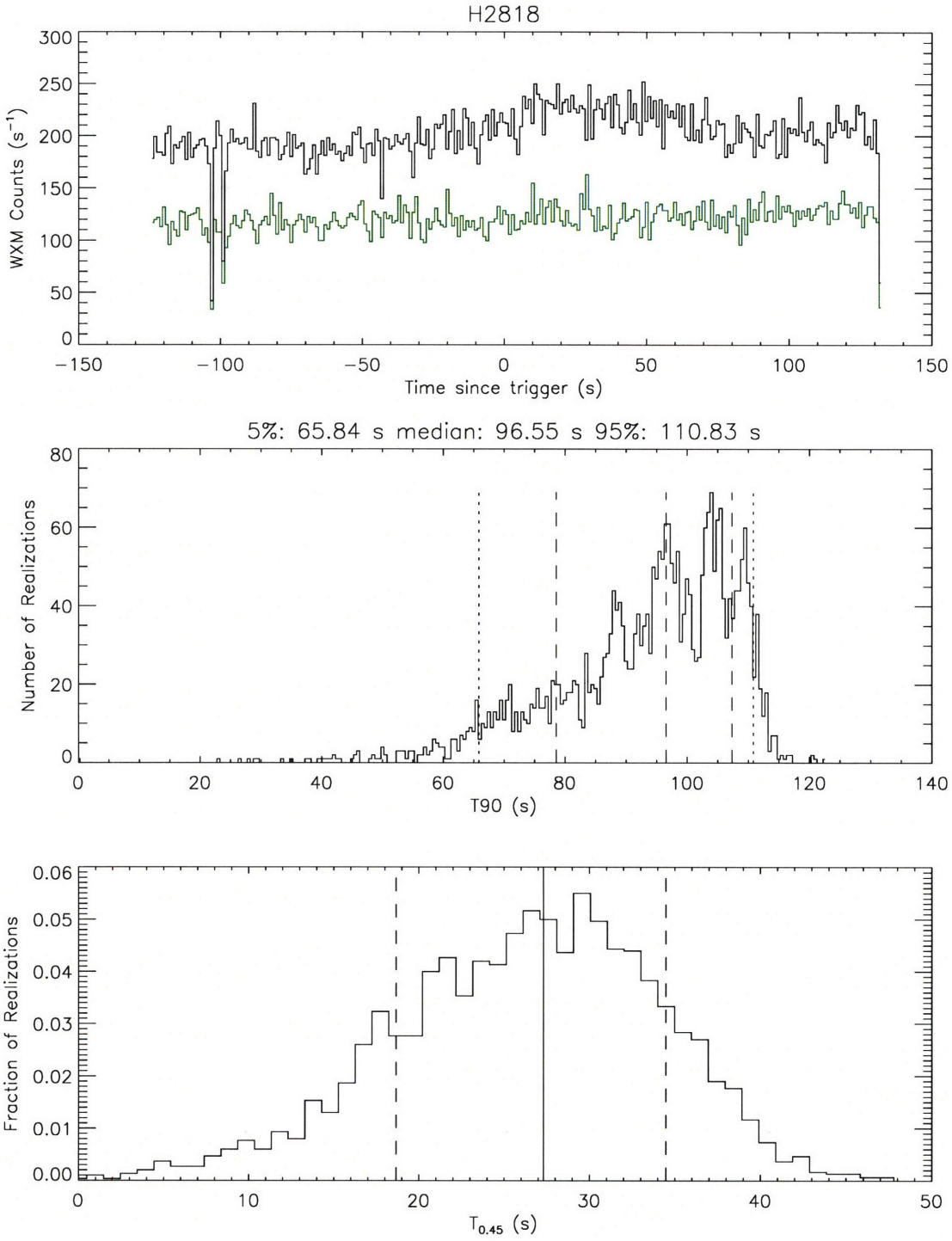

Figure A-12: BID H2818. The top panel shows the burst lightcurve and the background rate (in green). The middle panel shows the T_{90} distribution, with dashed lines indicating the median and one standard deviation, and dotted lines bounding the 90% confidence region. The bottom panel shows the $T_{0.45}$ distribution with a solid line indicating the median and dashed lines showing one standard deviations.

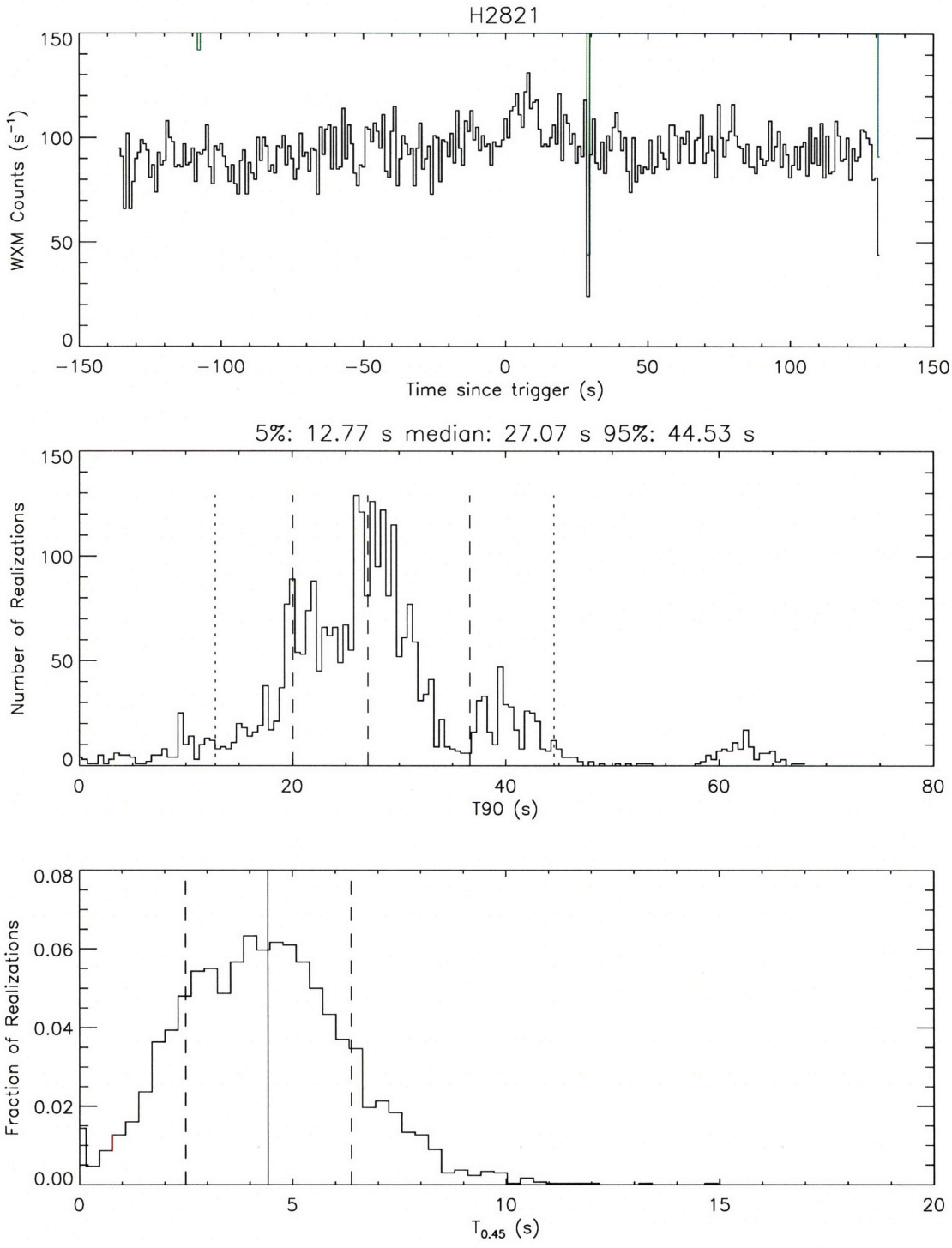

Figure A-13: BID H2821. The top panel shows the burst lightcurve and the background rate (in green). The middle panel shows the T_{90} distribution, with dashed lines indicating the median and one standard deviation, and dotted lines bounding the 90% confidence region. The bottom panel shows the $T_{0.45}$ distribution with a solid line indicating the median and dashed lines showing one standard deviations.

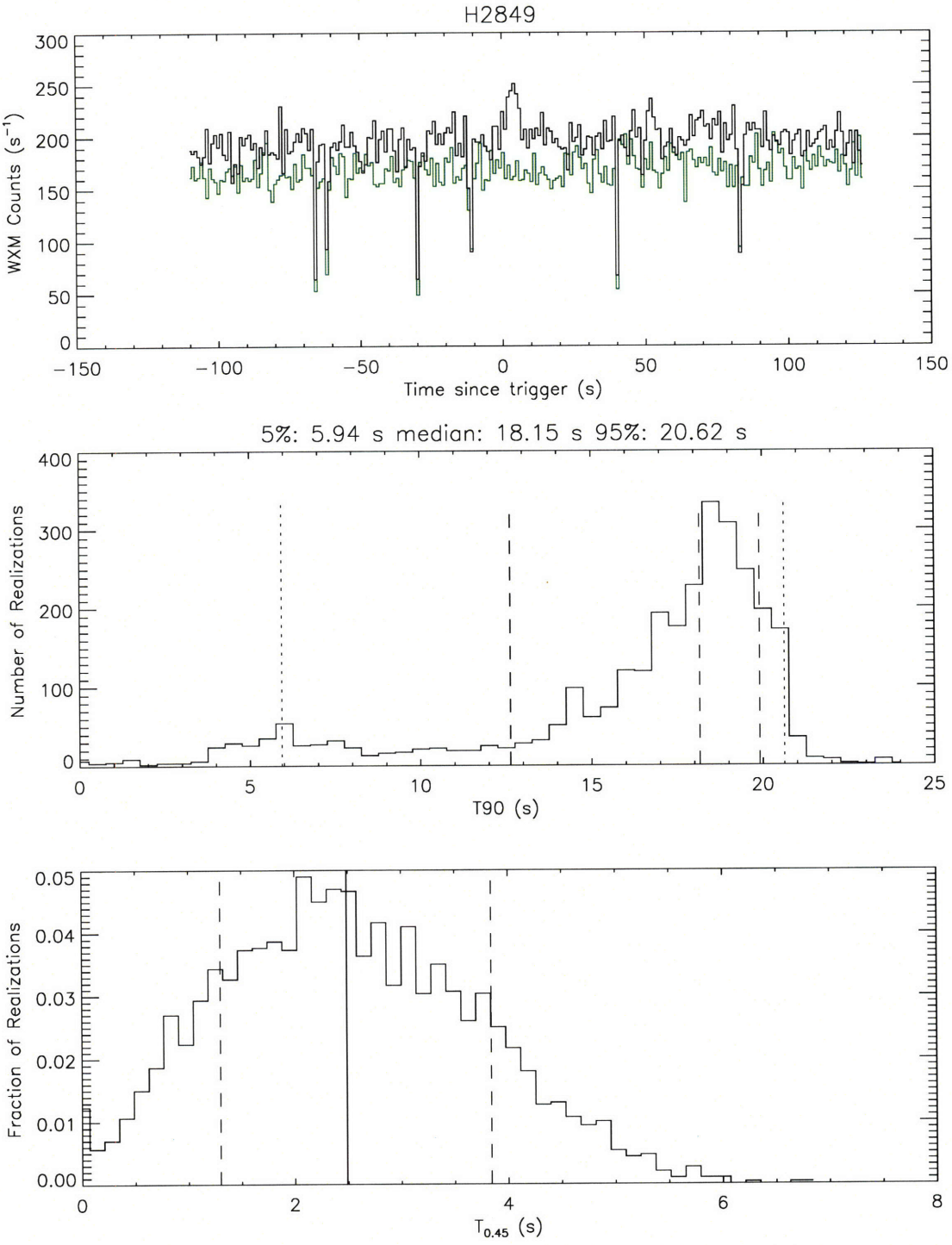

Figure A-14: BID H2849. The top panel shows the burst lightcurve and the background rate (in green). The middle panel shows the T_{90} distribution, with dashed lines indicating the median and one standard deviation, and dotted lines bounding the 90% confidence region. The bottom panel shows the $T_{0.45}$ distribution with a solid line indicating the median and dashed lines showing one standard deviations.

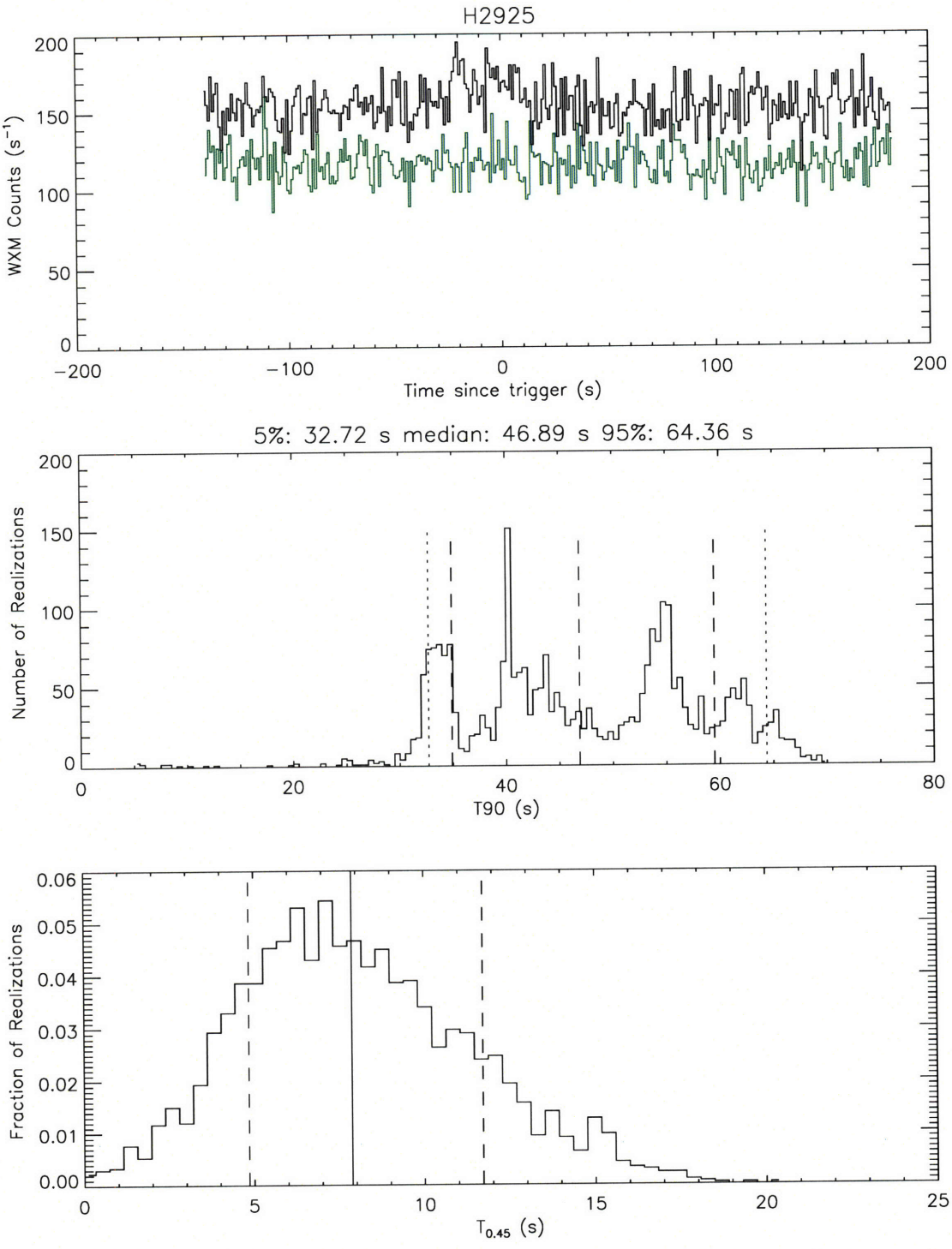

Figure A-15: BID H2925. The top panel shows the burst lightcurve and the background rate (in green). The middle panel shows the T_{90} distribution, with dashed lines indicating the median and one standard deviation, and dotted lines bounding the 90% confidence region. The bottom panel shows the $T_{0.45}$ distribution with a solid line indicating the median and dashed lines showing one standard deviations.

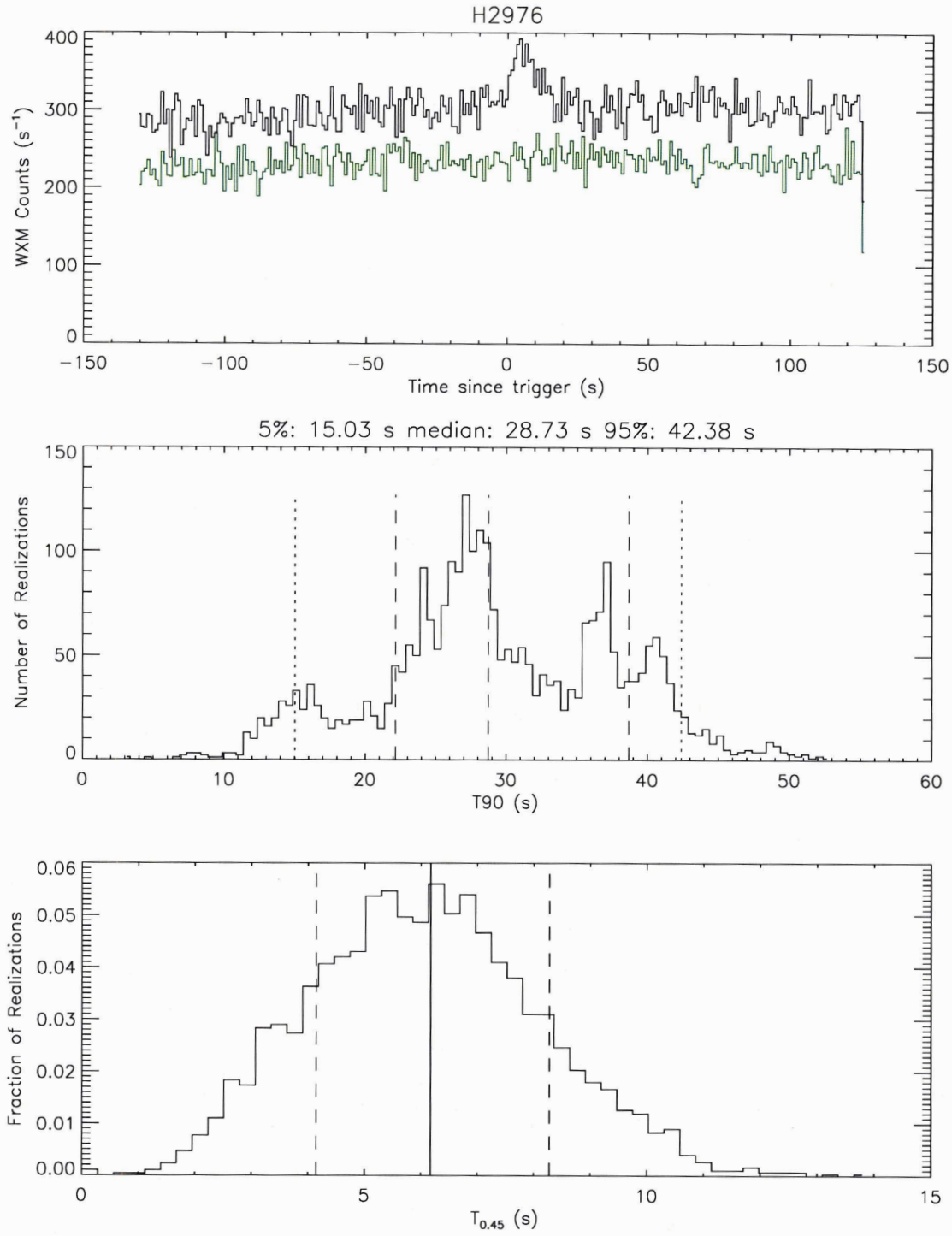

Figure A-16: BID H2976. The top panel shows the burst lightcurve and the background rate (in green). The middle panel shows the T_{90} distribution, with dashed lines indicating the median and one standard deviation, and dotted lines bounding the 90% confidence region. The bottom panel shows the $T_{0.45}$ distribution with a solid line indicating the median and dashed lines showing one standard deviations.

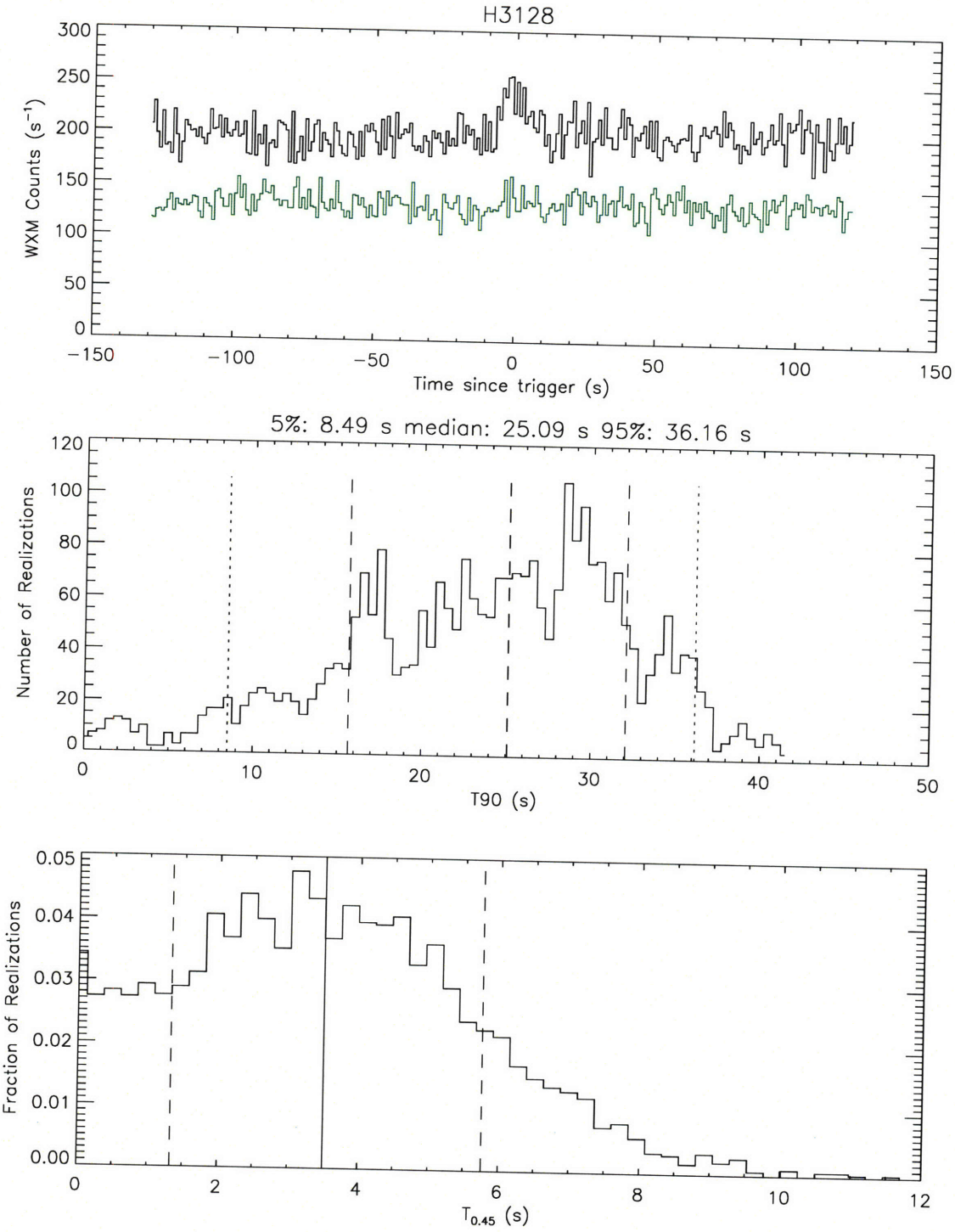

Figure A-17: BID H3128. The top panel shows the burst lightcurve and the background rate (in green). The middle panel shows the T_{90} distribution, with dashed lines indicating the median and one standard deviation, and dotted lines bounding the 90% confidence region. The bottom panel shows the $T_{0.45}$ distribution with a solid line indicating the median and dashed lines showing one standard deviations.

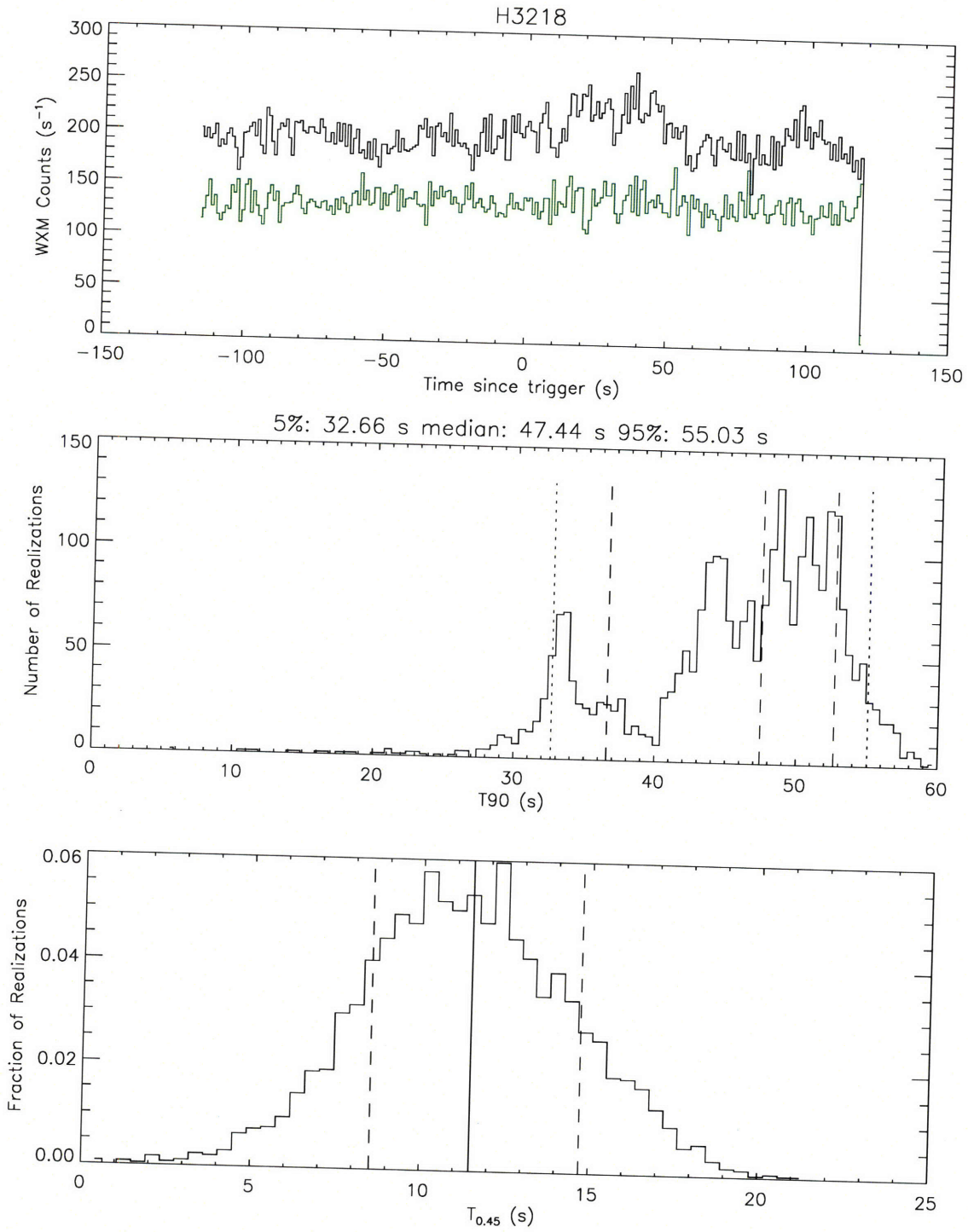

Figure A-18: BID H3218. The top panel shows the burst lightcurve and the background rate (in green). The middle panel shows the T_{90} distribution, with dashed lines indicating the median and one standard deviation, and dotted lines bounding the 90% confidence region. The bottom panel shows the $T_{0.45}$ distribution with a solid line indicating the median and dashed lines showing one standard deviations.

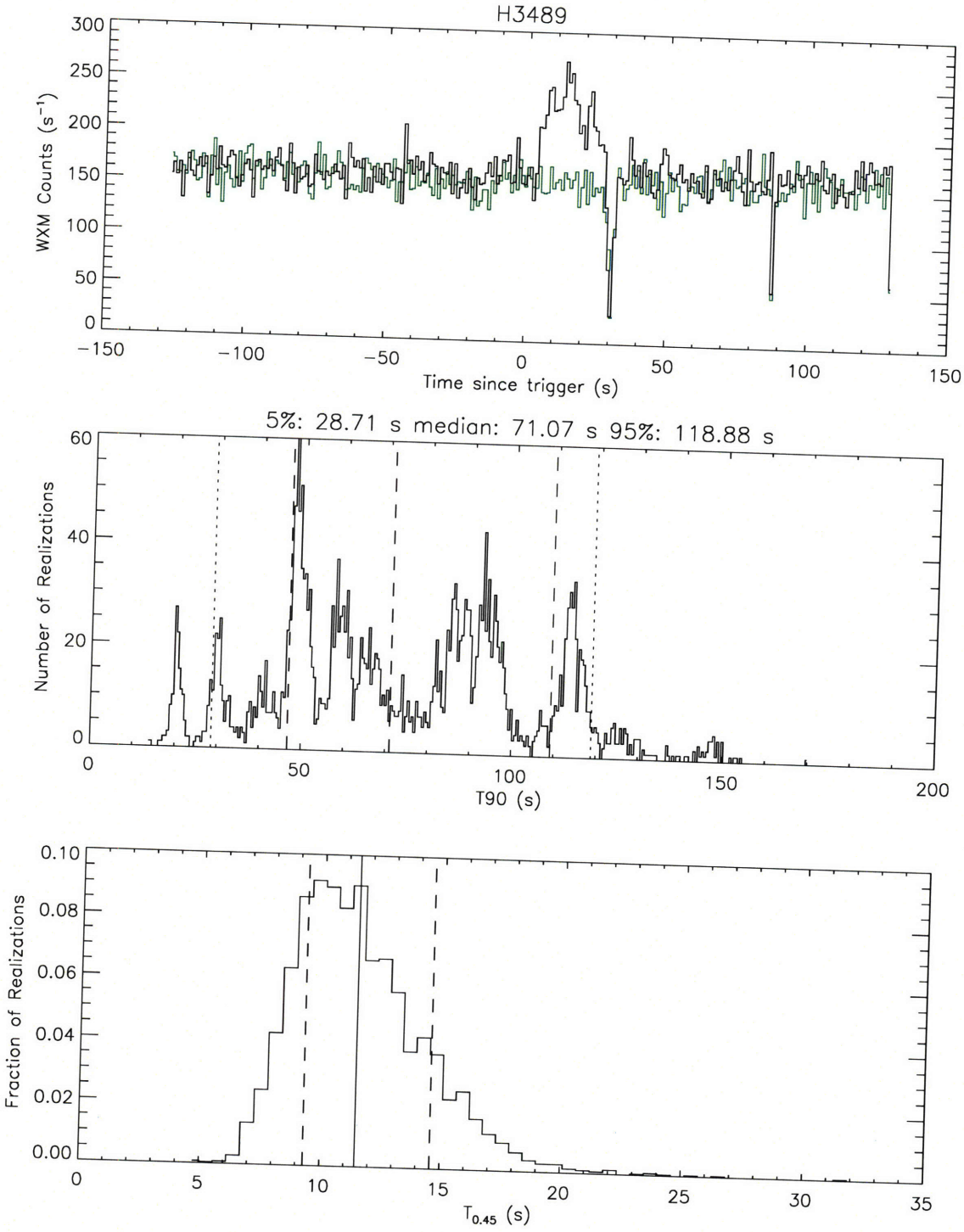

Figure A-19: BID H3489. The top panel shows the burst lightcurve and the background rate (in green). The middle panel shows the T_{90} distribution, with dashed lines indicating the median and one standard deviation, and dotted lines bounding the 90% confidence region. The bottom panel shows the $T_{0.45}$ distribution with a solid line indicating the median and dashed lines showing one standard deviations.

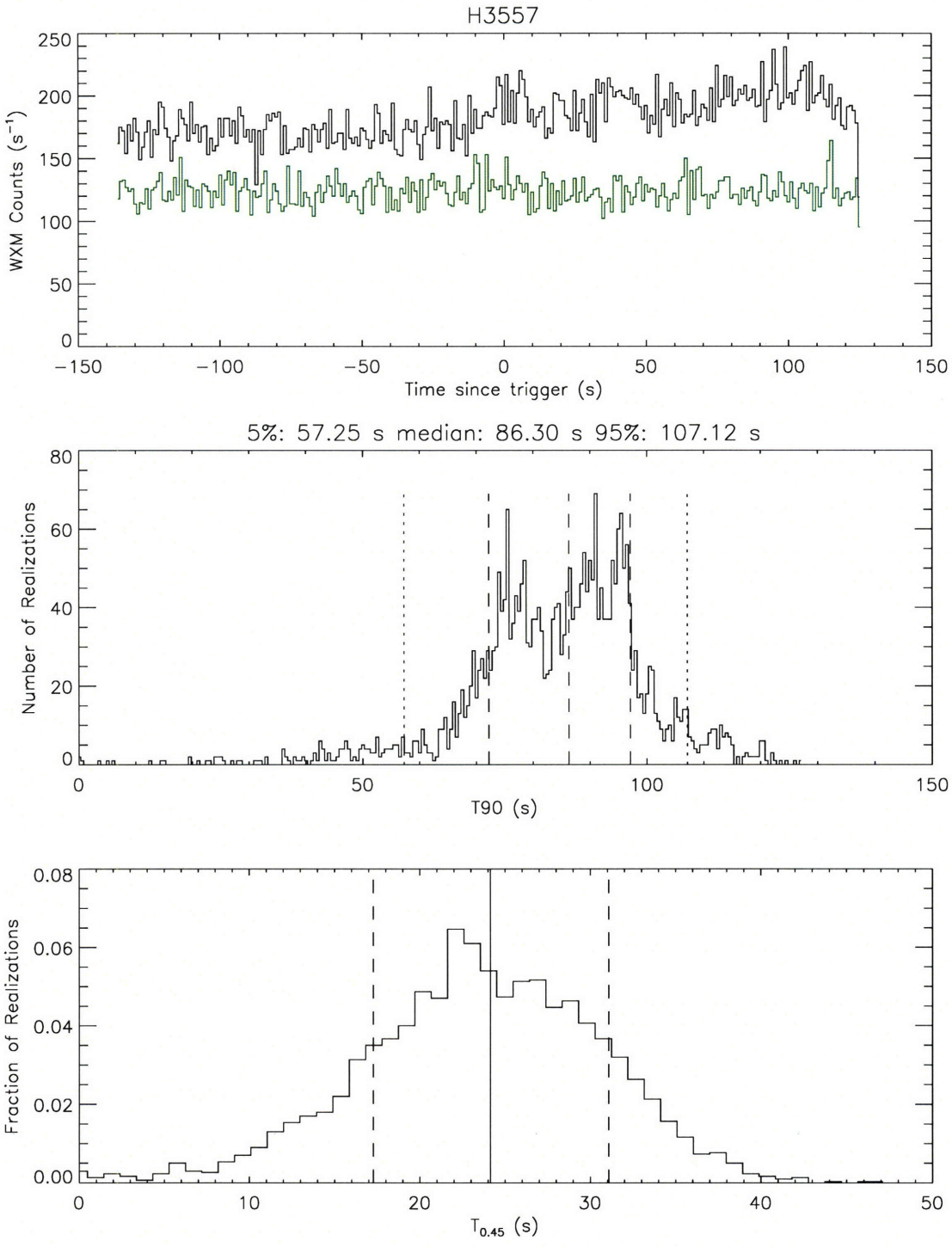

Figure A-20: BID H3557. The top panel shows the burst lightcurve and the background rate (in green). The middle panel shows the T_{90} distribution, with dashed lines indicating the median and one standard deviation, and dotted lines bounding the 90% confidence region. The bottom panel shows the $T_{0.45}$ distribution with a solid line indicating the median and dashed lines showing one standard deviations.

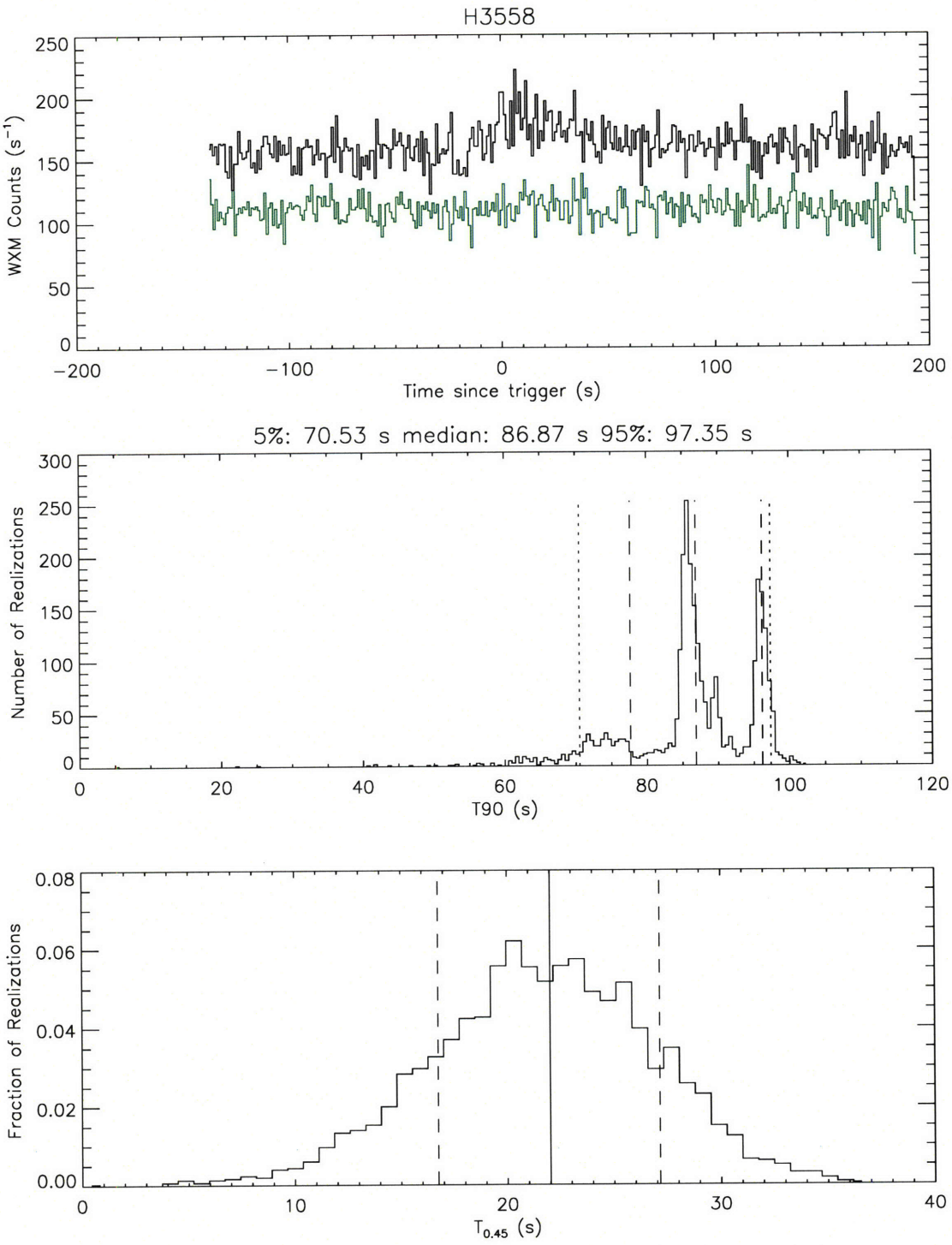

Figure A-21: BID H3558. The top panel shows the burst lightcurve and the background rate (in green). The middle panel shows the T_{90} distribution, with dashed lines indicating the median and one standard deviation, and dotted lines bounding the 90% confidence region. The bottom panel shows the $T_{0.45}$ distribution with a solid line indicating the median and dashed lines showing one standard deviations.

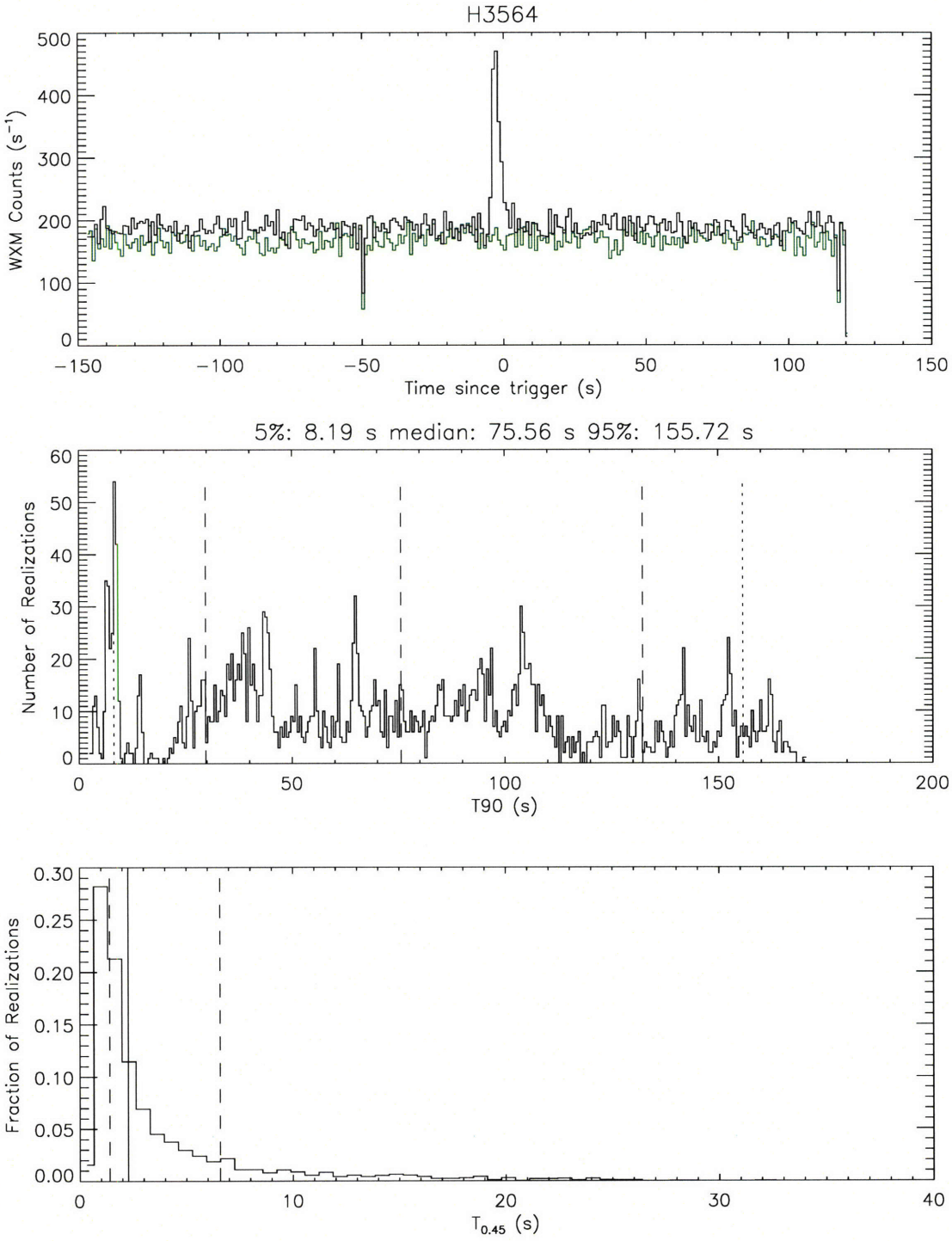

Figure A-22: BID H3564. The top panel shows the burst lightcurve and the background rate (in green). The middle panel shows the T_{90} distribution, with dashed lines indicating the median and one standard deviation, and dotted lines bounding the 90% confidence region. The bottom panel shows the $T_{0.45}$ distribution with a solid line indicating the median and dashed lines showing one standard deviations.

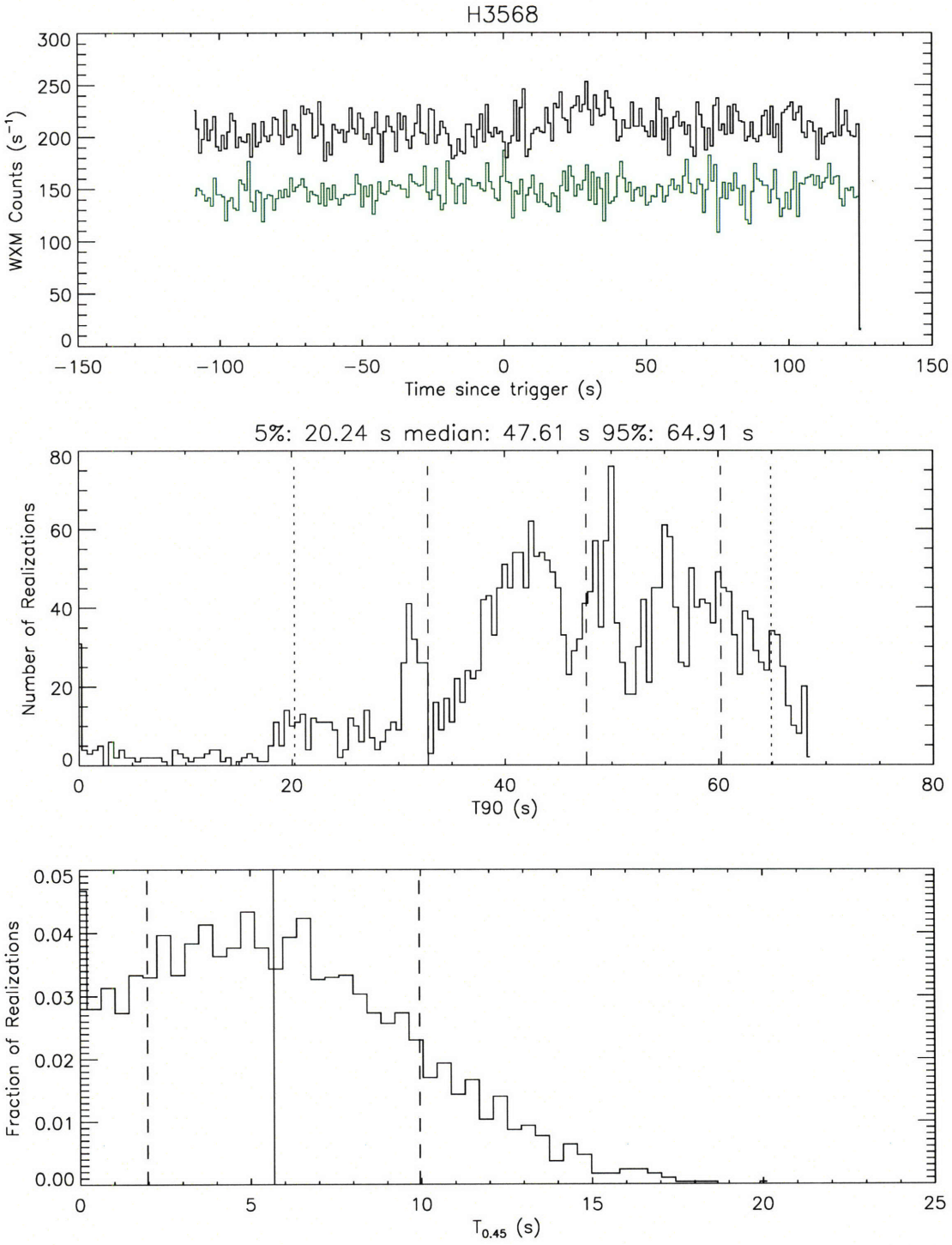

Figure A-23: BID H3568. The top panel shows the burst lightcurve and the background rate (in green). The middle panel shows the T_{90} distribution, with dashed lines indicating the median and one standard deviation, and dotted lines bounding the 90% confidence region. The bottom panel shows the $T_{0.45}$ distribution with a solid line indicating the median and dashed lines showing one standard deviations.

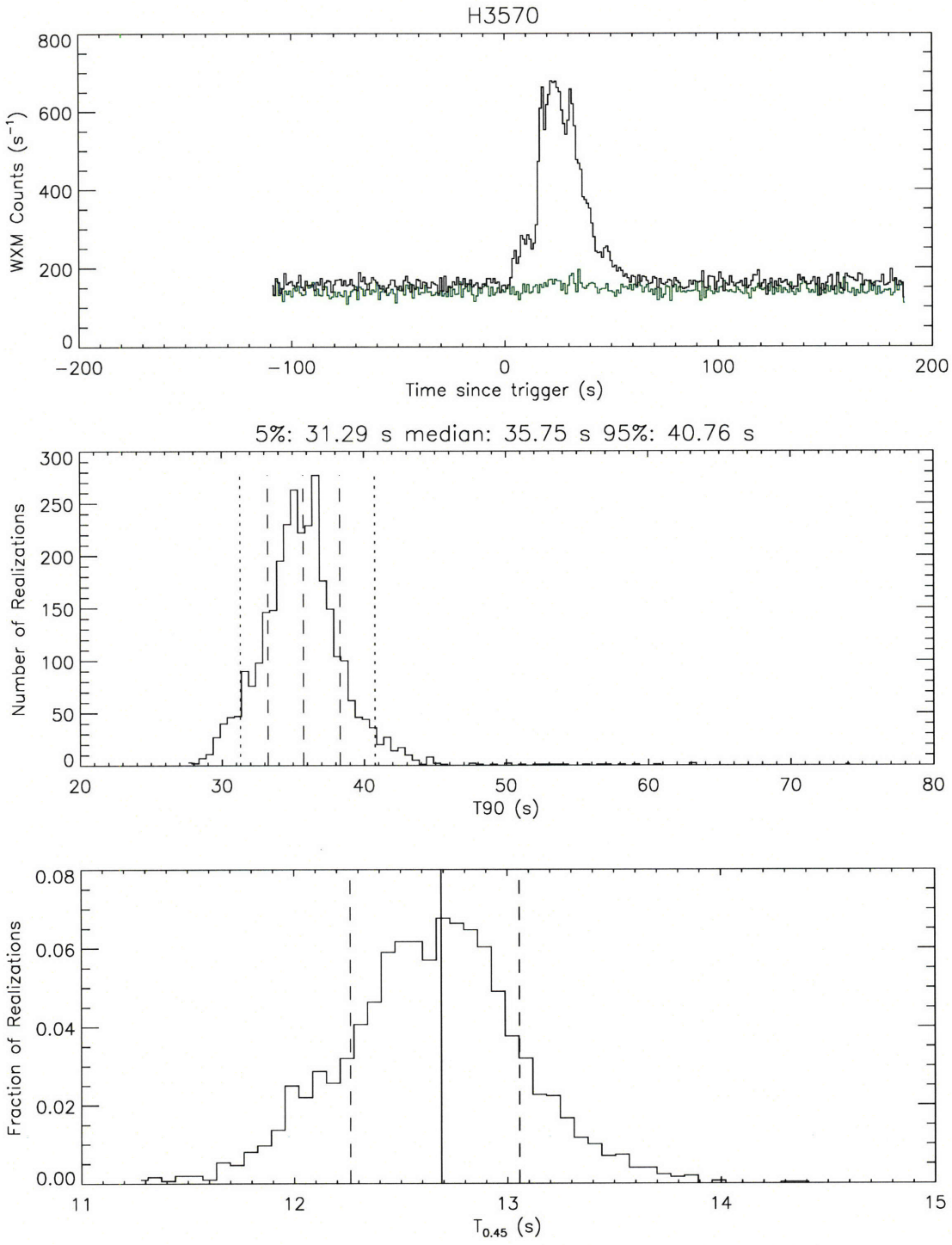

Figure A-24: BID H3570. The top panel shows the burst lightcurve and the background rate (in green). The middle panel shows the T_{90} distribution, with dashed lines indicating the median and one standard deviation, and dotted lines bounding the 90% confidence region. The bottom panel shows the $T_{0.45}$ distribution with a solid line indicating the median and dashed lines showing one standard deviations.

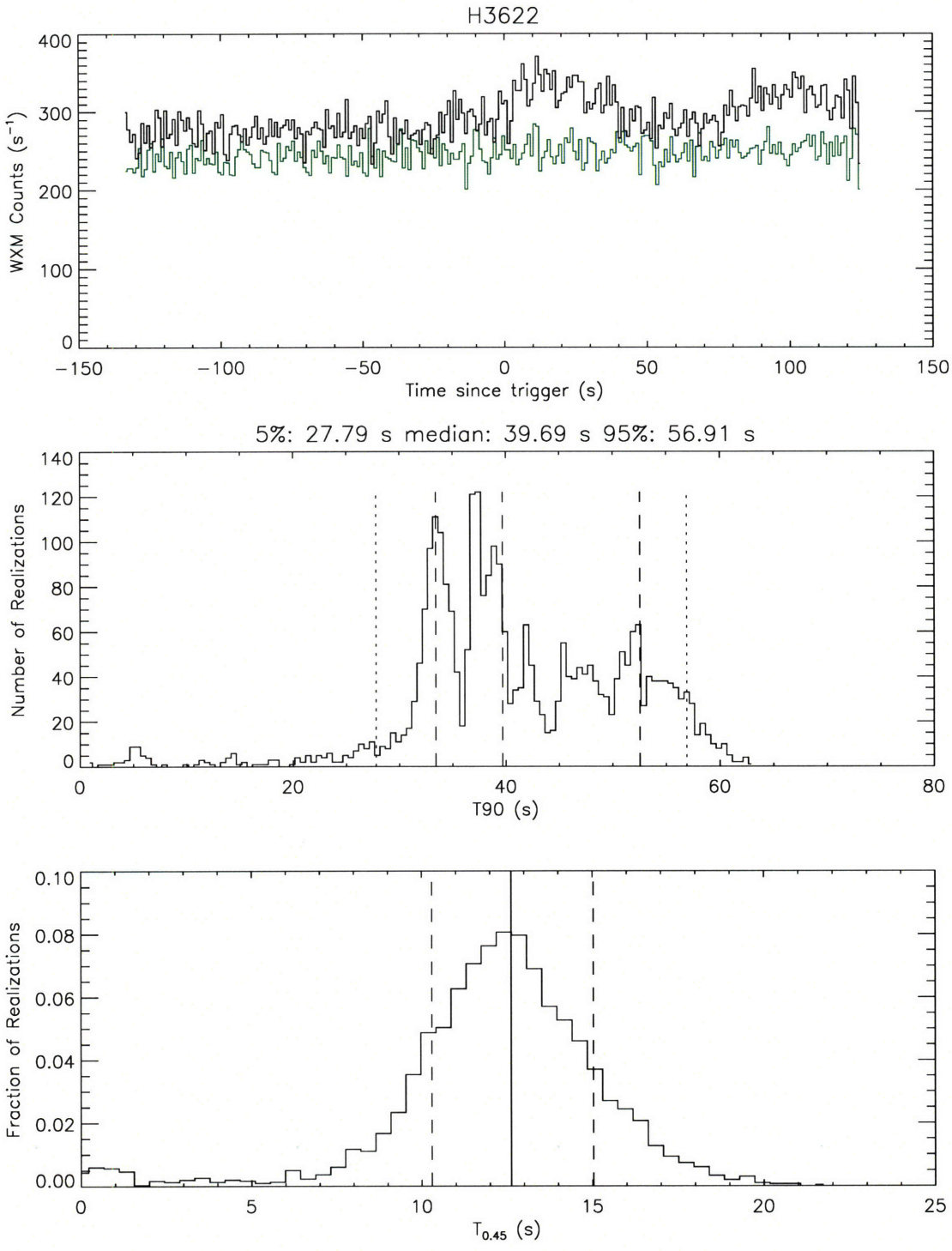

Figure A-25: BID H3622. The top panel shows the burst lightcurve and the background rate (in green). The middle panel shows the T_{90} distribution, with dashed lines indicating the median and one standard deviation, and dotted lines bounding the 90% confidence region. The bottom panel shows the $T_{0.45}$ distribution with a solid line indicating the median and dashed lines showing one standard deviations.

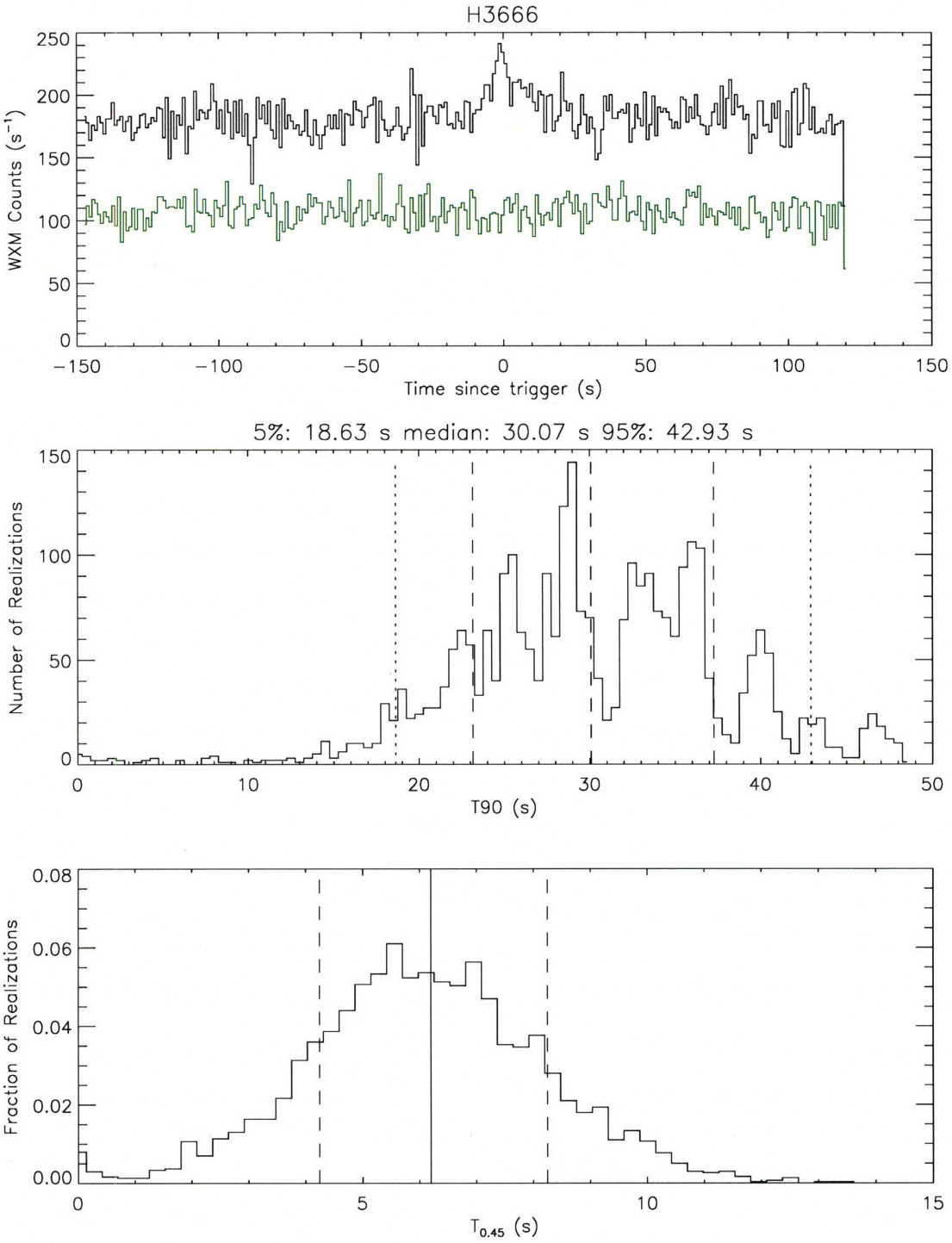

Figure A-26: BID H3666. The top panel shows the burst lightcurve and the background rate (in green). The middle panel shows the T_{90} distribution, with dashed lines indicating the median and one standard deviation, and dotted lines bounding the 90% confidence region. The bottom panel shows the $T_{0.45}$ distribution with a solid line indicating the median and dashed lines showing one standard deviations.

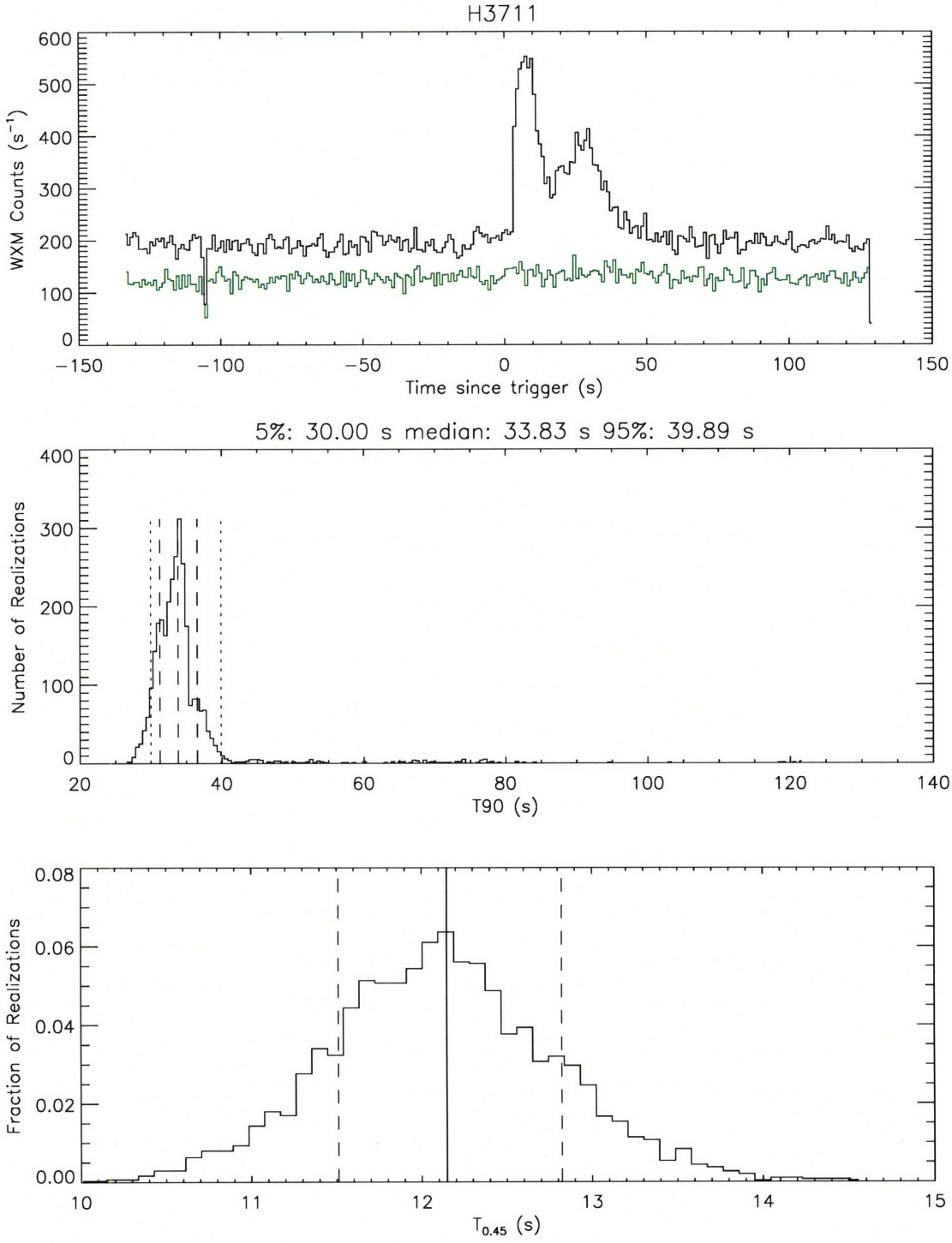

Figure A-27: BID H3711. The top panel shows the burst lightcurve and the background rate (in green). The middle panel shows the T_{90} distribution, with dashed lines indicating the median and one standard deviation, and dotted lines bounding the 90% confidence region. The bottom panel shows the $T_{0.45}$ distribution with a solid line indicating the median and dashed lines showing one standard deviations.

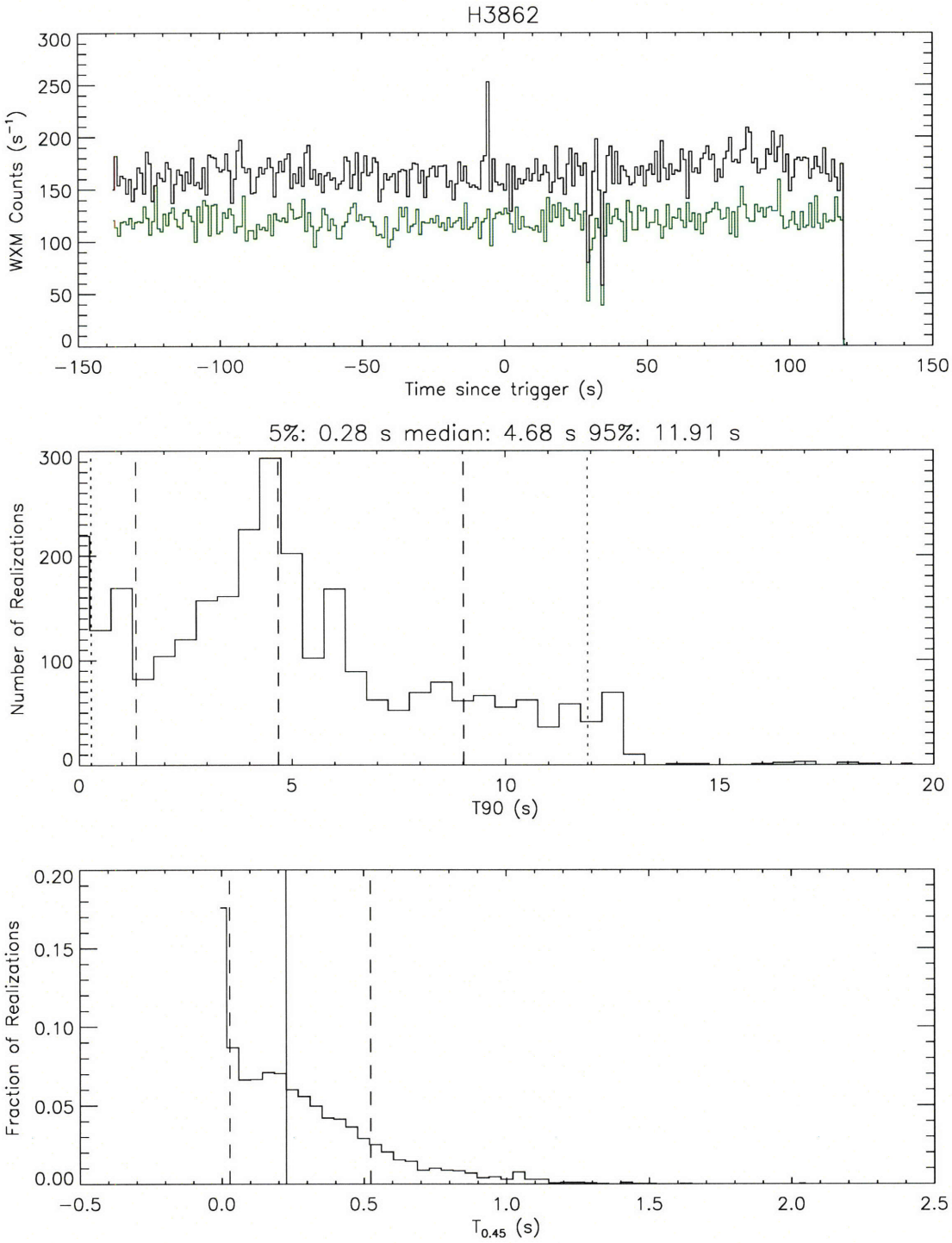

Figure A-28: BID H3862. The top panel shows the burst lightcurve and the background rate (in green). The middle panel shows the T_{90} distribution, with dashed lines indicating the median and one standard deviation, and dotted lines bounding the 90% confidence region. The bottom panel shows the $T_{0.45}$ distribution with a solid line indicating the median and dashed lines showing one standard deviations.

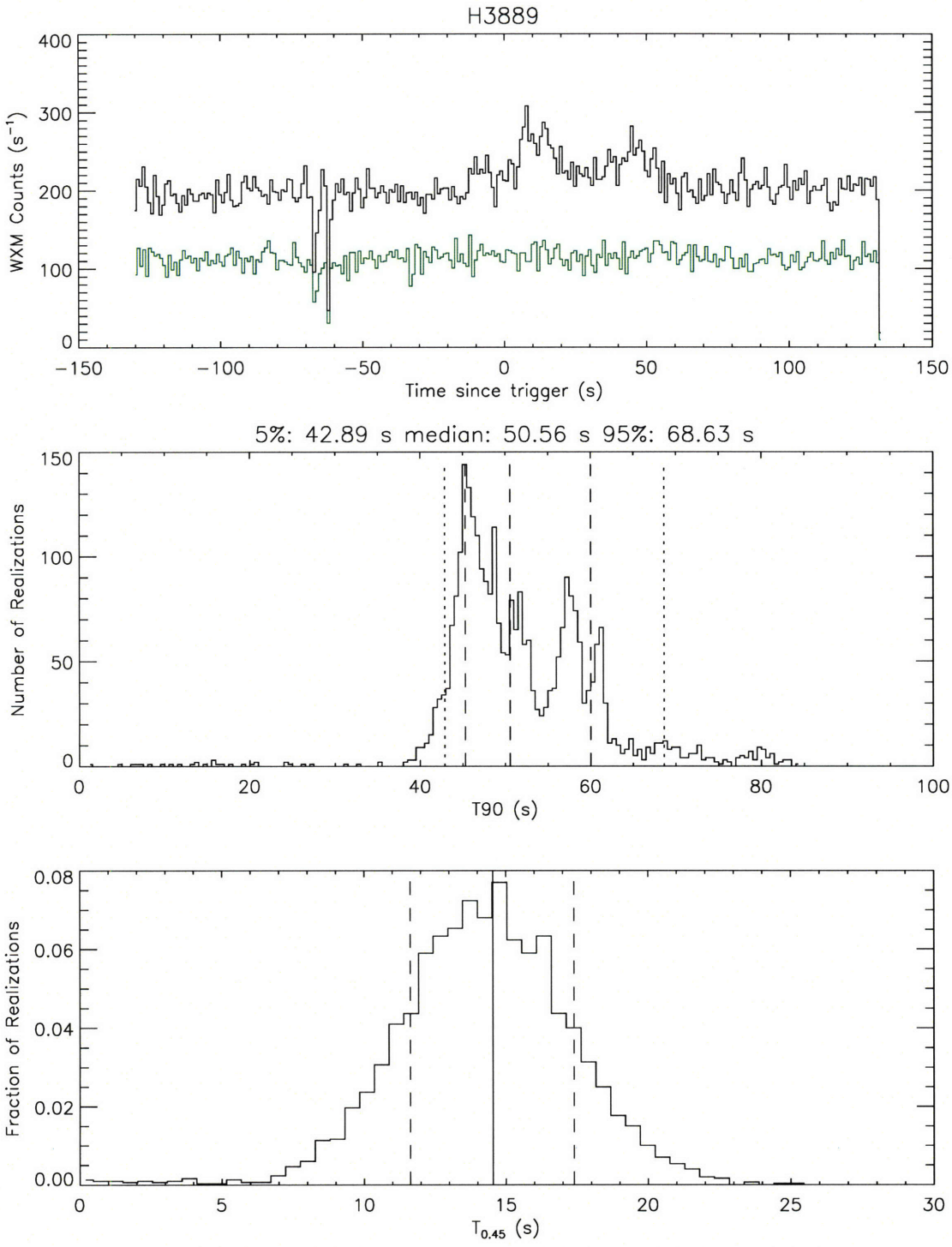

Figure A-29: BID H3889. The top panel shows the burst lightcurve and the background rate (in green). The middle panel shows the T_{90} distribution, with dashed lines indicating the median and one standard deviation, and dotted lines bounding the 90% confidence region. The bottom panel shows the $T_{0.45}$ distribution with a solid line indicating the median and dashed lines showing one standard deviations.

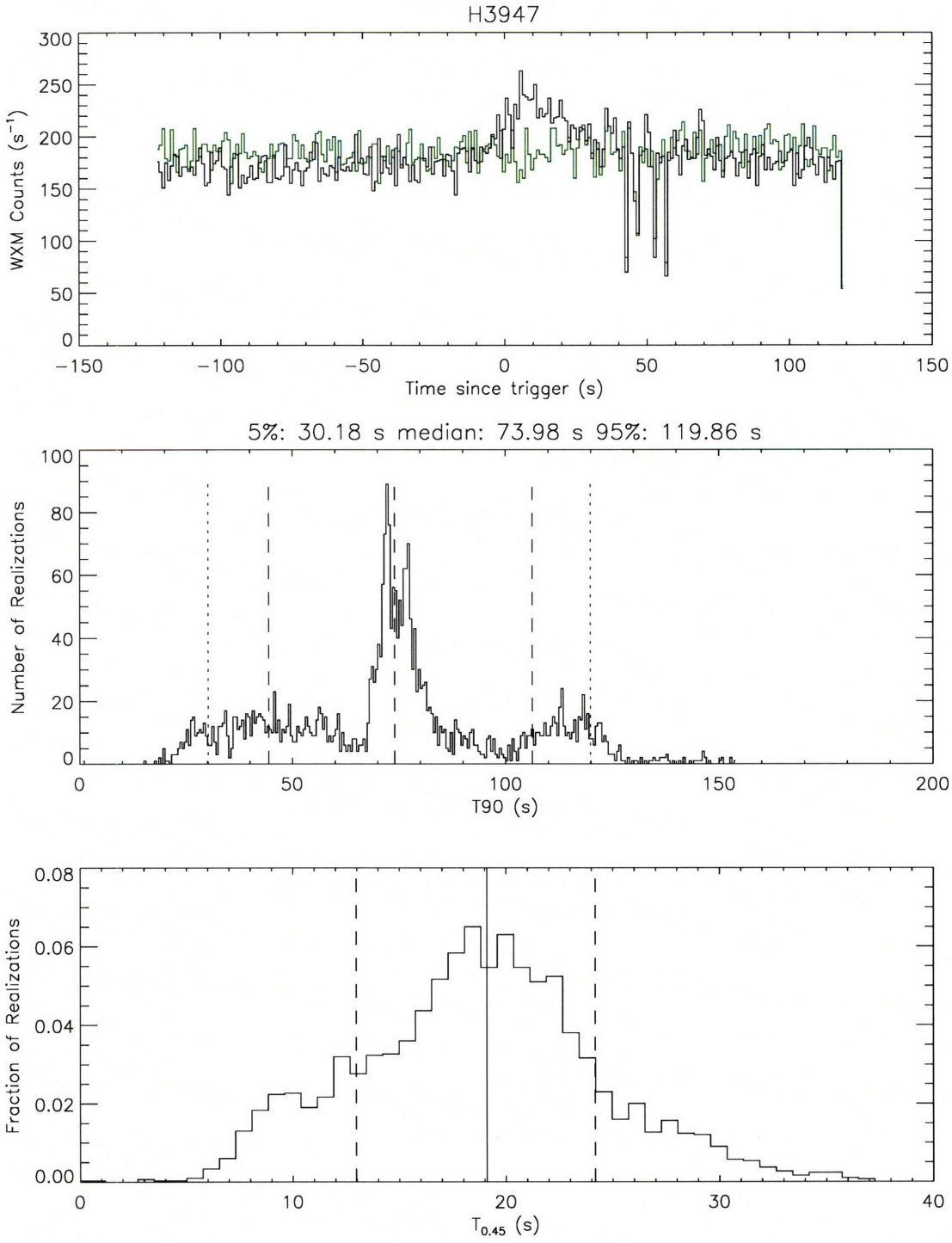

Figure A-30: BID H3947. The top panel shows the burst lightcurve and the background rate (in green). The middle panel shows the T_{90} distribution, with dashed lines indicating the median and one standard deviation, and dotted lines bounding the 90% confidence region. The bottom panel shows the $T_{0.45}$ distribution with a solid line indicating the median and dashed lines showing one standard deviations.

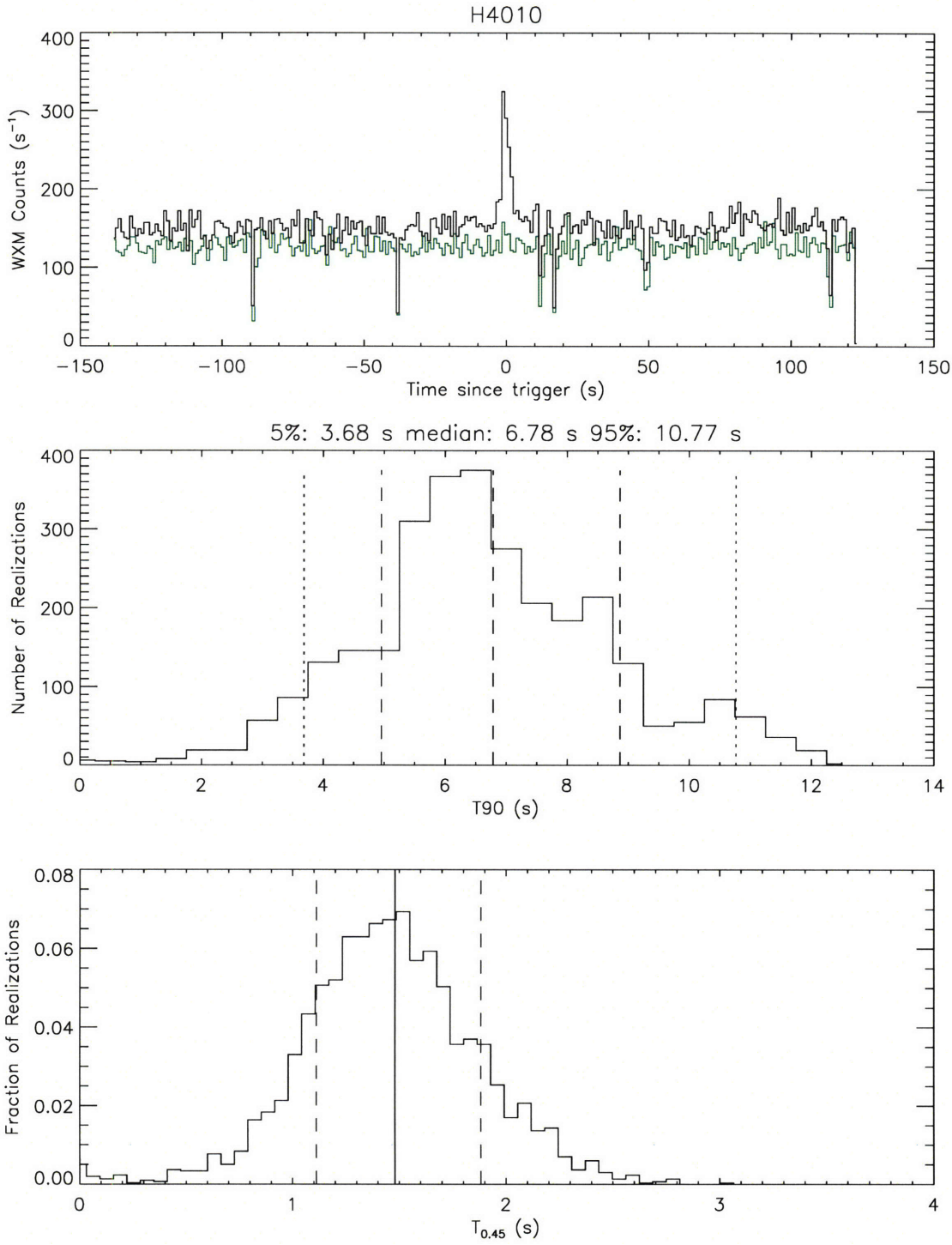

Figure A-31: BID H4010. The top panel shows the burst lightcurve and the background rate (in green). The middle panel shows the T_{90} distribution, with dashed lines indicating the median and one standard deviation, and dotted lines bounding the 90% confidence region. The bottom panel shows the $T_{0.45}$ distribution with a solid line indicating the median and dashed lines showing one standard deviations.

Bibliography

Amati, L. 2006, ArXiv Astrophysics e-prints, astro-ph/0601553

Amati, L., Frontera, F., Tavani, M., in't Zand, J. J. M., Antonelli, A., Costa, E., Feroci, M., Guidorzi, C., Heise, J., Masetti, N., Montanari, E., Nicastro, L., Palazzi, E., Pian, E., Piro, L., & Soffitta, P. 2002, A&A, 390, 81

Ascasibar, Y., Yepes, G., Gottlöber, S., & Müller, V. 2002, A&A, 387, 396

Atteia, J.-L., Boer, M., Cotin, F., Couteret, J., Dezalay, J.-P., Ehanno, M., Evrard, J., Lagrange, D., Niel, M., Olive, J.-F., Rouaix, G., Souleille, P., Vedrenne, G., Hurley, K., Ricker, G., Vanderspek, R., Crew, G., Doty, J., & Butler, N. 2003, in AIP Conf. Proc. 662: Gamma-Ray Burst and Afterglow Astronomy 2001: A Workshop Celebrating the First Year of the HETE Mission, ed. G. R. Ricker & R. K. Vanderspek, 17–24

Band, D., Matteson, J., Ford, L., Schaefer, B., Palmer, D., Teegarden, B., Cline, T., Briggs, M., Paciesas, W., Pendleton, G., Fishman, G., Kouveliotou, C., Meegan, C., Wilson, R., & Lestrade, P. 1993, ApJ, 413, 281

Band, D. L., Norris, J. P., & Bonnell, J. T. 2004, ApJ, 613, 484

Bloom, J. S., Frail, D. A., & Kulkarni, S. R. 2003, ApJ, 594, 674

Bloom, J. S., Frail, D. A., & Sari, R. 2001, AJ, 121, 2879

Briggs, M. S., Paciesas, W. S., Pendleton, G. N., Meegan, C. A., Fishman, G. J., Horack, J. M., Brock, M. N., Kouveliotou, C., Hartmann, D. H., & Hakkila, J. 1996, ApJ, 459, 40

Bromm, V., & Loeb, A. 2002, ApJ, 575, 111

—. 2006, ApJ, 642, 382

Butler, N. R. 2006, Private Communication

Choloniewski, J. 1987, MNRAS, 226, 273

Costa, E., Frontera, F., Heise, J., Feroci, M., in 't Zand, J., Fiore, F., Cinti, M. N., dal Fiume, D., Nicastro, L., Orlandini, M., Palazzi, E., Rapisarda, M., Zavattini, G., Jager, R., Parmar, A., Owens, A., Molendi, S., Cusumano, G., Maccarone,

M. C., Giarrusso, S., Coletta, A., Antonelli, L. A., Giommi, P., Muller, J. M., Piro, L., & Butler, R. C. 1997, Nature, 387, 783

Daigne, F., Rossi, E. M., & Mochkovitch, R. 2006, ArXiv Astrophysics e-prints, astro-ph/0607618

Donaghy, T., Lamb, D. Q., Reichart, D. E., & Graziani, C. 2003, in AIP Conf. Proc. 662: Gamma-Ray Burst and Afterglow Astronomy 2001: A Workshop Celebrating the First Year of the HETE Mission, ed. G. R. Ricker & R. K. Vanderspek, 450–453

Efron, B. 1979, The Annals of Statistics, 7, 1

Efron, B. 1982, The Jackknife, the Bootstrap and other resampling plans (CBMS-NSF Regional Conference Series in Applied Mathematics, Philadelphia: Society for Industrial and Applied Mathematics (SIAM), 1982)

Efron, B., & Petrosian, V. 1992, ApJ, 399, 345

Efron, B. and Tibshirani, R. 1993, An Introduction to the Bootstrap (Boca Raton: Chapman & Hall/CRC)

Eichler, D., Livio, M., Piran, T., & Schramm, D. N. 1989, Nature, 340, 126

Fenimore, E. E. 2004, Private Communication

Fenimore, E. E., in 't Zand, J. J. M., Norris, J. P., Bonnell, J. T., & Nemiroff, R. J. 1995, ApJ, 448, L101+

Fenimore, E. E., & Ramirez-Ruiz, E. 2000, ArXiv Astrophysics e-prints, astro-ph/0004176

Firmani, C., Avila-Reese, V., Ghisellini, G., & Ghirlanda, G. 2006a, ArXiv Astrophysics e-prints, astro-ph/0605267

—. 2006b, MNRAS, in press, doi:10.1111/j.1745-3933.2006.00219.x

Firmani, C., Avila-Reese, V., Ghisellini, G., & Tutukov, A. V. 2004, ApJ, 611, 1033

Firmani, C., Ghisellini, G., Avila-Reese, V., & Ghirlanda, G. 2006c, MNRAS, 370, 185

Fishman, G. J., Meegan, C. A., Wilson, R. B., Paciesas, W. S., Parnell, T. A., Austin, R. W., Rehage, J. R., Matteson, J. L., Teegarden, B. J., Cline, T. L., Schaefer, B. E., Pendleton, G. N., Berry, F. A., Horack, J. M., Storey, S. D., Brock, M. N., & Lestrade, J. P. 1989, in Proceedings of the Gamma Ray Observatory Science Workshop, ed. W. N. Johnson (Greenbelt, MD: NASA), 2–39–2–50

Frail, D. A., Kulkarni, S. R., Sari, R., Djorgovski, S. G., Bloom, J. S., Galama, T. J., Reichart, D. E., Berger, E., Harrison, F. A., Price, P. A., Yost, S. A., Diercks, A., Goodrich, R. W., & Chaffee, F. 2001, ApJ, 562, L55

Fruchter, A. S., Pian, E., Thorsett, S. E., Bergeron, L. E., González, R. A., Metzger, M., Goudfrooij, P., Sahu, K. C., Ferguson, H., Livio, M., Mutchler, M., Petro, L., Frontera, F., Galama, T., Groot, P., Hook, R., Kouveliotou, C., Macchetto, D., van Paradijs, J., Palazzi, E., Pedersen, H., Sparks, W., & Tavani, M. 1999, ApJ, 516, 683

Ghirlanda, G., Ghisellini, G., & Lazzati, D. 2004a, ApJ, 616, 331

Ghirlanda, G., Ghisellini, G., Lazzati, D., & Firmani, C. 2004b, ApJ, 613, L13

Graziani, C., & Lamb, D. Q. 2003, in AIP Conf. Proc. 662: Gamma-Ray Burst and Afterglow Astronomy 2001: A Workshop Celebrating the First Year of the HETE Mission, ed. G. R. Ricker & R. K. Vanderspek, 76–78

Grindlay, J. E., & The Exist Team. 2006, in American Institute of Physics Conference Series, ed. S. S. Holt, N. Gehrels, & J. A. Nousek, 631–641

Heise, J., in't Zand, J., Kippen, R. M., & Woods, P. M. 2001, in Gamma-ray Bursts in the Afterglow Era, ed. E. Costa, F. Frontera, & J. Hjorth, 16–+

Horváth, I. 1998, ApJ, 508, 757

—. 2002, A&A, 392, 791

Horváth, I., Balázs, L. G., Bagoly, Z., Ryde, F., & Mészáros, A. 2006, A&A, 447, 23

Hurley, K. 1992, in American Institute of Physics Conference Series, ed. W. S. Paciesas & G. J. Fishman, 3–12

Ioka, K., & Nakamura, T. 2002, ApJ, 570, L21

Jernigan, J. G. 2006, Private Communication

Kawai, N., Kosugi, G., Aoki, K., Yamada, T., Totani, T., Ohta, K., Iye, M., Hattori, T., Aoki, W., Furusawa, H., Hurley, K., Kawabata, K. S., Kobayashi, N., Komiyama, Y., Mizumoto, Y., Nomoto, K., Noumaru, J., Ogasawara, R., Sato, R., Sekiguchi, K., Shirasaki, Y., Suzuki, M., Takata, T., Tamagawa, T., Terada, H., Watanabe, J., Yatsu, Y., & Yoshida, A. 2006, Nature, 440, 184

Kawai, N., Yoshida, A., Matsuoka, M., Shirasaki, Y., Tamagawa, T., Torii, K., Sakamoto, T., Takahashi, D., Fenimore, E., Galassi, M., Tavenner, T., Lamb, D. Q., Graziani, C., Donaghy, T., Vanderspek, R., Yamauchi, M., Takagishi, K., & Hatsukade, I. 2003, in AIP Conf. Proc. 662: Gamma-Ray Burst and Afterglow Astronomy 2001: A Workshop Celebrating the First Year of the HETE Mission, ed. G. R. Ricker & R. K. Vanderspek, 25–32

Klebesadel, R. W., Strong, I. B., & Olson, R. A. 1973, ApJ, 182, L85+

Kocevski, D., & Liang, E. 2006, ApJ, 642, 371

Kommers, J. M., Lewin, W. H. G., Kouveliotou, C., van Paradijs, J., Pendleton, G. N., Meegan, C. A., & Fishman, G. J. 2000, ApJ, 533, 696

Koshut, T. M., Paciesas, W. S., Kouveliotou, C., van Paradijs, J., Pendleton, G. N., Fishman, G. J., & Meegan, C. A. 1996, ApJ, 463, 570

Kouveliotou, C., Meegan, C. A., Fishman, G. J., Bhat, N. P., Briggs, M. S., Koshut, T. M., Paciesas, W. S., & Pendleton, G. N. 1993, ApJ, 413, L101

Lamb, D. Q. 1995, PASP, 107, 1152

Lamb, D. Q., & Reichart, D. E. 2000, ApJ, 536, 1

Lamb, D. Q., Ricker, G. R., Lazzati, D., Ghirlanda, G., Ghisellini, G., Firmani, C., Amati, L., Atteia, J. ., Avila-Reese, V., Burles, S., Butler, N., Chen, H. ., Costa, E., Doty, J., Frontera, F., Fruchter, A., Garnavich, P., Graziani, C., Jernigan, J. G., Kawai, N., Mazzali, P., Meszaros, P., Piro, L., Sakamoto, T., Stanek, K., Vietri, M., della Valle, M., Villasenor, J., & Zhang, B. 2005, ArXiv Astrophysics e-prints

Le Floc'h, E. 2004, New Astronomy Review, 48, 601

Le Floc'h, E., Duc, P.-A., Mirabel, I. F., Sanders, D. B., Bosch, G., Diaz, R. J., Donzelli, C. J., Rodrigues, I., Courvoisier, T. J.-L., Greiner, J., Mereghetti, S., Melnick, J., Maza, J., & Minniti, D. 2003, A&A, 400, 499

Li, L.-X. 2006, ArXiv Astrophysics e-prints, astro-ph/0607366

Lichti, G. G., Briggs, M. S., Diehl, R., Fishman, G., Georgii, R., Kippen, R. M., Kouveliotou, C., Meegan, C., Paciesas, W., Preece, R., Schönfelder, V., & von Kienlin, A. 2001, in Gamma-ray Bursts in the Afterglow Era, ed. E. Costa, F. Frontera, & J. Hjorth, 371–+

Lloyd-Ronning, N. M., Dai, X., & Zhang, B. 2004, ApJ, 601, 371

Lloyd-Ronning, N. M., Fryer, C. L., & Ramirez-Ruiz, E. 2002, ApJ, 574, 554

Lynden-Bell, D. 1971, MNRAS, 155, 95

MacFadyen, A. I., & Woosley, S. E. 1999, ApJ, 524, 262

Maloney, A., & Petrosian, V. 1999, ApJ, 518, 32

Mannucci, F., Buttery, H., Maiolino, R., Marconi, A., & Pozzetti, L. 2006, ArXiv Astrophysics e-prints, astro-ph/0607143

Marshall, H. L., Tananbaum, H., Avni, Y., & Zamorani, G. 1983, ApJ, 269, 35

Mazets, E. P., & Golenetskii, S. V. 1981, Ap&SS, 75, 47

McBreen, B., Hurley, K. J., Long, R., & Metcalfe, L. 1994, MNRAS, 271, 662

McBreen, S., Quilligan, F., McBreen, B., Hanlon, L., & Watson, D. 2001, A&A, 380, L31

Mitrofanov, I. G., Anfimov, D. S., Litvak, M. L., Sanin, A. B., Saevich, Y. Y., Briggs, M. S., Paciesas, W. S., Pendleton, G. N., Preece, R. D., Koshut, T. M., Fishman, G. J., Meegan, C. A., & Lestrade, J. P. 1999, ApJ, 522, 1069

Mukherjee, S., Feigelson, E. D., Jogesh Babu, G., Murtagh, F., Fraley, C., & Raftery, A. 1998, ApJ, 508, 314

Norris, J. P., Marani, G. F., & Bonnell, J. T. 2000, ApJ, 534, 248

Norris, J. P., Nemiroff, R. J., Bonnell, J. T., Scargle, J. D., Kouveliotou, C., Paciesas, W. S., Meegan, C. A., & Fishman, G. J. 1996, ApJ, 459, 393

Paciesas, W. S., Meegan, C. A., Pendleton, G. N., Briggs, M. S., Kouveliotou, C., Koshut, T. M., Lestrade, J. P., McCollough, M. L., Brainerd, J. J., Hakkila, J., Henze, W., Preece, R. D., Connaughton, V., Kippen, R. M., Mallozzi, R. S., Fishman, G. J., Richardson, G. A., & Sahi, M. 1999, ApJS, 122, 465

Paczyński, B. 1991, Acta Astronomica, 41, 257

—. 1995, PASP, 107, 1167

—. 1998, ApJ, 494, L45+

Perlmutter, S., Aldering, G., Goldhaber, G., Knop, R. A., Nugent, P., Castro, P. G., Deustua, S., Fabbro, S., Goobar, A., Groom, D. E., Hook, I. M., Kim, A. G., Kim, M. Y., Lee, J. C., Nunes, N. J., Pain, R., Pennypacker, C. R., Quimby, R., Lidman, C., Ellis, R. S., Irwin, M., McMahon, R. G., Ruiz-Lapuente, P., Walton, N., Schaefer, B., Boyle, B. J., Filippenko, A. V., Matheson, T., Fruchter, A. S., Panagia, N., Newberg, H. J. M., Couch, W. J., & The Supernova Cosmology Project. 1999, ApJ, 517, 565

Preece, R. D., Briggs, M. S., Mallozzi, R. S., Pendleton, G. N., Paciesas, W. S., & Band, D. L. 2000, ApJS, 126, 19

Reichart, D. E., Lamb, D. Q., Fenimore, E. E., Ramirez-Ruiz, E., Cline, T. L., & Hurley, K. 2001, ApJ, 552, 57

Ricker, G. R., Atteia, J.-L., Crew, G. B., Doty, J. P., Fenimore, E. E., Galassi, M., Graziani, C., Hurley, K., Jernigan, J. G., Kawai, N., Lamb, D. Q., Matsuoka, M., Pizzichini, G., Shirasaki, Y., Tamagawa, T., Vanderspek, R., Vedrenne, G., Villasenor, J., Woosley, S. E., & Yoshida, A. 2003, in AIP Conf. Proc. 662: Gamma-Ray Burst and Afterglow Astronomy 2001: A Workshop Celebrating the First Year of the HETE Mission, ed. G. R. Ricker & R. K. Vanderspek, 3–16

Riess, A. G., Filippenko, A. V., Challis, P., Clocchiatti, A., Diercks, A., Garnavich, P. M., Gilliland, R. L., Hogan, C. J., Jha, S., Kirshner, R. P., Leibundgut, B., Phillips, M. M., Reiss, D., Schmidt, B. P., Schommer, R. A., Smith, R. C., Spyromilio, J., Stubbs, C., Suntzeff, N. B., & Tonry, J. 1998, AJ, 116, 1009

Sakamoto, T. 2004, PhD thesis, The Institute of Physical and Chemical Research

Sakamoto, T., Lamb, D. Q., Kawai, N., Yoshida, A., Graziani, C., Fenimore, E. E., Donaghy, T. Q., Matsuoka, M., Suzuki, M., Ricker, G., Atteia, J.-L., Shirasaki, Y., Tamagawa, T., Torii, K., Galassi, M., Doty, J., Vanderspek, R., Crew, G. B., Villasenor, J., Butler, N., Prigozhin, G., Jernigan, J. G., Barraud, C., Boer, M., Dezalay, J.-P., Olive, J.-F., Hurley, K., Levine, A., Monnelly, G., Martel, F., Morgan, E., Woosley, S. E., Cline, T., Braga, J., Manchanda, R., Pizzichini, G., Takagishi, K., & Yamauchi, M. 2005, ApJ, 629, 311

Sari, R., Piran, T., & Halpern, J. P. 1999, ApJ, 519, L17

Sari, R., Piran, T., & Narayan, R. 1998, ApJ, 497, L17+

Schaefer, B. E. 2003, ApJ, 583, L67

Sethi, S., & Bhargavi, S. G. 2001, A&A, 376, 10

Shirasaki, Y., Kawai, N., Yoshida, A., Matsuoka, M., Tamagawa, T., Torii, K., Sakamoto, T., Suzuki, M., Urata, Y., Sato, R., Nakagawa, Y., Takahashi, D., Fenimore, E. E., Galassi, M., Lamb, D. Q., Graziani, C., Donaghy, T. Q., Vanderspek, R., Yamauchi, M., Takagishi, K., & Hatsukade, I. 2003, PASJ, 55, 1033

Strohmayer, T. E., Fenimore, E. E., Murakami, T., & Yoshida, A. 1998, ApJ, 500, 873

Villasenor, J. N., Dill, R., Doty, J. P., Monnelly, G., Vanderspek, R., Kissel, S., Prigozhin, G., Crew, G. B., & Ricker, G. R. 2003, in AIP Conf. Proc. 662: Gamma-Ray Burst and Afterglow Astronomy 2001: A Workshop Celebrating the First Year of the HETE Mission, ed. G. R. Ricker & R. K. Vanderspek, 33–37

Woods, E., & Loeb, A. 1995, ApJ, 453, 583

Woosley, S. E. 1993, ApJ, 405, 273

Woosley, S. E., & Bloom, J. S. 2006, ARA&A, 44, 507

Yonetoku, D., Murakami, T., Nakamura, T., Yamazaki, R., Inoue, A. K., & Ioka, K. 2004, ApJ, 609, 935

Zhang, B., & Mészáros, P. 2002, ApJ, 571, 876